Degradation of TBC Systems in Environments Relevant to Advanced Gas Turbines for IGCC Systems

Final Project Report

April, 2015

Principal Investigator: Prof. Brian Gleeson
Dept. Mechanical Engineering and Materials Science
University of Pittsburgh
Pittsburgh, PA 15261

Submitted to: Dr. Seth Lawson
University Turbine Systems Research Program
National Energy Technology Laboratory
Department of Energy

DOE award number: DE-FE0007271

DUNS Number: 004514360

Project Period: Oct. 1, 2011 – Sept. 30, 2014

Disclaimer

Abstract

Air plasma sprayed (APS) thermal barrier coatings (TBCs) are used to provide thermal insulation for the hottest components in gas turbines. Zirconia stabilized with 7wt% yttria (7YSZ) is the most common ceramic top coat used for turbine blades. The 7YSZ coating can be degraded from the buildup of fly-ash deposits created in the power-generation process. Fly ash from an integrated gasification combined cycle (IGCC) system can result from coal-based syngas. TBCs are also exposed to harsh gas environments containing CO_2, SO_2, and steam. Degradation from the combined effects of fly ash and harsh gas atmospheres has the potential to severely limit TBC lifetimes. The main objective of this study was to use lab-scale testing to systematically elucidate the interplay between prototypical deposit chemistries (*i.e.*, ash and its constituents, K_2SO_4, and FeS) and environmental oxidants (i.e., O_2, H_2O and CO_2) on the degradation behavior of advanced TBC systems. Several mechanisms of early TBC failure were identified, as were the specific fly-ash constituents responsible for degradation. The reactivity of MCrAlY bondcoats used in TBC systems was also investigated. The specific roles of oxide and sulfate components were assessed, together with the complex interplay between gas composition, deposit chemistry and alloy reactivity. Bondcoat composition design strategies to mitigate corrosion were established, particularly with regard to controlling phase constitution and the amount of reactive elements the bondcoat contains in order to achieve optimal corrosion resistance.

Table of Contents

1 Background

1.1 IGCC Process and fly-ash deposits

The large-scale use of coal in generating electricity has led to the development of technologies that can improve efficiency and cleanliness of using coal-derived fuels [1]. Integrated gasification combined cycle (IGCC) plants are being developed to reduce emissions compared to conventional coal-fired power plants and still operate with comparable efficiencies [2, 3]. These plants convert coal or a combination of coal+biomass into a synthetic gas (syngas) fuel containing varying amounts of H_2 and CO, which is cleaned and burned in a combustion turbine to create electricity [4]. The advantages of this process include flexibility in fuel source, low emissions, and efficient CO_2 capture. During the IGCC process, turbine components are subjected to harsh gas atmospheres containing CO_2, SO_2, and steam at high temperatures. The degradation of turbine components in these atmospheres can be enhanced by the deposit of fly-ash which is comprised primarily of silica (SiO_2), alumina (Al_2O_3), and calcia (CaO) as well as iron oxide (Fe_2O_3) and magnesia (MgO) [5]. In addition to the oxide components, fly-ash typically contains impurities of K_2SO_4 and Na_2SO_4 from the coal or biomass fuel source, and FeS from the interaction of SO_2 with metallic components in the system [6]. The degradation of turbine components from the combined effects of harsh gas atmospheres and fly-ash deposits at temperatures in the range of 900-1100°C are not well understood.

The main components of an IGCC plant are shown in Figure 1. The majority of electricity is produced by the combustion turbine. Overall plant efficiency is improved by utilizing heat from the combustion turbine and from the gasifier to produce additional electricity in a heat recovery steam generator [7]. One primary advantage of this process is that the syngas is cleaned prior to combustion. This is done at relatively low temperatures, and can be done more efficiently than a conventional pulverized coal plant [8, 9]. Some fly-ash, however, can still exist in the gas turbine. The sources of this fly-ash can be small amounts from the coal that did not get filtered out before combustion. Fly-ash deposits can also be generated from interaction of turbine gases with upstream components in the system [10]. The largest source of fly-ash in IGCC systems, however, is typically from ambient air passing through the turbine [11]. The exact composition of fly-ash will vary as the relative ratios of oxides and the other components change based on geography as well as fuel source (type of coal, biomass, etc). Combustion of bituminous and anthracite coal, for example, tend to produce fly-ash with higher levels of SiO_2 and Al_2O_3. Fly-ash from subbituminous and lignite coals, in contrast, are more likely to contain relatively higher levels of CaO. Regardless of specific composition, the primary components of fly-ash are always SiO_2, Al_2O_3, Fe_2O_3, and CaO [5].

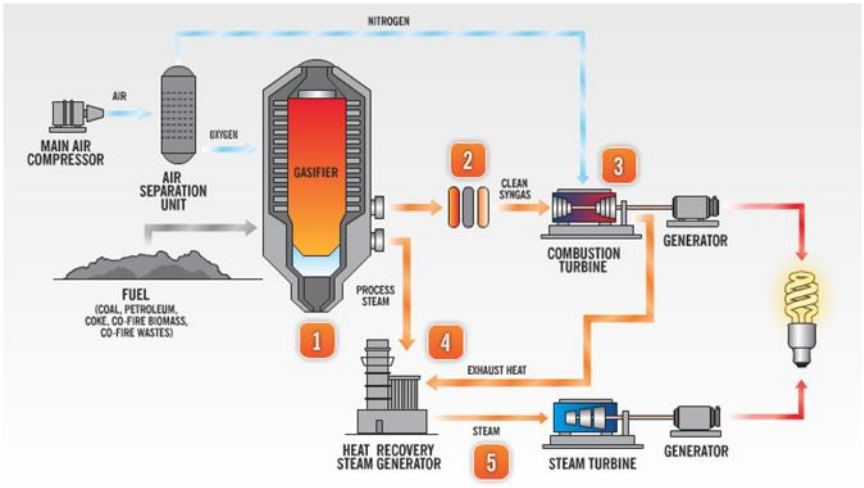

Figure 1: Schematic of IGCC system. Coal-based syngas is cleaned and burned in the combustion turbine [12].

1.2 TBC Systems used in gas turbines

Since the inception of gas turbines, the need for higher efficiency has prompted a continuous increase of operating temperatures, eventually exceeding the capabilities of the metallic materials typically used as structural components. This has led to the development of Thermal Barrier Coatings (TBCs) [13, 14], which consist of a ceramic topcoat and a metal bondcoat applied to a single-crystal, nickel-base superalloy substrate (Figure 2a). The γ-γ' superalloy is designed to withstand creep and fatigue in a temperature range extending to about 1000 °C. Good mechanical properties are obtained from both precipitation of cuboidal γ'-Ni_3Al and solid-solution strengthening of the γ-Ni matrix [15]. Alloy compositions associated with this microstructure do not impart, however, satisfactory corrosion resistance at high temperatures, mainly due to the relatively low aluminum content (5-6 wt. %) and to the presence of refractory elements such as molybdenum or tungsten.

Protection against corrosion in the harsh turbine environments relies on the formation of an Al_2O_3 scale by selective oxidation of the aluminum contained in the bondcoat. Maintaining a compact and adherent thermally grown oxide (TGO) also facilitates the junction between the metal substrate and the ceramic topcoat, which have limited compatibility in terms of thermal expansion. Two main types of bondcoat are currently used: Pt-modified β-NiAl and γ-γ' coatings, obtained by aluminization or Pt deposition followed by a diffusion heat treatment, are mostly found in aero engines; β-γ MCrAlY (M=Ni,Co) coatings, elaborated by plasma spray or electrodeposition, are commonly used in land-based turbines. Figure 2b shows a typical MCrAlY overlay bondcoat, where the Al-rich β phase (darker) acts as an Al reservoir to form Al_2O_3 [16].

(a)

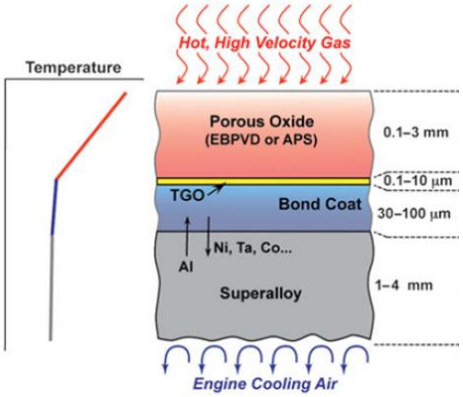

(b)

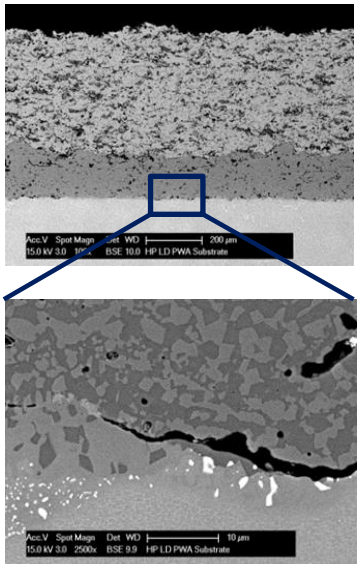

Figure 2: (a) Schematic of a thermal barrier coating showing the four different layers [17]. (b) SEM micrographs showing different regions of typical air plasma sprayed TBC. The darker (β) phase in the two-phase bond coat is responsible for alumina scale growth.

Beyond corrosion related issues, maximal temperatures encountered in service possibly exceed the γ' solvus in the superalloy (~ 1200 °C), which threatens the integrity of the structural component. Associated with internal cooling, the ceramic topcoat provides the thermal gradient necessary to protect the substrate, lowering the metal temperature by 100-150 °C [18]. This top coat is typically made from zirconia (ZrO_2) that is stabilized with yttria (Y_2O_3). Yttria stabilized zirconia (YSZ) has been widely used because of the low thermal conductivity of ZrO_2 (shown in Figure 3a), a relatively high coefficient of thermal expansion (CTE), excellent adhesion to the Al_2O_3 layer, and high strain tolerance [14, 16, 19]. Two types of TBCs are used depending on the method of top coat deposition: electron beam physical vapor deposition (EB-PVD) or air plasma spray (APS). EB-PVD top coating can be deposited on overlay or diffusion bond coats, and are primarily used in jet engines. They are characterized by distinct vertical columns that exhibit excellent strain tolerance in thermal cycling [20]. APS coatings are deposited on overlay bond coats. They are typically characterized by horizontal splats that form as molten YSZ cools and solidifies after deposition. The conventional splat morphology, as shown in Figure 2b, provides APS TBCs with lower thermal conductivity than EB-PVD TBCs at the expense of reduced strain tolerance [21]. A variant of the APS top coat is the dense vertically cracked (DVC) top coat which incorporates large intentional cracks to impart enhanced strain tolerance while retaining the relatively lower thermal conductivity of an APS coating. Both types of APS TBCs are primarily used in land-based turbines for power generation because of a relatively lower cost and the ability to coat large components [17].

A portion of the zirconia-yttria phase diagram is shown in Figure 3b. Pure zirconia can exist in three phases: monoclinic, tetragonal, and cubic. The cubic phase that is

obtained with high amounts of Y_2O_3 has low fracture toughness and is not suitable for TBCs that experience thermal cycling [16]. The equilibrium tetragonal phase would be suitable for TBC application, but it is subject to a transformation to monoclinic upon cooling. This transformation is undesirable because it undergoes a volume expansion (~3-4%) that causes cracking and eventually TBC spallation [22]. For this reason, there is a desire to retain (or stabilize) the tetragonal phase at all temperatures. When a composition of approximately 7wt% Y_2O_3 (7YSZ) is rapidly deposited using either APS or EB-PVD methods, a metastable tetragonal phase (commonly referred to as t') is formed at room temperature. When this t' phase is heated into the two phase (t+c) region it is thermodynamically driven to separate into equilibrium tetragonal and cubic phases. This phase separation, however, is kinetically limited due to the extremely slow diffusion of cations in ZrO_2. Thus the t' phase is retained at all temperatures up to around 1200°C, making it ideal for TBCs in this temperature range. The driving force for phase separation above 1200°C leads to degradation of the TBC at these higher temperatures, and new materials will be required as these temperatures are realized in the future [16]. However, 7YSZ is currently the most commonly used material for TBCs at operating temperatures ≤1200°C.

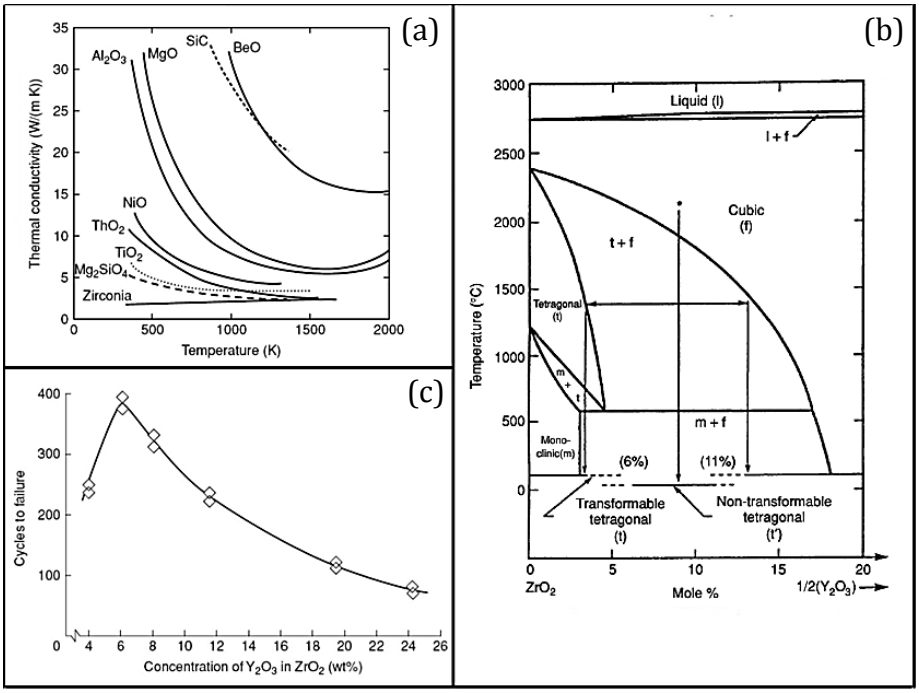

Figure 3: Properties of zirconia. (a) Its low thermal conductivity makes it an excellent TBC top coat material. (b) A portion of the ZrO_2-Y_2O_3 phase diagram shows three possible phases of zirconia. Stabilization of the tetragonal phase with ~7wt. % Y_2O_3 (roughly 7-8 mol % $YO_{1.5}$) improves fracture toughness, leading to (c) increased lifetime in thermal cycling [23].

Failure mechanisms can vary for APS and EB-PVD TBCs due to the different top coat and bond coat structures [19, 24]. The stress state generally changes in the top coat with temperature. The difference in coefficient of thermal expansion (CTE) between the top coat

and the substrate causes in-plane compressive stress in the YSZ when the TBC is cooled down from the top coat deposition [19]. Some viscoelastic deformation of the bond coat typically occurs to relieve a portion of this stress. The stresses are the greatest at this YSZ/bond coat interface where the surface is rumpled. Failure is typically associated with TGO growth and usually occurs at or near the TGO [18]. TBC lifetime depends on factors such as maximum operating temperatures, temperature gradients experienced in operations, thermal cycling, and deposit-induced attack [19]. TBCs typically fail when cracks form and propagate in the top coat, causing the YSZ to delaminate and spall off. Since the TBC is not self-healing, once the spalling has occurred the life of the TBC is over [20]. Turbine components, however, could be left in service after top coat delamination; this would expose the underlying bond coat to the harsh operating temperatures (and potentially to the buildup of deposits) before the failed TBC is replaced.

TBC failure is classified into two broad categories: intrinsic mechanisms that arise from factors within the TBC system, and extrinsic mechanisms that arise from external factors [25]. Intrinsic failure can originate from strain misfits between TBC layers during changes in temperature and can be affected by impurities in the TBC [25]. Cracking in the top coat typically originates at imperfections or defects and propagates during thermal cycling. Extrinsic failure mechanisms result from the top coat being damaged by elements outside the TBC system. These types of failures are inherently different from intrinsic failure mechanisms in that they result from a "top-down" attack that originates on the TBC top coat, rather than a delamination originating from within the TBC [25]. Failure due to extrinsic mechanisms can dramatically shorten the lifetime of TBCs. This type of failure generally falls into two categories: erosion or foreign object damage (FOD), and infiltration of molten deposit into the YSZ [26, 27]. Erosion is the result of foreign particles like sand or particles that have broken loose from other components in the system. These particles hit the YSZ and cause small cracks that propagate near the surface leading to delamination. FOD failure is similar to erosion except that is generally involves larger objects [28].

TBCs are often exposed to deposit-induced attack which involves calcia-magnesia-alumina-silicates (CMAS) [29, 30]. At very high temperatures (>1250°C), these types of deposits melt and the liquid melt infiltrates the porous YSZ causing early TBC failure. The damage caused by this CMAS infiltration is generally classified into two categories: thermo-chemical effects and thermo-mechanical effects [31, 32]. Thermo-chemical effects typically involve a chemical interaction between the melt and the YSZ that changes the 7YSZ structure. In some cases, the molten CMAS can melt the YSZ and re-precipitate it with a different composition (less Y_2O_3) that causes destabilization of the t' phase [33]. This is also characterized by a drastically different morphology that does not resemble either horizontal splats (in APS) or columns (in EB-PVD), but rather "globules" of YSZ that are surrounded by solidified CMAS melt [32, 34]. The solubility of YSZ in molten CMAS depends on the ratio of oxides in the deposit, and in some cases the CMAS melt does not dissolve YSZ. The liquid CMAS does, however, infiltrate the YSZ where it changes the overall mechanical properties of the top coat. These thermo-mechanical effects can lead to dramatic changes in elastic modulus and strain tolerance [5, 31]. The resulting stress can cause cracking and spallation within the top coat. This is often characterized by cracking in the middle of the top coat itself, rather than at the YSZ/bond coat interface.

One aspect of laboratory CMAS studies that is not often discussed in the literature is

the effect of sulfates (Na_2SO_4 and K_2SO_4) that are almost always found in such deposits. At very high temperatures where CMAS deposits become molten (>1250°C), these minor constituents would volatilize quickly and therefore are typically not considered. However, at lower temperatures (900-1100°C) liquid sulfates are more likely to cause detrimental effects on the TBC. Previous studies have found that exposure to Na_2SO_4 do not degrade 7YSZ [35]. The presence of V_2O_5, however, is well-known to leach Y_2O_3 from the YSZ with the formation of YVO_4 which cause destabilization of the t' phase [36]. This destabilization is accelerated in an SO_2-SO_3 containing atmosphere. The formation of YVO_4 is further enhanced by exposure to Na_2SO_4 in addition to V_2O_5 because of the formation of $NaVO_3$, which reacts with Y_2O_3 more readily to form YVO_4 [37].

Early TBC failure can also be affected by different gas environments. The YSZ top coat is known to be susceptible to early spallation caused by moisture in the atmosphere [38]. Two types of moisture-induced failure have been widely reported. A very rapid delamination of the YSZ top coat has been identified upon application of water droplets at room temperature on TBCs that had been subjected to thermal cycling [39]. This moisture-induced delayed spallation (MIDS) is attributed to water molecules adsorbing on the TBC near a crack at the YSZ/TGO interface. The adsorbed molecules disassociate into OH^- ions that react with the TGO, and H^+ ions that diffuse into the metal. The H^+ ions then travel into the crack where they induce crack propagation at the scale/metal interface that leads to delamination of the top coat [38, 39, 40]. Another moisture-induced early failure mechanism in TBCs occurring around 200-400°C is commonly referred to as low temperature degradation (LTD) [22, 41]. This mechanism involves OH^- ions diffusing through the YSZ lattice where they annihilate oxygen vacancies. These vacancies, that were created when the Y^{3+} ions replaced the Z^{4+} ions on the YSZ lattice, are responsible for the slow cation diffusion in the YSZ. The annihilation of these sites allowed for phase separation into equilibrium cubic and tetragonal phases, and the subsequent transformation to monoclinic that leads to early failure [42].

Microstructural evolutions occur in the bondcoat due to both Al removal from the subsurface by selective oxidation, and interdiffusion with the superalloy substrate, driven by differences in chemical potentials. Stress caused by thermal cycling may cause spallation of the Al_2O_3 scale, exposing an Al-depleted surface. This will eventually result in the rapid formation of nickel or cobalt oxides, or breakaway, when the surface Al content is too low for a new Al_2O_3 layer to form.

The oxidation behavior is influenced by the presence of secondary oxidants in the gas atmosphere in a variety of ways. Carburization strongly affects Cr_2O_3-forming alloys, and accelerates the onset of breakaway even at the low carbon activities typical of CO_2-rich combustion gases [43]. However, Al_2O_3 is a better barrier to carbon than Cr_2O_3, and provides efficient protection against carburization [44]. Water vapor poses an important threat to Cr_2O_3-formers, mostly because of significant Cr_2O_3 volatilization in the presence of H_2O [45, 46, 47]. The partial pressure of aluminum hydrate is low, and Al_2O_3 evaporation is unimportant at the temperatures of interest [48]. If no significant effect of water vapor is reported in isothermal conditions, Al_2O_3 spallation during thermal cycling is greatly enhanced in the presence of H_2O [49, 50].

Additional modes of degradation may occur if the YSZ topcoat is removed or otherwise allows condensed species present in the environment to access the bondcoat. In

particular, hot corrosion is a potentially severe form of accelerated attack by molten sulfates, and has long been recognized as an important concern in the operation of gas turbines for aircraft or marine propulsion [51, 52]. Mechanistic aspects of the corrosion process, as well as alloy and coating compositional factors and mitigation strategies, have been described in several reviews [53, 54, 55, 56, 57]. Two temperature regimes are distinguished based on the melting point of the deposited sulfate, typically Na_2SO_4 (T_m = 884 °C): type I at temperatures above T_m, and type II below T_m. In type II conditions, a minimum amount of SO_3 is required in the gas to stabilize the sulfate of an alloy constituent (typically Ni or Co) and produce a low melting mixture with Na_2SO_4. No hot corrosion is expected below the eutectic temperature (e.g., T_e (Na_2SO_4-$NiSO_4$) = 671 °C, T_e (Na_2SO_4-$CoSO_4$) = 565 °C). Conversely, sulfates evaporate rapidly at elevated temperatures, such that dry corrosion prevails above about 1000 °C. Essentially, hot corrosion occurs as oxides which would otherwise form compact scales on an alloy surface are dissolved in the molten salt. Depending on the particular conditions, both Al_2O_3 and Cr_2O_3-forming alloys are potentially affected. Understanding the effect of alloying elements and designing resistant alloys are made difficult by the extreme complexity of the reaction mechanisms involved; however, empirical evidence shows that good resistance is reached by MCrAlY alloys with high chromium contents [55].

Hot corrosion is concerned with degradation of the bondcoat material from sulfates at temperatures in the range of 700-900°C, whereas CMAS is concerned with degradation of YSZ from silicates at temperatures around 1200-1300°C. The scope of this work is to examine the degradation of both top coat and bondcoat at temperatures around 1000-1100°C. Fly-ash degradation, as shown in Figure 4 compared to CMAS and hot corrosion, can involve damage from all constituents of the deposit (oxides and sulfates) at these intermediate temperatures.

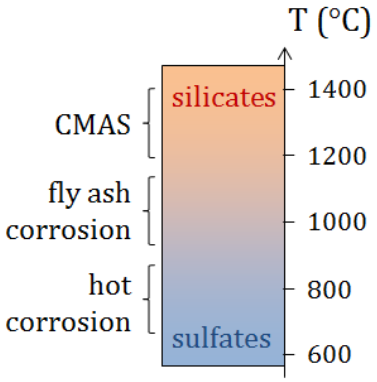

Figure 4: Fly-ash corrosion compared to CMAS and hot corrosion.

2 Materials and Experimental Methods

2.1 Top coats

Testing was conducted on the two different types of APS TBCs provided by Praxair Surface Technologies shown in Figure 5. Nominal densities for DVC and HPLD coatings were 92% theoretical density (T.D.) and 85% T.D., respectively. Both top coats were deposited to a thickness of 15 mils onto dual layer NiCoCrAlY overlay bond coats of thickness of 7-8 mils. All top coats were made from high purity YSZ. Previous studies have shown that these high purity TBCs exhibited excellent resistance to sintering and phase separation at operating temperatures around 1100°C [58]. This was accomplished by controlling impurities such as silica and alumina in the YSZ powder during manufacturing [59]. The HPLD TBCs are characterized by the horizontal splat morphology, and the DVC top coats exhibit vertical cracks in the relatively dense YSZ. Figure 5 shows the TBCs in the as-processed condition, and the TGO formed between the top two layers in processing is virtually indistinguishable at this magnification. This TGO layer thickens at high temperatures, as can be seen in later Figures. Both types of TBCs are deposited on 2nd generation nickel-based superalloys. Two different substrate alloys were used (PWA1484 and Rene N5) that were specifically chosen because they are commonly used in turbine blade manufacturing. These two superalloys were also very similar in composition, and therefore any effects of the substrate (such as interdiffusion with the bond coat) would be very similar for the two different TBCs.

Free-standing DVC specimens were also used for testing. The purpose of testing with free-standing YSZ was to examine chemical interaction with fly-ash deposits before testing with complete TBC systems. Mechanical testing (3-pt. bend test) could also be done on free-standing samples to examine overall effects of fly-ash on top coat properties (elastic modulus, coefficient of thermal expansion).

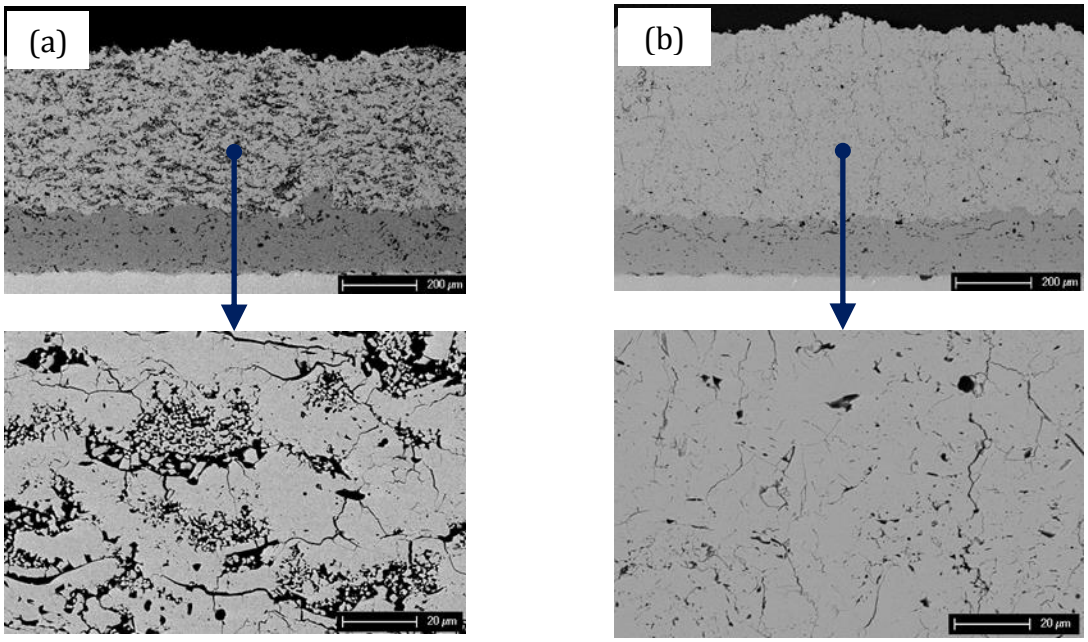

Figure 5: Two types of air plasma sprayed 7YSZ top coats used for testing in the study. (a) Conventional high-purity low-density top coats, and (b) Dense vertically cracked top coats.

2.2 Bondcoats

Corrosion of the bondcoat material was studied using cast NiCoCrAlY alloys. All ingots were made by argon-arc melting, followed by drop casting into 10 mm diameter rods that were then homogeneized in vacuum for 6 h at 1200 °C plus another 48 h at 1150 °C. All processing was conducted at the Materials Preparation Center of the Ames Laboratory [60]. A series of six model alloys were prepared with a constant 30 at. % Co and systematically varied Al and Cr contents. As shown in Figure 6, these alloys have relatively low Al and high Cr, which places them in the γ-rich part of the β-γ two-phase field at 1100 °C; small amounts of σ were present in the alloys with the highest Cr contents. Phase compositions and fractions measured after 50 h annealing at 1100 °C are given in Table 1. These γ-rich compositions were chosen to ensure good resistance to hot corrosion, on the basis of preliminary results. A cast version of Ni-19Co-15Cr-24Al (all alloy compositions are in at. %), a more typical bondcoat composition used in TBC systems, was also made to provide a baseline for comparison. Two variants with slightly different Y contents, 0.1 and 0.3 at. %, were used in order to evaluate the importance of controlling the amount of reactive elements in industrially processed coatings. The microstructures of the γ-rich and β-rich alloys at 1100 °C are shown in Figures 7 and 8, respectively. Bright yttrium-rich intermetallics are seen to be present in greater fraction in the higher Y version of the β-rich alloy. Little or no yttrides precipitated in the γ-rich alloys, probably reflecting a higher solubility of Y in γ.

Specimens approximately 1 mm thick were cut from the heat-treated rods, ground using SiC paper to a P1200-grit finish, then degreased with detergent and ultrasonically cleaned in ethanol before exposure.

#	Ni	Co	Cr	Al	Y
1	42	19	15	24	0.28
2	42	19	15	24	0.1
3	31	30	27	12	0.1
4	28	30	30	12	0.1
5	25	30	33	12	0.1
6	27	30	27	16	0.1
7	24	30	30	16	0.1
8	21	30	33	16	0.1

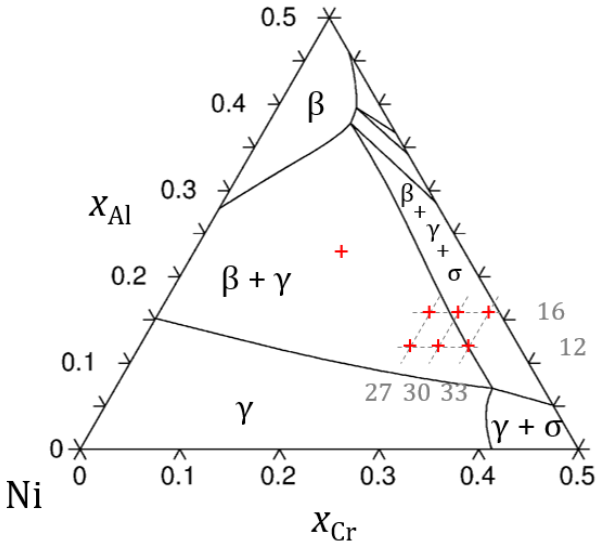

Figure 6: Nominal composition (at. %) of the NiCoCrAlY alloys and isotherm (1100 °C) isopleth (x_{Co}=0.3) pseudo-ternary section of the NiCoCrAl phase diagram, calculated using Thermo-Calc [61] and the NIST 2000 Superalloy database [62] (from X. Liu and Z.-K. Liu, Pennsylvania State University). Alloy compositions are indicated with red markers. The Ni-19Co-15Cr-24Al alloy is slightly off-plane, as is contains less Co than the isopleth value.

Table 1: Measured phase compositions (SEM-EDS) and phase fractions (image analysis) of the γ-rich alloys used in this work after 50 h heat treatment at 1100 °C. Measurements were done away from the specimen surfaces to avoid oxidation-induced microstructural evolutions.

#	γ					β					σ				
	at. %				vol. %	at. %				vol. %	at. %				vol. %
	Ni	Co	Cr	Al		Ni	Co	Cr	Al		Ni	Co	Cr	Al	
3	29.1	31.7	29.5	9.7	87	40.1	17.3	9.7	33.0	13					
4	26.0	32.4	33.2	8.5	84	37.9	18.3	11.5	32.3	16					
5	22.3	32.0	37.5	8.2	81	34.3	18.8	13.6	33.3	18	10.8	27.8	58.1	3.3	1.0
6	22.4	34.4	34.8	8.4	66	34.7	20.6	11.6	33.1	34					
7	19.9	34.9	37.3	7.8	59	32.1	21.7	13.9	32.4	40	9.6	29.5	57.5	3.3	1.6
8	18.4	36.6	37.4	7.6	36	30.6	23.2	14.2	32.0	42	8.9	30.5	57.2	3.3	22

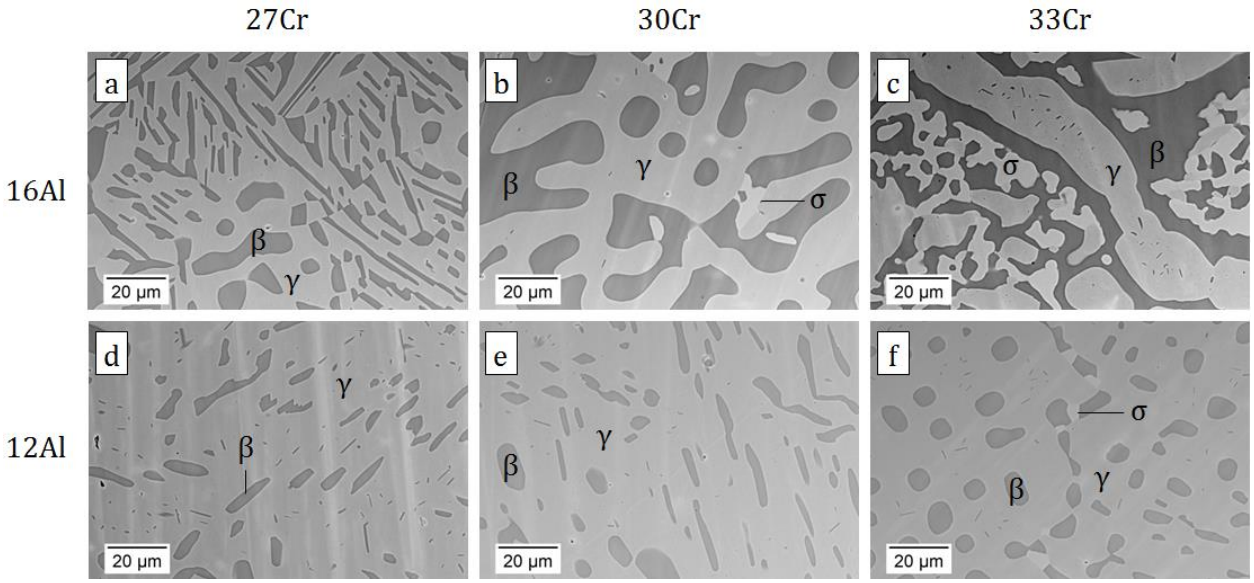

Figure 7: Microstructure of the γ-rich Ni-30Co-xCr-yAl-0.1Y alloys, observed by SEM after 50 h annealing at 1100 °C. (a) 27Cr-16Al; (b) 30Cr-16Al; (c) 33Cr-16Al; (d) 27Cr-12Al; (e) 30Cr-12Al; (d) 33Cr-12Al.

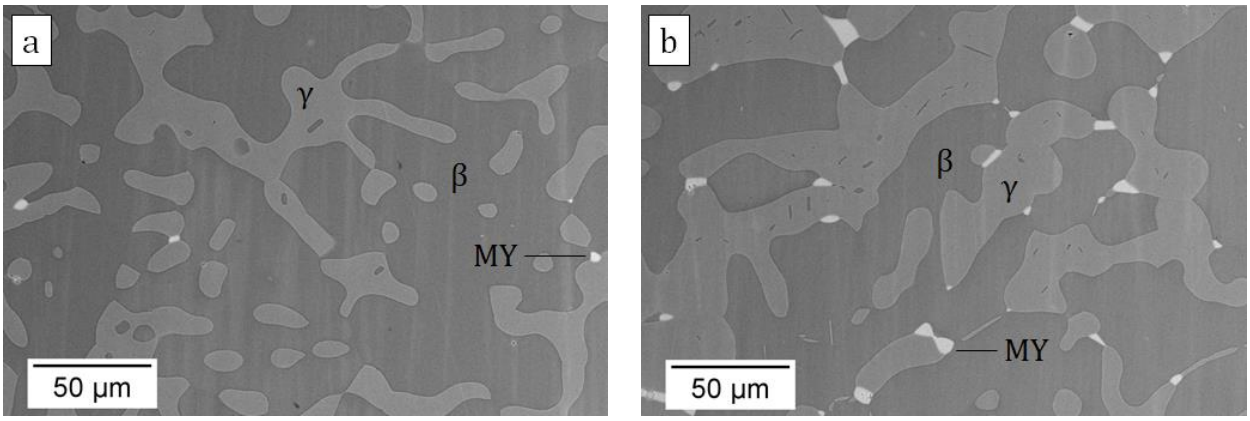

Figure 8: Microstructure of the β-rich Ni-19Co-15Cr-24Al-zY alloys, observed by SEM after 50 h annealing at 1100 °C. (a) 0.1 Y; (b) 0.3 Y.

2.3 Experiments

Two different horizontal tube furnaces were used in the configuration described in Figure 9 for testing of free-standing YSZ and complete TBC systems. A Thermo Scientific three zone furnace was used for isothermal exposures at 1100°C, and an Applied Test Systems (ATS) single zone furnace was used for cyclic exposures between 1100°C (45 minutes) and 160°C (15 minutes). Both furnaces were capable of maintaining gas atmospheres containing dry air, CO_2, SO_2, or steam by using glass end caps that were sealed to both ends of the furnace tubes. Samples traveled horizontally using a magnet outside of the glass end cap that forced a metal slug to move the sample rod. The opposite end of the sample rod was attached to the sample holder (alumina boat) with Kanthal wire. Moving

samples with a magnet was done manually for the isothermal furnace. The cyclic apparatus utilized a ball nut that traveled along a rotating ball screw to move the magnet. This was operated automatically using a programmable controller.

Steam containing atmospheres were achieved using a water bath with bubbler followed by a condenser. The reaction gas passing through the bubbler submersed in a water bath would absorb an amount of steam that depended on the temperature. For atmospheres containing 20% steam, a temperature of 60°C was desired. The water bath, however, would be set at 62°C, in order to slightly over-saturate the gas. This over-saturated gas would then travel through the condenser that was maintained at the desired temperature of 60°C. The main advantage of this process was that the condensation of excess steam could be monitored on the walls of the condenser in order to verify the steam content was accurate. The gas, now containing the appropriate amount of steam, would be flowed to the reaction furnace using copper tubing that was wrapped in heat tape to avoid condensation of steam before reaching the reaction tube.

Thermal cycling in the horizontal tube furnace was done with three complete TBCs at a time. This was determined to be the maximum number of TBCs that could reasonably fit in the hot zone of the furnace, and also the maximum number that could be reliably cycled with the magnetic system given the weight of each sample. TBCs were subjected to the same gas atmosphere in the reaction zone as they were outside the furnace. The end cap would typically be open and TBCs exposed to lab air every 160 cycles in order to inspect the experimental setup and maintain the integrity of the sample holder and rod. Thorough inspection of TBCs could also be done to determine failure. Samples would also be monitored by inspection through the clear end cap while the samples were cycled out of the furnace. Partial spallation of YSZ top coat was often observed, but complete TBC failure was determined when the entire top coat (or what was left after partial spallation) delaminated from the substrate.

Thermal cycling in lab air was done with a bottom loading CM furnace. Thermal cycles in the bottom loading furnace consist of a 10 minute ramp to 1100°C, followed by a 45 minute hold at 1100°C, and then a 10 minute cooling period in forced air to 60°C. This testing cycle represents a more harsh thermal cycle compared to thermal cycling in the horizontal tube furnace because the temperature change is both greater in magnitude and more rapid. The disadvantage, however, is that the gas atmosphere cannot be controlled.

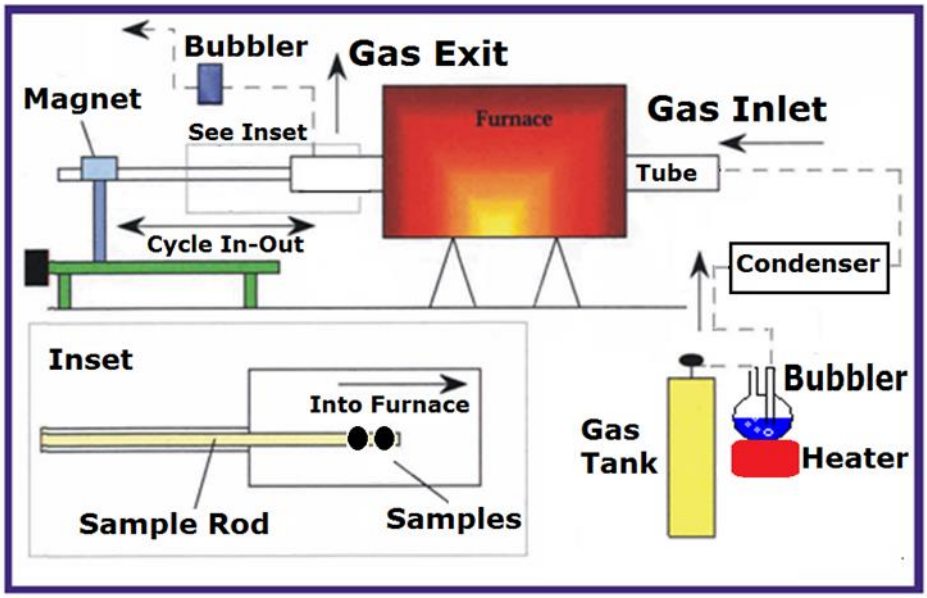

Figure 9: Experimental setup for cyclic and isothermal experiments in horizontal tube furnace capable of controlled gas atmospheres.

Fly-ash was deposited on the top surface of all samples before thermal exposure. This was done by mixing a deposit with ethanol to create a slurry. The slurry would then be applied to the sample with a dropper and allowed to dry. Samples would be weighed before and after slurry application to ensure that a deposit loading of 35 ± 5 mg/cm^2 was achieved. In some cases synthetic fly-ash was also ball milled before reaction with YSZ to obtain smaller, more uniform particle distribution. Experiments were done to examine the effects of the ball milling process on reaction with YSZ, and no effect of the ball milling was observed. Ball milling was not determined to be an important factor in the observed reaction products, and was not considered any further.

Model fly-ash deposits were prepared by mixing oxide and sulfate powders in the desired proportions, and crushing the mixtures using a mortar and pestle. Free-standing YSZ was reacted with three synthetic ash mixtures of the same composition: 1. Synthetic ash that was not heat treated prior to exposure, 2. Synthetic ash that was heat-treated at 1200°C before exposure, and 3. Synthetic ash that was melted at 1500°C and then crushed into a powder before exposure. The reaction product shown in Figure 14b was formed with the heat treated (1200°C) ash. Figure 10 shows the reaction layers formed during exposure to the other two high-CaO synthetic ashes. The same reaction layer was formed in all three exposures. This provided important verification of the synthetic ash mixture being used was representative of a fully melted oxide mixture that would be similar to an actual fly-ash, and heat treatment did not affect the formation of the $CaZrO_3$ layer. All other exposures with YSZ and complete TBCs were done with pre-heat treated (1200°C) synthetic ash.

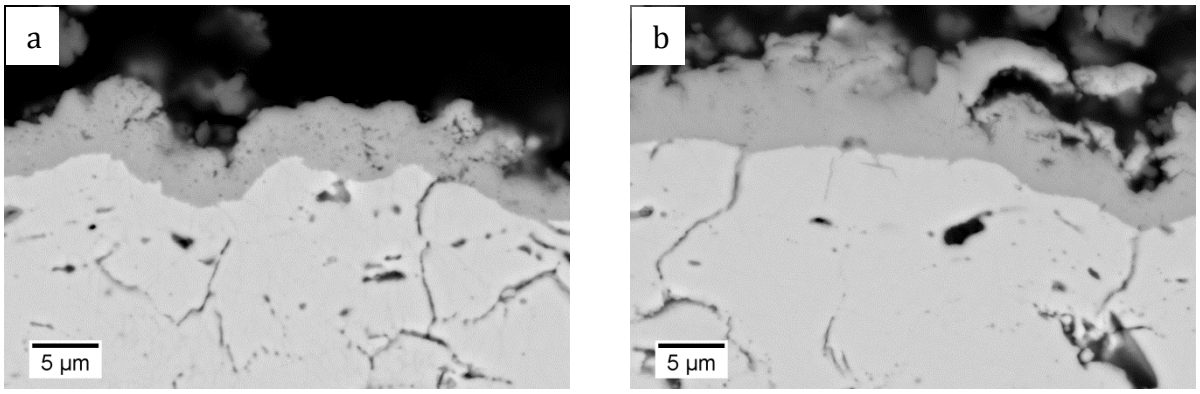

Figure 10: Free-standing YSZ was reacted with (a) pre-melted fused ash, and (b) individual oxide powders that were mixed together and not heat-treated, in dry air for 72 hours at 1100°C.

Isothermal testing of the bondcoat materials was conducted in a one-zone, horizontal furnace from Thermo Scientific. The same methods as described above were used to generate and flow controlled gas atmospheres, to move samples horizontally in and out of the furnace hot zone, and to apply deposits on the samples. Model fly-ash deposits were prepared using the same technique described for the free-standing YSZ and complete TBC samples. Figure 11 shows the corrosion products obtained after reaction of the γ-rich alloy Ni-30Co-30Cr-12Al-0.1Y with a commercial class C fly ash from a conventional coal-fired power plant (Scherer, GA) described in Table 2, and a model ash mixture of the same composition. The corrosion products, which will be described in detail in Section 3.2.2, do not present any significant difference. This justifies the use of model ash mixtures to simulate fly ash corrosion.

Corrosion experiments were performed at 900 and 1100 °C in flowing gas mixtures of the following compositions (vol. %): N_2-21O_2 (dry air), CO_2-20H_2O, CO_2-20H_2O-1.6O_2, and O_2-0.1SO_2. Linear gas flow rates were about 2 mm s^{-1} at reaction temperature, with a total pressure slightly over 1 atm. The O_2-SO_2 mixture was passed through a Pt honeycomb catalyst located directly upstream of the specimens in the hot zone, allowing the otherwise sluggish reaction

$$SO_2 + \frac{1}{2}O_2 = SO_3 \quad (1)$$

to proceed.

Table 2: Composition of Class C Fly-Ash (wt%)

	CaO	SiO_2	Al_2O_3	Fe_2O_3	MgO	Na_2SO_4	K_2SO_4
Wt%	33.4	26.4	20.1	6.1	8.0	5.2	0.7

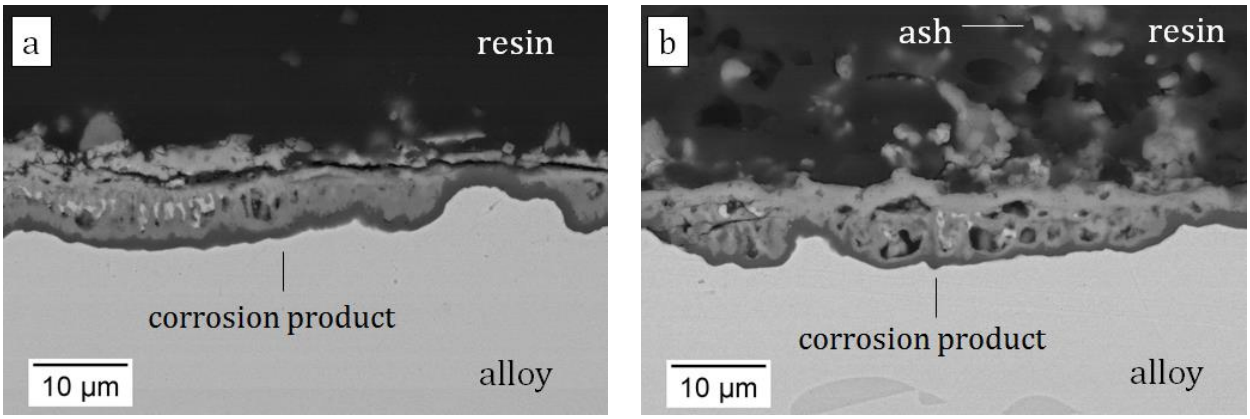

Figure 11: Reaction morphology observed after 50 h exposure of the γ-rich Ni-30Co-30Cr-12Al-0.1Y alloy with (a) commercial and (b) model class C fly ash in CO_2-20H_2O at 1100 °C. Ash composition (wt. %): 26SiO_2, 20Al_2O_3, 34CaO, 6Fe_2O_3, 8MgO, 5Na_2SO_4, 1K_2SO_4.

2.4 Characterization Techniques

After reaction, samples were mounted, cut, and polished to 1 μm using oil-based products to avoid the loss of any water-soluble products. Polished cross sections were examined using a JEOL model JSM6510 scanning electron microscope (SEM). The SEM was equipped with electron dispersive x-ray spectroscopy (EDS) for elemental analysis. EDS was capable of obtaining spectra in specific locations as well as elemental mapping over larger regions. SEM micrographs were primarily used to characterize oxide scale formation and TBC failure. In some cases, Raman spectroscopy was also used on mounted TBC specimens to identify YSZ phases. The cubic, tetragonal, and monoclinic phases each have unique Raman spectra [63]. The occurrence of these different peaks can be used to determine the presence of each phase. Similarly, oxidized surfaces were examined by photo-stimulated luminescence spectroscopy, which allows γ, θ and α polymorphs of Al_2O_3 to be distinguished [64], using a 633 nm HeNe laser in a Renishaw inVia Raman microscope.

The elastic modulus of free-standing YSZ was determined using three point bend testing. Testing was done with YSZ samples (1”x.25”x.03”) that had been heat treated for 72 hours. A total of 8 samples were tested: 4 that were heat treated without deposit, and 4 that were reacted with a synthetic fly-ash deposit. Modulus testing was done by Innovative Test Solutions (ITS) in Schenectady, New York.

3 Results and Discussion

3.1 YSZ Top Coat and Complete TBCs

3.1.1 Reaction between Commercial Fly-Ash and 7YSZ

Free-standing DVC samples were tested with the commercial class C fly-ash. Figure 12a shows extensive degradation of the YSZ after reaction at 1300°C in dry air. The fly-ash was infiltrated with molten ash constituents, and the microstructure of the YSZ was completely changed near the surface. The dense YSZ structure was transformed into globular regions surrounded by solidified fly-ash. The Raman spectra shown in Figure 13 indicate the absence of t' phase in the globular YSZ. Similar degradation had been documented as a result of CMAS melt dissolving the 7YSZ and then re-precipitating globules of Y-lean YSZ [34] that transform to monoclinic upon cooling.

The temperature dependence of the reaction with class C fly-ash and YSZ was studied at 1200°C and 1100°C in dry air. The reaction at 1200°C did not change the overall microstructure (like in the globular formation at 1300°C), and thus did not appear to involve molten fly-ash penetration into the YSZ. The exposure resulted in a continuous, dense reaction product that varied between 5 and 10 microns in thickness and did not infiltrate significantly into the smaller cracks and pores. This complex reaction layer shown in Figure 12b contained a number of ash constituents but consisted predominantly of Ca, Si, Al, Fe, and Zr.

Exposure of YSZ to class C ash at 1100°C in dry air is shown in Figure 12c. Unlike the 1200°C exposure, a continuous reaction layer was not formed at the surface. Examination of sub-surface cracks, however, revealed some infiltration of ash constituents in the YSZ (indicated by arrows in the Figure). This was the result of some partial melting in the ash. All known eutectic compositions between the oxides in the ash are above 1100°C. Therefore this liquid formation likely involved minor fly-ash constituents such as Na_2SO_4 and K_2SO_4. EDS analysis indicated that the infiltrated regions contained Ca and Si. (Na and K were not observed, and likely would have evaporated at this temperature.) Known compounds formed between CaO and SiO_2 would not be liquid at 1100°C. This further indicated that other constituents were involved in the formation of liquids, and that CaO and SiO_2 were also important components in the infiltration. These results indicated a need to investigate CaO and SiO_2 combined with minor constituents such as Na_2SO_4 and K_2SO_4, as well as a need to control ash compositions by using synthetic fly-ash mixtures.

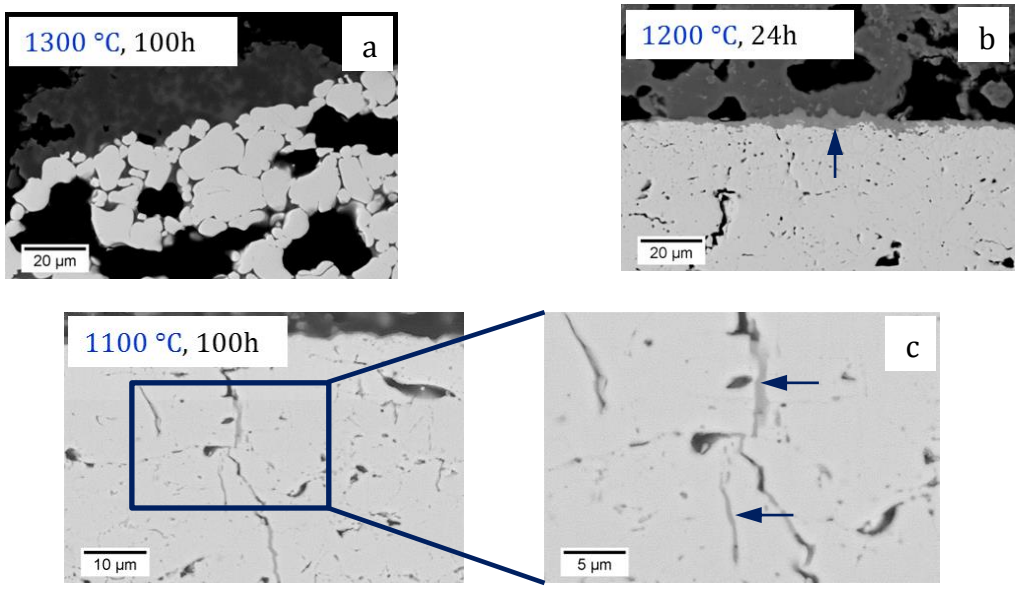

Figure 12: Reaction of commercial Class C fly-ash with free-standing DVC YSZ. (a) At 1300°C the ash has melted and completely infiltrated the YSZ. (b) At 1200°C the degradation was less extensive but a complex reaction layer was formed at the ash/YSZ interface. (c) At 1100°C there was no observable reaction layer, but some infiltration was observed in small cracks in the YSZ.

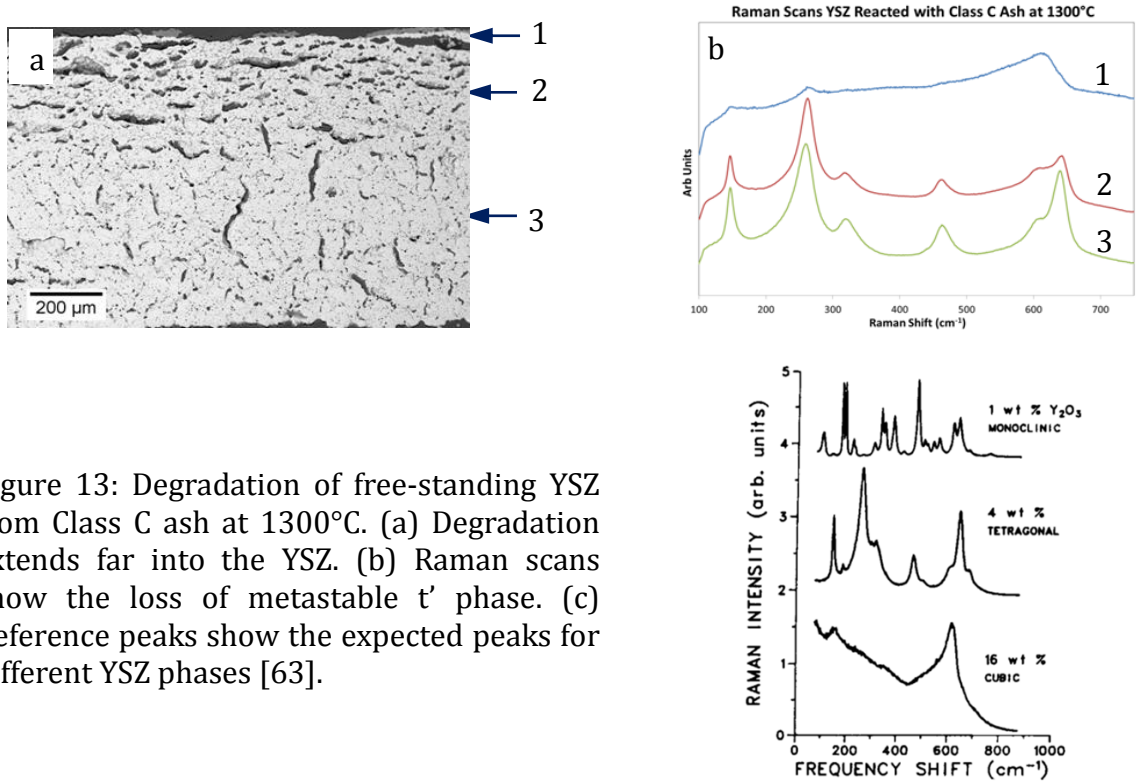

Figure 13: Degradation of free-standing YSZ from Class C ash at 1300°C. (a) Degradation extends far into the YSZ. (b) Raman scans show the loss of metastable t' phase. (c) Reference peaks show the expected peaks for different YSZ phases [63].

3.1.2 Reactions with Synthetic Fly-Ash

Synthetic fly-ash mixtures were made with oxides that are predominantly found in fly-ash (CaO, Al_2O_3, SiO_2, Fe_2O_3, MgO). The concentration of CaO was systematically varied, while the ratios of other oxides were kept constant. These synthetic fly-ash mixtures did not contain any minor constituents (Na_2SO_4, K_2SO_4, FeS). Two different synthetic fly-ash compositions described in Table 3 were reacted with free-standing DVC YSZ for 72 hours at 1100°C in dry air. The results shown in Figure 14 demonstrated that the low-CaO synthetic ash had no effect on the YSZ, whereas the high-CaO ash formed a dense reaction product. This product was identified as $CaZrO_3$ using XRD analysis, and this was verified by EDS analysis which showed equal molar ratios of Ca and Zr. The phase diagram shown in Figure 15 also showed formation of $CaZrO_3$ at 1100°C. The reaction layer was continuous along the YSZ surface and did not infiltrate into small cracks and pores of the YSZ, indicating that there was a solid-state reaction between the ash and YSZ. Further analysis (not shown) indicated that its growth was diffusion-controlled and it thickened with parabolic kinetics.

Table 3: Two different synthetic ash compositions exposed to YSZ at 1100°C

	CaO	SiO_2	Al_2O_3	Fe_2O_3	MgO
Low-CaO Ash (Wt%)	10	50	25	10	5
High-CaO Ash (Wt%)	70	18	9	2	1

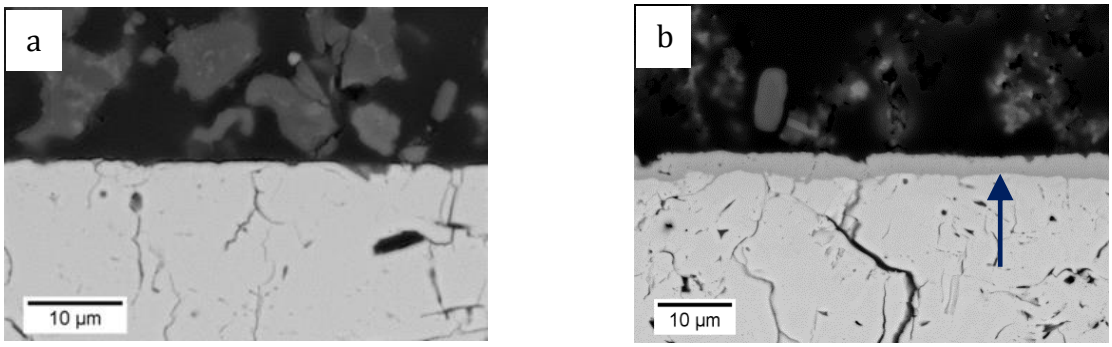

Figure 14: Exposure of free-standing YSZ to two different synthetic ash compositions described in Table 4. (a) Low-CaO ash did not react with the YSZ. (b) The arrow indicates a dense reaction layer that has formed between the YSZ and a high-CaO synthetic ash.

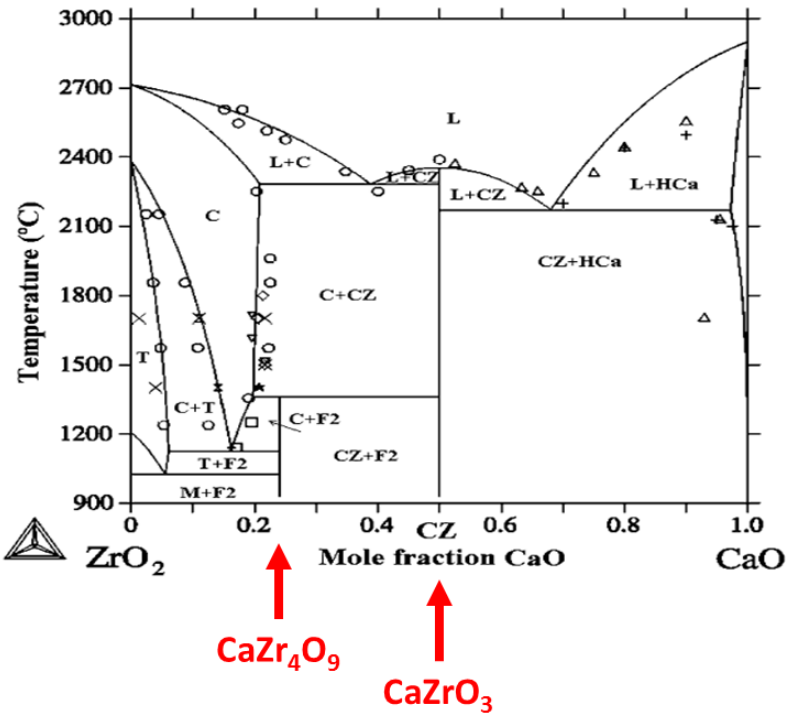

Figure 15: Partial phase diagram of the ZrO_2-CaO system. Two different compounds are possible at 1100°C.

The formation of a $CaZrO_3$ reaction layer on YSZ was the same for exposures with pure CaO and those with high-CaO synthetic ash. In both cases, the dense $CaZrO_3$ layer sealed the top surface of the YSZ and exhibited no penetration into small cracks below the YSZ surface. The consequences of this reaction layer on the overall TBC performance were examined in the bottom-loading cyclic furnace. A DVC TBC was reacted with pure CaO isothermally at 1100°C in dry air for 72 hours, and a continuous $CaZrO_3$ layer (approximately 5μm thick) was formed along the top surface. This TBC was then exposed to thermal cycling along with an as-processed TBC. The pre-formed $CaZrO_3$ layer did not cause TBC failure before 200 cycles. Figure 16 shows both TBCs after 200 thermal cycles. There were no observable differences that resulted from the presence of the reaction layer such as excessive cracking in the YSZ, depletion of β phase in the bond coat, or disruption of TGO growth. The only effect that the $CaZrO_3$ layer had on the top coat was that some regions had broken away from the surface (indicated in the figure by the arrow). This result shows that some of the YSZ would be consumed as it was used to form $CaZrO_3$ that spalled from the TBC, leaving the top coat somewhat thinner. However, the nature of $CaZrO_3$ kinetics would result in minimal loss of YSZ, and thus the existence of the $CaZrO_3$ layer along the top of the YSZ was considered relatively harmless to the overall TBC lifetime.

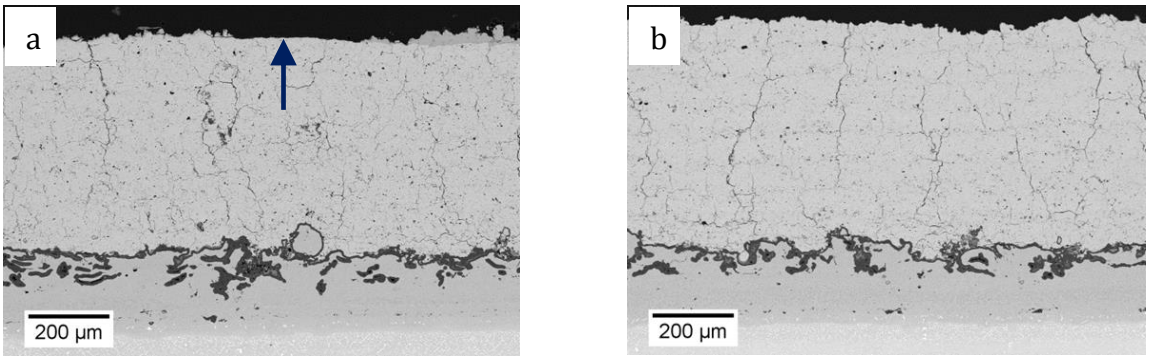

Figure 16: (a) Complete DVC TBC that has been thermally cycled in lab air after a $CaZrO_3$ layer was pre-formed compared to (b) an as-processed TBC that was cycled in the same conditions.

3.1.3 Addition of Sulfate to Synthetic Fly-Ash

Detrimental effects of the $CaZrO_3$ layer that would be formed with the high-CaO ash (oxides only) were not severe. Actual fly-ash, however, contains sulfates (K_2SO_4 and Na_2SO_4) from the coal and biomass fuel source as well as FeS from interaction between hot gases and metallic components upstream of the turbine. The effects of minor ash constituents were examined with the high-CaO synthetic ash. Figure 17 shows the high-CaO ash reaction at 1100°C for 72 hours in dry air, before and after addition of 10 wt. % K_2SO_4. The EDS mapping shows the penetration of Ca deep into the YSZ with the addition of K_2SO_4. The K_2SO_4, which melts at 1084°C, appeared to have infiltrated the YSZ and transported CaO into the cracks. Figure 18 shows in more detail the reaction of free-standing DVC YSZ with the ash described in Table 4. The liquid penetration filled the small crack tips and open pores far beneath the YSZ surface during reaction. This liquid K_2SO_4 was responsible for transporting CaO into these cracks where it formed $CaZrO_3$ in places where it contacted the YSZ.

Additional testing was done with additions of FeS and both FeS+K_2SO_4. Reactions with K_2SO_4+FeS resulted in the same infiltration as those with only K_2SO_4, and reactions with only FeS did not produce any infiltration. It was concluded that only K_2SO_4 was necessary for the infiltration of $CaZrO_3$ into cracks in the YSZ.

Table 4: High-CaO synthetic fly ash containing 10wt% K_2SO_4

	CaO	SiO_2	Al_2O_3	Fe_2O_3	MgO	K_2SO_4
Wt%	63	16.2	8.1	1.8	0.9	10

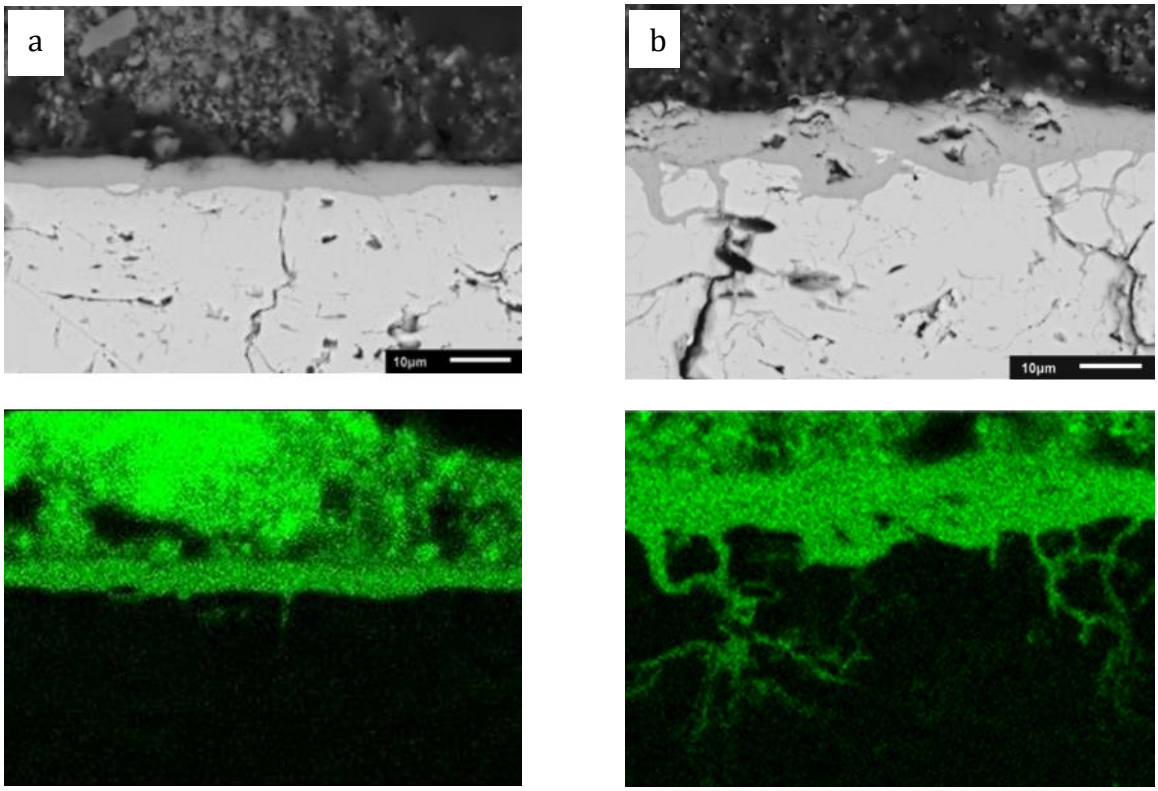

Figure 17: Free-standing YSZ that has been reacted with high-CaO synthetic ash containing (a) only oxides and (b) oxides with the addition of K_2SO_4.

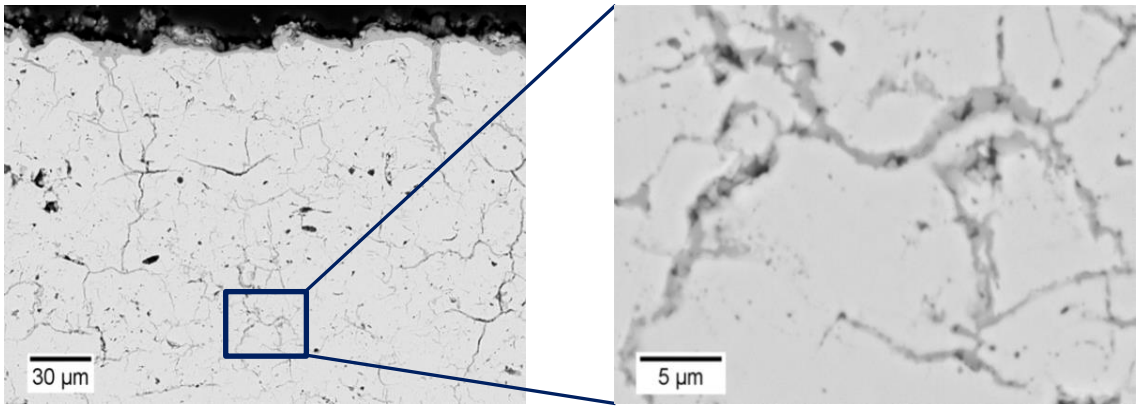

Figure 18: YSZ reacted with high-CaO synthetic ash that contains K_2SO_4 showing extensive infiltration of $CaZrO_3$ into cracks and pores.

The only oxide from the synthetic ash that reacted with YSZ was CaO, and this reaction was carried into the YSZ with the addition of K_2SO_4. In order to better understand this infiltration, mixtures of only CaO and K_2SO_4 were reacted with YSZ. Figure 19 shows the reaction of a 0.5CaO-0.5K_2SO_4 (wt. %) deposit with DVC YSZ for two different times.

EDS mapping was used to show relative concentrations of Ca, K, and S at both of these times. After a 1 hour exposure, strong signals of all three elements show that liquid K_2SO_4 infiltrated much of the YSZ and transported CaO with it. After 70 hours, however, the EDS mapping indicated that K_2SO_4 was almost completely gone and large amounts of Ca were retained in the YSZ cracks. Closer SEM analysis indicates that extensive $CaZrO_3$ infiltration was responsible for this Ca signal. An important observation here is that the extent of $CaZrO_3$ infiltration was the same for similar exposures to high-CaO synthetic ash and mixtures of only $CaO+K_2SO_4$. The additional oxides in the synthetic ash did not influence the $CaZrO_3$ infiltration.

The mechanism by which liquid K_2SO_4 transports the CaO into the YSZ was studied further with the exposures to $CaO+K_2SO_4$ mixtures. The strong K and S signals in EDS mapping after the 1 hour exposure showed that the wetting of the small cracks by liquid K_2SO_4 occurred quickly. The occurrence of Ca at the same time shows that some CaO is also transported into the YSZ immediately. The $CaZrO_3$ layer was not observed on the YSZ surface at this short time, but a product was observed in some of the very small cracks inside the YSZ. This could indicate that the deposit at the surface of the YSZ was initially depleted of CaO as it was transported into the cracks. After longer times, more CaO from the deposit would reach the surface in great enough concentration that $CaZrO_3$ would form both externally and internally to the YSZ.

The solubility of CaO in liquid K_2SO_4 reported in the literature is approximately 1-2 wt. % [65]. This low solubility was confirmed by laboratory experiments, and indicates that liquid K_2SO_4 should not dissolve enough CaO at one time to form the amount of $CaZrO_3$ found in the 70 hour reaction. This suggests that the extensive $CaZrO_3$ formation observed in the longer exposures was the result of a continuous transport of CaO through the liquid K_2SO_4 during exposure. The reaction with $0.10CaO\text{-}0.90K_2SO_4$ (wt. %) shown in Figure 20 supports this conclusion. Both $CaO+K_2SO_4$ deposits (10 % CaO and 50 % CaO) should be capable of saturating the liquid K_2SO_4 with CaO. If the $CaZrO_3$ infiltration was caused by a single wetting of the YSZ by liquid K_2SO_4, then both exposures would produce the same infiltration.

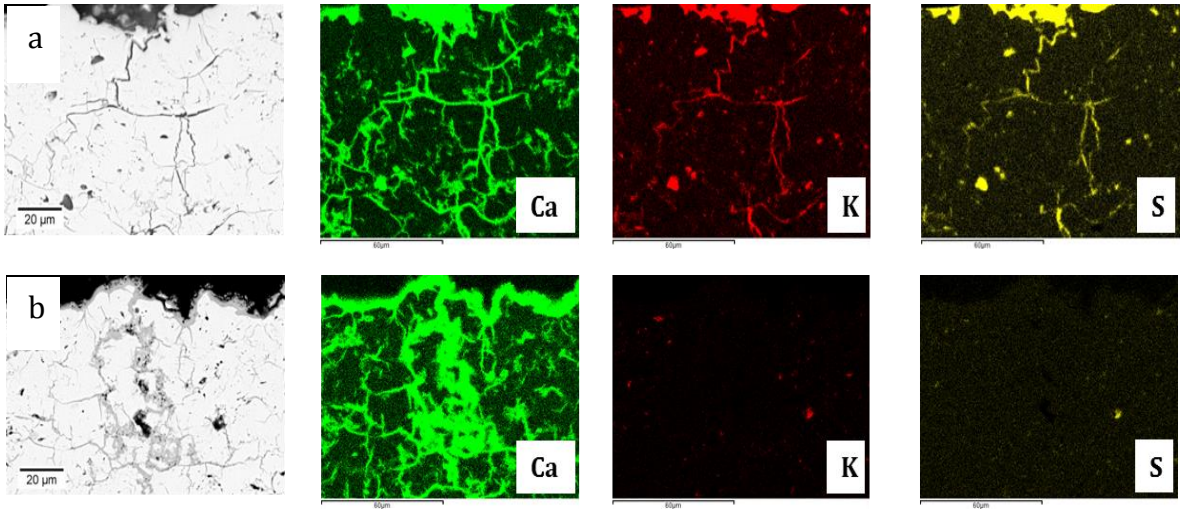

Figure 19: Deposit consisting of 0.5 $CaO\text{-}0.5\ K_2SO_4$ (wt. %) reacted with DVC YSZ in dry air

at 1100°C for (a) 1 hour and (b) 70 hours.

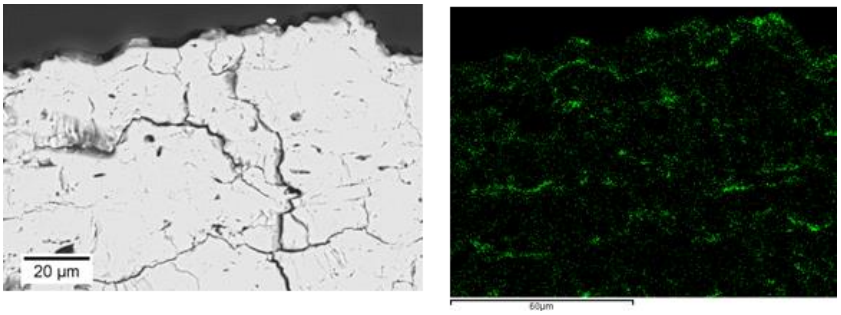

Figure 20: Deposit consisting of 0.10 CaO-0.90 K_2SO_4 (wt. %) reacted with DVC YSZ in dry air at 1100°C for 70h.

3.1.4 Cyclic Failure of Complete TBC Systems

The consequences of the $CaZrO_3$ infiltration on TBC lifetime were studied with complete TBC systems. The high-CaO synthetic ash with additions of FeS and K_2SO_4, described in Table 5 was deposited on a DVC TBC and cycled in lab air using the bottom-loading cyclic furnace described in section 2. An identical TBC was cycled with the same deposit without FeS or K_2SO_4 (i.e., only oxides). Both deposits contained a high enough level of CaO to react and form $CaZrO_3$ with the YSZ, but only the deposit containing K_2SO_4 would be expected to cause substantial infiltration. Based on comparison to previous work, the TBC should have endured at least 1000 cycles before failure without a deposit [58]. The deposit with K_2SO_4 caused TBC failure after 140 cycles, while the exposure without K_2SO_4 remained intact. Both TBCs are shown in Figure 21. Delamination in the failed TBC occurred along the crests of the undulated interface between the bond coat and the YSZ. Cracks were observed to pass through the TGO along the tops of the undulations. This is a typical failure mode for these TBCs [58], with the difference here being that it occurred substantially early in the ash with K_2SO_4. This demonstrates the damaging effect of the $CaZrO_3$ infiltration on the TBC lifetime.

Table 5: High-CaO synthetic ash with addition of K_2SO_4 and FeS

	CaO	SiO_2	Al_2O_3	Fe_2O_3	MgO	K_2SO_4	FeS
Wt%	63	16.2	8.1	1.8	0.9	5	5

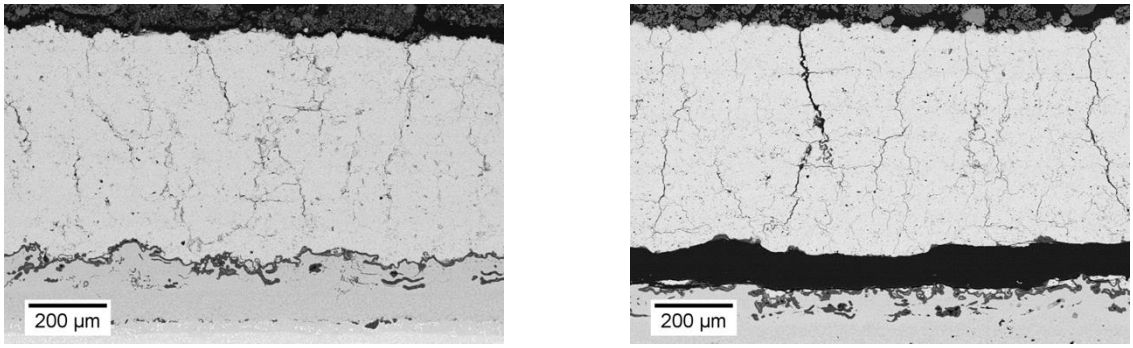

Figure 21: Complete DVC TBC exposed to 140 cycles in lab air with (a) high-CaO deposit and (b) the same deposit with additions of K_2SO_4 and FeS.

Additional cyclic testing was done to further show the effect of the high-CaO synthetic ash with K_2SO_4. The ash described in Table 5 was deposited on DVC TBCs which were then thermally cycled in dry air using the horizontal tube cyclic furnace described in section 2. Failure occurred later in this furnace (400-500 cycles) compared to the harsher thermal cycling provided by the bottom loading furnace. The location of TBC failure along the TGO/bond coat interface was the same in the two furnaces (Figure 21b and Figure 23a). TBCs were cycled to failure without deposit in the horizontal tube furnace in order to obtain a baseline comparison with deposit-induced failure. The early failure summarized in Figure 22 shows that the infiltration caused by the synthetic fly-ash resulted in severely limited TBC lifetimes. The TBC failure without (Figure 23b) was the same as the deposit-induced failure (except that it occurred after many more cycles). In both cases, delamination occurred at the TGO and resulted from cracks that extended across the crests of the undulations. The fly-ash resulted in an overall decrease in the compliance of the top coat that caused early failure that otherwise appeared normal.

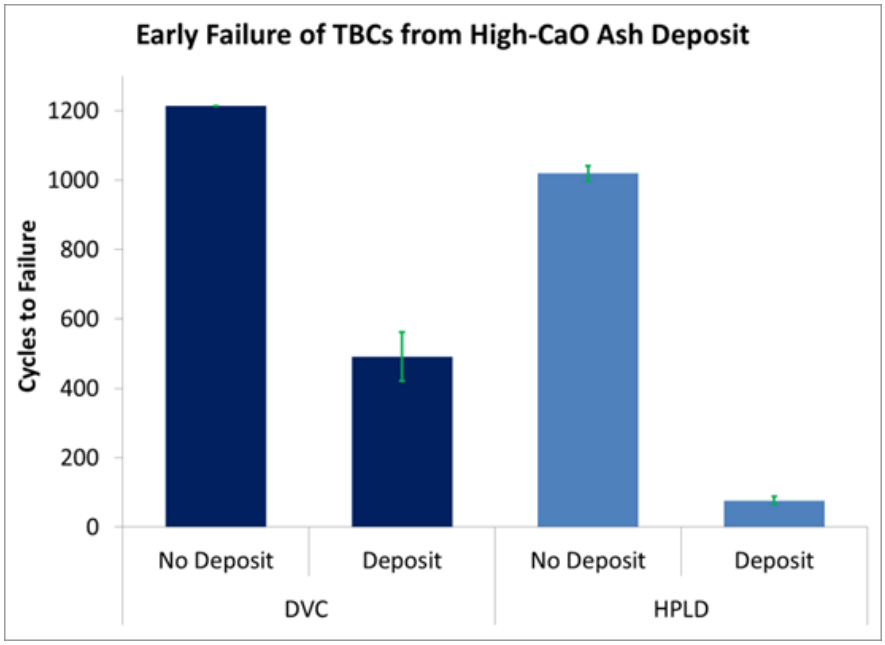

Figure 22: Thermal cycles to failure in dry air for DVC and HPLD TBCs exposed to high-CaO

synthetic fly-ash.

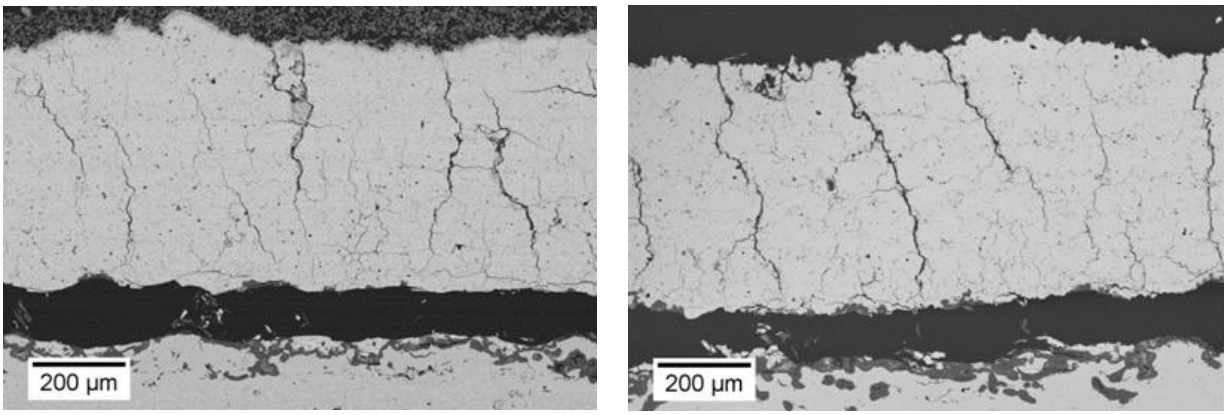

Figure 23: Complete DVC TBC that failed in dry air after exposure to (a) 444 cycles at 1100°C with high-CaO synthetic ash that included additions of K_2SO_4 and FeS, and (b) 1214 cycles at 1100°C with no deposit.

Early failure in TBCs cycled with ash deposit was a consequence of the $CaZrO_3$ infiltration. The dense reaction product, which filled cracks and pores in the YSZ, changed the mechanical properties of the coating and caused excess stress in the YSZ. The in-plane stress caused by a mismatch in the coefficient of thermal expansion (CTE) between a thin film and underlying substrate applied to the YSZ is described by equation 1.

$$\sigma = E_{tbc}\frac{\Delta\alpha\Delta T}{1-\nu} \qquad \text{Equation 2}$$

where σ is the stress in the film, E_{tbc} is the elastic modulus of the top coat, υ is Poisson's ratio, Δα is the difference in CTE between the layers, and ΔT is the temperature drop experienced in thermal cycling. This stress contributes to initial cracking that can lead to spallation during exposure to thermal cycling.

Important factors which influence the CTE mismatch stress are E, α, and ΔT. The TBCs which were cycled to failure experienced the same ΔT with deposit and without. Therefore, changes in E and/or α can be used to at least qualitatively show a change in overall stress in the top coat. The value of α is smaller than the metallic substrate, so an overall decrease in α would further increase overall stress (by further increasing Δα). Similarly, an overall increase in E of the top coat would also increase overall stress in the TBC. The change in average value of E as a result of $CaZrO_3$ infiltration was measured for free-standing DVC YSZ samples. Samples that were heat treated at 1100°C in dry air for 72 hours were measured to have an elastic modulus of 30 ± 3 GPa, and samples that were reacted with a high-CaO ash (containing 10wt% K_2SO_4) in the same conditions were measured to have a modulus of 132 ± 19 GPa. This dramatic increase in E caused by $CaZrO_3$ infiltration reduced the overall strain tolerance and increased the CTE mismatch stress significantly.

The effects of the high-CaO synthetic ash on the more porous HPLD top coat were more severe than with the DVC top coat TBCs. The cyclic failure is compared in Figure 22 for the two types of TBCs. HPLD TBCs were severely damaged in less than 100 cycles. It is

important to note that without deposit these TBCs exhibited lifetimes (and location of failure) comparable to the DVC TBCs. Failure of HPLD TBCs is shown in Figure 24. Cyclic exposure without deposit caused delamination of the intact YSZ top coat that separated from the substrate at the YSZ/bond coat interface. The deposit, however, caused $CaZrO_3$ infiltration which triggered significant cracking and spallation throughout the YSZ and eventual delamination of the entire top coat (or what was left of it). Figure 24b shows significant crack propagation though the middle of the YSZ top coat. This was very distinct from a normal failure near the TGO.

The accelerated failure of the HPLD top coats can be explained in several ways. These top coats are more porous than the DVC coatings. The regions that are infiltrated by $CaZrO_3$ will have increased values of E, and greater infiltration should lead to greater changes in overall values of E. This of course will equate to a higher stress. Also, these HPLD coatings exhibit the conventional "splat" morphology that does not exist in the DVC coatings. These horizontal splat boundaries exhibit lower toughness and allow for easier crack propagation. Therefore, the increased stress from $CaZrO_3$ infiltration can cause crack initiation and then cracks can spread quite easily along the splat boundaries, leading to spallation of large regions of YSZ.

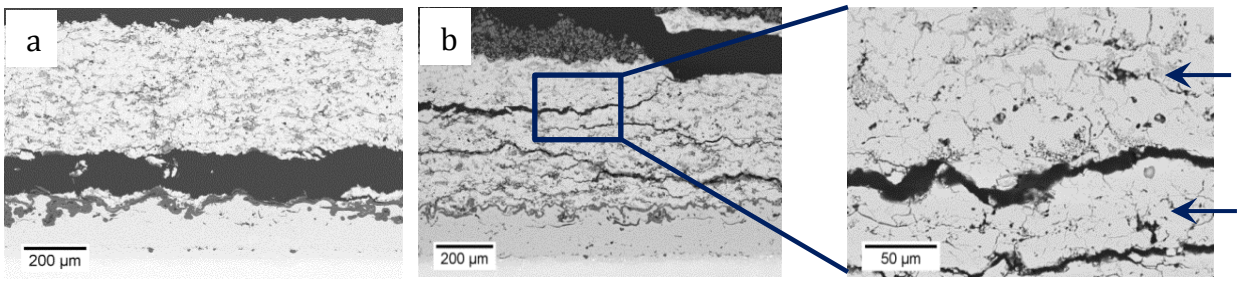

Figure 24: (a) Failed HPLD TBC without deposit and (b) Damaged HPLD TBC due to high-CaO synthetic ash.

3.1.5 Degradation from High-SiO_2 Ash

The damage caused by high-CaO ash in HPLD TBCs resulted in severely shortened lifetimes. This high level of CaO may not always exist in real fly-ash, however, because fly-ash compositions vary with fuel type and geography. IGCC fly-ash often contains high levels of SiO_2. The high-SiO_2 ash described in

Table 6 was reacted with free-standing DVC YSZ and also with complete HPLD TBC systems. Figure 25 shows that some infiltration was found in cracks in the TBC after exposure to this ash for 72 hours in dry air at 1100°C. EDS analysis show that K and S remain in the infiltrated region after long (72 hour) exposures, which shows that the infiltrating product contains K and S. This infiltration is different than the $CaZrO_3$ infiltration, mainly in that it does not appear to react with the YSZ to form any Zr or Y

containing product (and therefore it would not be expected to consume YSZ). The infiltration from the high-SiO_2 ash is a potassium silicate formed between the SiO_2 and K_2SO_4 in the synthetic ash that forms a liquid at 1100°C. This is different than the $CaZrO_3$ infiltration where liquid K_2SO_4 transports the CaO but K is no longer in the YSZ after 72hours (most likely due to evaporation).

Early failure of HPLD TBCs from cycling with the high-SiO_2 synthetic ash in dry air is summarized in Figure 26. Figure 27 shows an infiltrated region of YSZ near the top of the TBC (indicated by the arrow) and cracking along the splat boundaries directly below. This caused regions of YSZ to break away in a similar manner as was observed with $CaZrO_3$ infiltration. Eventually failure occurred when the remaining top coat delaminated entirely along the TGO.

This spallation in the top coat was more severe with the high-CaO ash compared to high-SiO_2 ash. The $CaZrO_3$ reaction was observed deeper into the YSZ, which caused larger regions to break away in comparison to the potassium silicate infiltration. This could be the result of a higher viscosity of liquid potassium silicate that would lead to less infiltration. The more shallow infiltration of the potassium silicate caused smaller regions of YSZ loss. This could also indicate that $CaZrO_3$ infiltration had a greater effect on altering of mechanical properties (E, CTE) of the top coat which caused more spallation.

When infiltrated regions of YSZ spall from the top coat, one would expect the stress caused by a dense infiltration of ash to be relieved. This could slow down further damage of the TBC, although the top coat would now be thinner and not able to provide as much a thermal barrier. Infiltration in the newly exposed region is minimal, and further spallation of TBC is halted until complete delamination occurs. An additional cyclic test was conducted in which the ash was re-applied every 20 cycles in order to facilitate newly infiltrated regions of YSZ where spallation had occurred. The results shown in Figure 26 indicate that the additional damage to the TBC is not extensive. This result suggests that the initial stress induced by the first infiltration (before spallation of infiltrated region) was responsible for much of the overall damage to the TBC. The re-application of ash caused more regions of YSZ near the surface to spall from the TBC, but the eventual delamination of the entire top coat did not occur significantly sooner with the re-application.

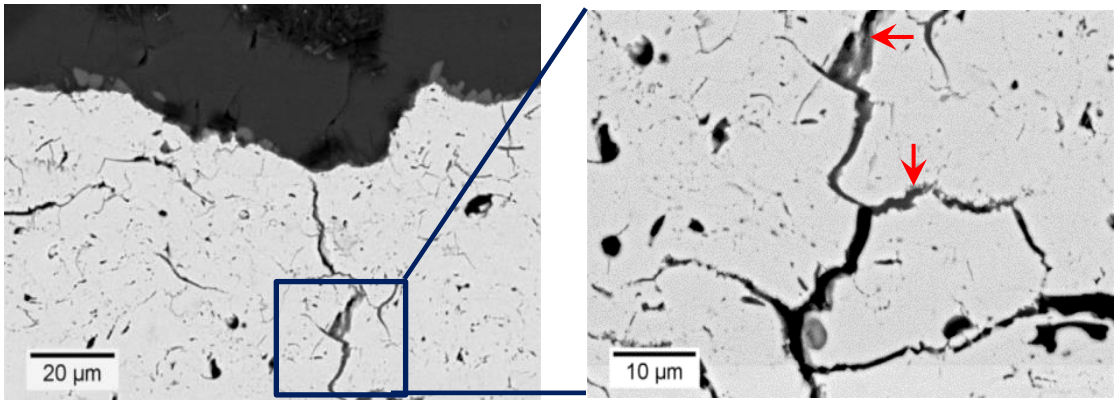

Figure 25: DVC TBC that has been exposed to a high-SiO_2 ash in dry air at 1100°C for 72 hours showing some infiltration of ash constituents in small cracks near the surface.

Table 6: High-SiO_2 synthetic ash composition with addition of K_2SO_4

	SiO_2	Al_2O_3	CaO	Fe_2O_3	MgO	K_2SO_4
Wt%	45	22.5	9	9	4.5	10

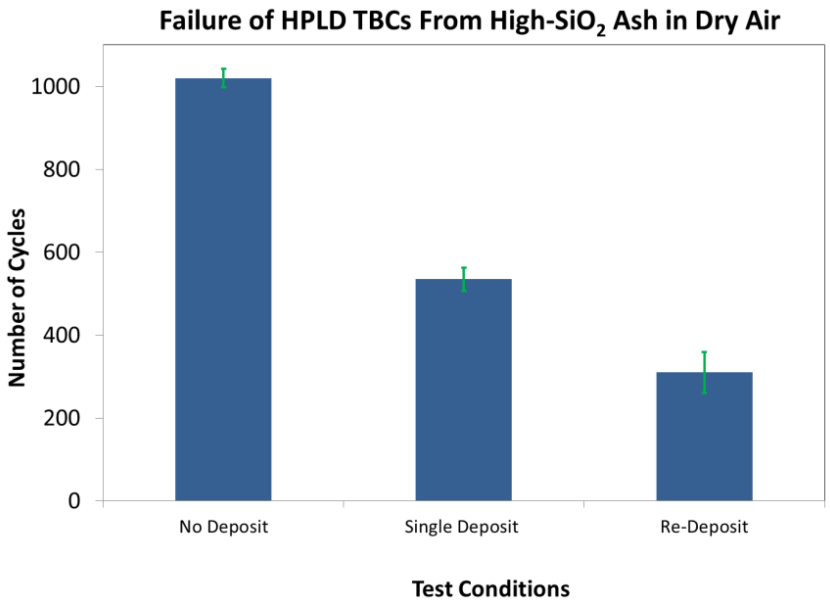

Figure 26: Thermal cycles to failure for HPLD TBCs with high-SiO_2 ash in dry air.

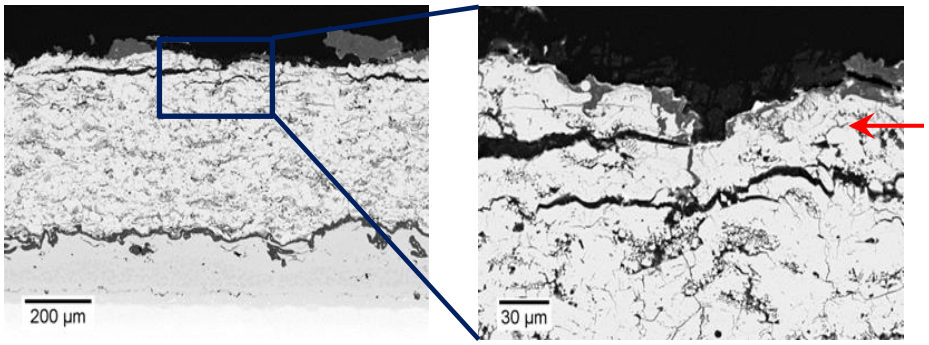

Figure 27: Damaged HPLD TBC from cyclic thermal exposure to high-SiO_2 ash with K_2SO_4 showing infiltrated regions of YSZ breaking away from top coat.

TBCs used in combustion turbines are exposed to gas atmospheres that contain CO_2, SO_2, and H_2O. The degradation of HPLD TBCs from high-SiO_2 ash (re-deposited every 20 cycles) was tested in more harsh gas atmospheres that better simulate real operating environments. The results are summarized in Figure 28. The overall damage to the TBC was nearly the same in dry air as in the steam-containing atmosphere. This result shows that

when TBCs are at low temperatures in thermal cycling, they are not significantly affected by low-temperature degradation (LTD) that has been observed in 7YSZ TBCs in laboratory experiments [41]. This could be related to the fact that LTD is known to start at the YSZ surface and progress inward. The deposit at the surface in this case may be inhibiting the LTD process from initiating at the surface.

HPLD TBCs with SiO_2 ash were cycled to failure in an atmosphere of 1000ppm SO_2-2%O_2-bal CO_2. Thermal cycles to failure are shown in Figure 28 compared to the dry air and steam-containing atmospheres. The addition of SO_2 into the atmosphere resulted in earlier failure of the TBCs. Damage in the top coat was observed to be similar to dry air experiments. However, the bond coat oxidation was also affected in the SO_2-containing atmosphere. The oxidation at the crests of the undulated interface was disrupted, as seen in Figure 29. Significant internal TGO growth through these regions would be accompanied by a volume expansion that contributed to additional stresses. Top coat delamination, which typically occurs along the crests, would occur more easily with this additional stress. The brittle internally growing alumina would also facilitate cracking through the bond coat, as shown by the arrow in Figure 29 and enable further delamination.

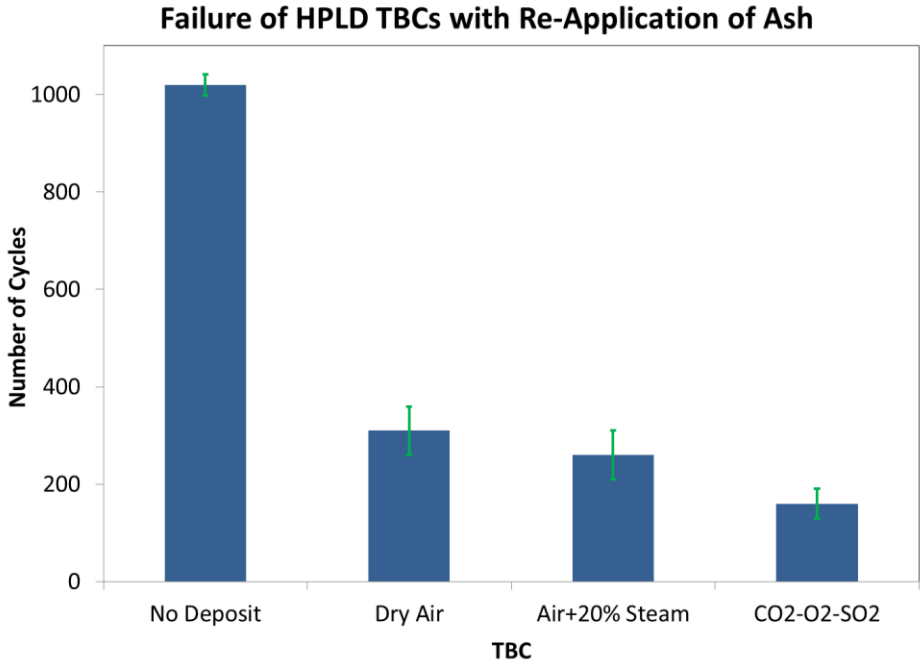

Figure 28: Thermal cycles to failure for HPLD TBCs with high-SiO_2 ash in several gas atmospheres where the deposit was re-applied every 20 cycles in each case

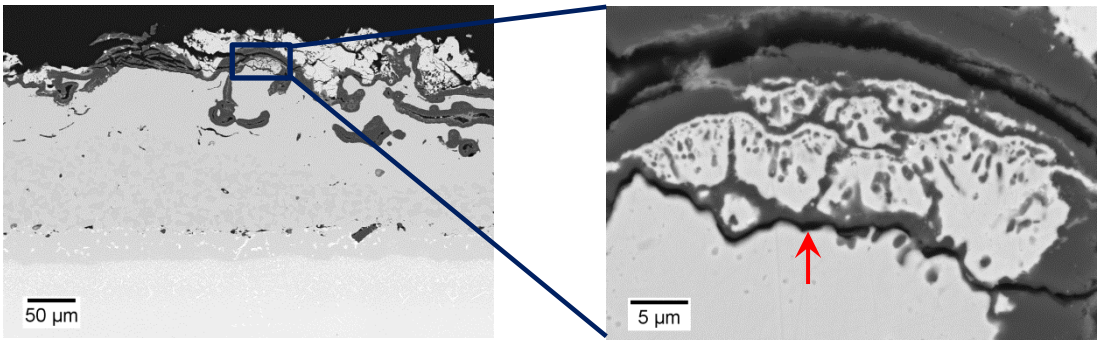

Figure 29: Failed HPLD TBC after 220 cycles at 1100°C in gas atmosphere of 1000ppm SO_2-2%O_2-CO_2 with high-SiO_2 synthetic ash.

3.2 Bond Coat

3.2.1 Oxidation in the absence of a deposit

Experiments carried out in the absence of a deposit establish an understanding of the intrinsic oxidation behavior of the NiCoCrAlY alloys. Weight gains recorded after 50 h exposure to various gas mixtures at 1100 °C are summarized in Figure 30. All alloys yielded relatively low weight gains; experimental variability does not allow any significant effect of gas or alloy composition to be identified solely from the weight gains. Compact and adherent Al_2O_3 scales were formed in all gases, as exemplified with two γ-rich alloys in Figure 31. Careful examination of the reacted specimens shows that scales were slightly thinner after reaction in CO_2-H_2O, compared to dry air (Figure 32). Furthermore, in dry air, alloys with the higher aluminum content also produced slightly thinner scales than alloys with less aluminum. Calculation of instantaneous oxidation rates from data obtained by thermogravimetric analysis (TGA, not shown here) indicated that the variance between low and high Al alloys mostly occurs in the transient stage of the exposure, although a slightly higher oxidation rate was found to persist for up to 15 h for the low-Al alloys. This difference in oxidation rate is related to the fraction of β in these two-phase alloys. In the β-rich alloys, the β dissolution zone is quite shallow, and the oxide grown on regions where β was present prior to exposure is seen to be thinner than that formed on preexisting γ regions (Figure 33).

As noted in Section 2, the low solubility of Y in β causes yttride precipitation in β-rich alloys. Reaction of the yttrides located near the surface with oxygen produces “pegs” of very stable yttrium-aluminum oxides that extend into the alloy. Both versions of the β-rich alloy Ni-19Co-15Cr-24Al-zY formed pegs, but these were present in larger number and size in the higher Y version, as shown in Figure 33. This apparently had no detrimental effect in these deposit-free, short isothermal exposures. It is noteworthy, however, that the larger pegs contained some Cr, Ni and Co oxide at their surface. This possibly occurred because these constituents of the yttrides could not diffuse out during the rapid oxidation process taking place in early stages of the exposure.

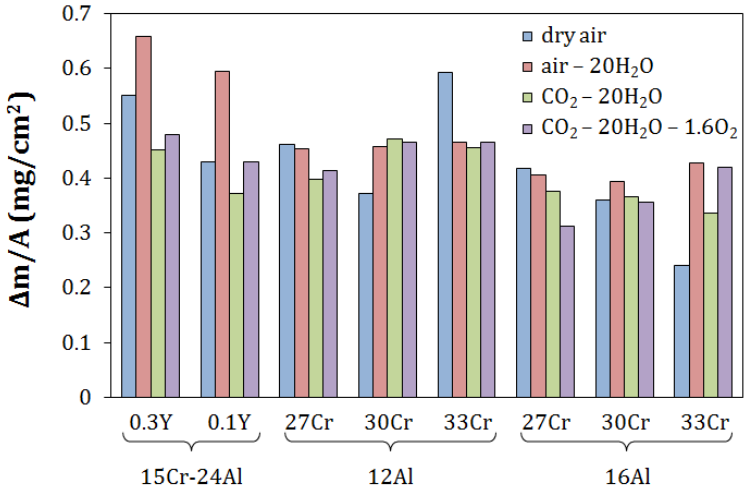

Figure 30: Weight changes recorded after 50 h exposure of the NiCoCrAlY alloys in various gas atmospheres at 1100 °C, in the absence of a deposit.

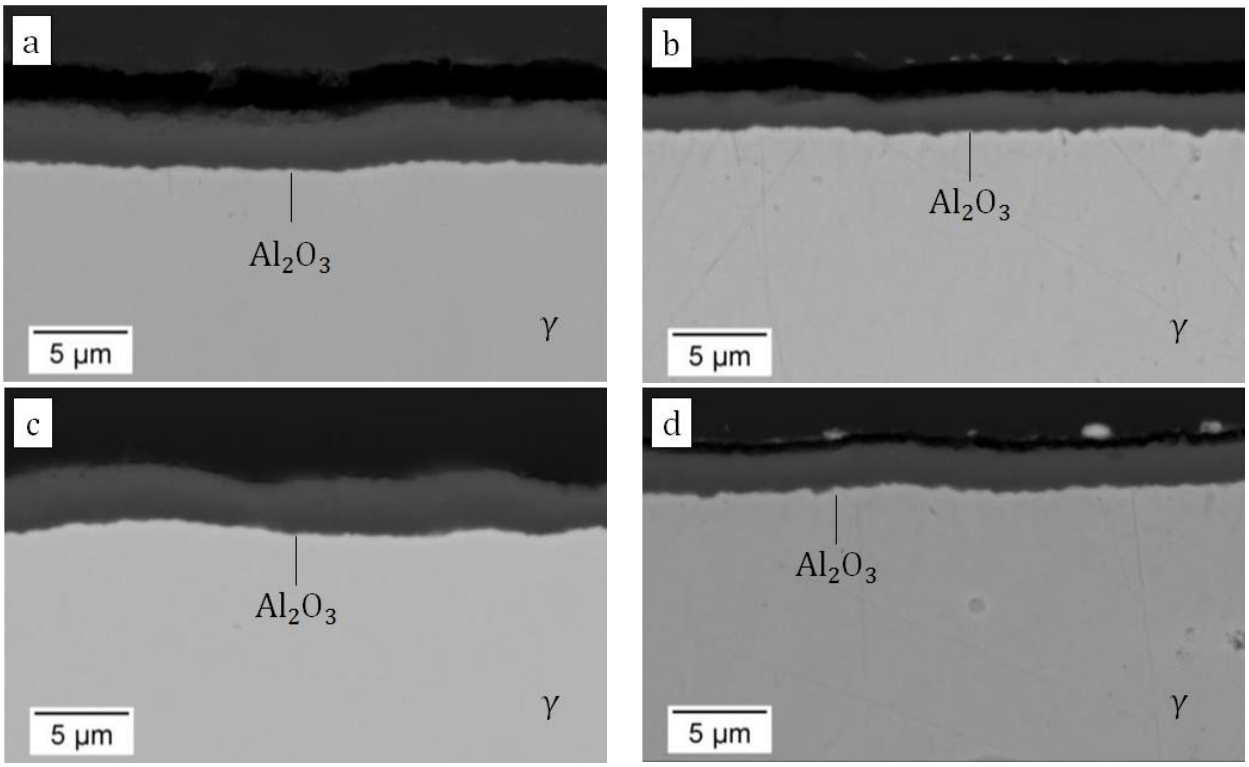

Figure 31: Typical reaction morphology observed after 50 h exposure of γ-rich NiCoCrAlY alloys in (a,c) dry air and (b,d) CO_2-H_2O at 1100 °C, in the absence of a deposit. (a,b) Ni-30Co-27Cr-12Al-0.1Y; (c,d) Ni-30Co-33Cr-12Al-0.1Y.

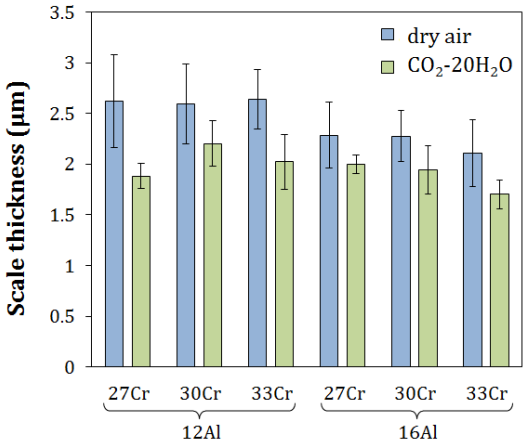

Figure 32: Average scale thickness measured after 50 h oxidation of the NiCoCrAlY alloys with no deposit at 1100 °C.

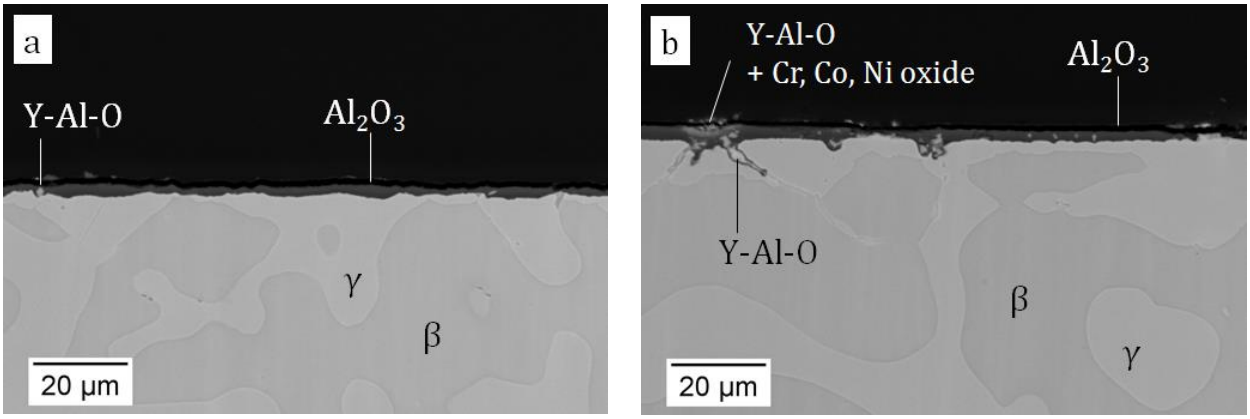

Figure 33: Reaction morphology observed after 50 h exposure of the β-rich Ni-19Co-15Cr-24Al-zY alloys with (a) 0.1 Y and (b) 0.3 Y in dry air with no deposit at 1100 °C.

3.2.2 Corrosion by class-C ash at 1100 °C

As will be discussed in Section 3.2.4, corrosion experiments using a variety of fly-ash deposit compositions showed that significant degradation of the alloys of interest only occurred with CaO-rich, sulfate-containing mixtures such as class C ash. The reaction of the γ-rich Ni-30Co-27Cr-12Al-0.1Y with class C ash in CO_2-H_2O at 1100 °C is presented first to introduce the degradation morphology typically observed in the present study. The effect of alloy composition will then be discussed. It is noted that exposure to fly ash generally produced non-uniform extents of reaction, where regions of the alloys were effectively protected by a thin Al_2O_3 scale, while other regions, depending on the conditions considered, underwent significant degradation. Micrographs shown in the present and

following sections attempt to be representative of the reaction morphology observed on average in corroded regions of a given sample.

3.2.2.1 Reaction mechanism and effect of gas composition

Aside from the regions of exclusive Al_2O_3 growth, two reaction morphologies were identified after exposure of Ni-30Co-27Cr-12Al-0.1Y to class C ash in CO_2-H_2O at 1100 °C. The most prevalent is depicted in Figure 34a, where nodules of mixed oxides are seen to extend to variable widths and depths. Those nodules contained both alloy (Al, Cr, Co, Ni) and ash (Al, Ca, Fe, Mg, Na, Si) constituents, and had variable compositions. A continuous Al_2O_3 layer was always found at the base of the nodules, and was identified by photo-stimulated luminescent spectroscopy (PSLS, not shown here) to be α-Al_2O_3. In less frequent locations (Figure 34b), the nodules comprised a mixture of Al-free metal and Al-rich and Cr-rich oxide, surmounted by a mixed oxide layer and separated from the bulk alloy by a continuous Al_2O_3 layer. The outermost oxide layer was Al-rich but also contained ash constituents.

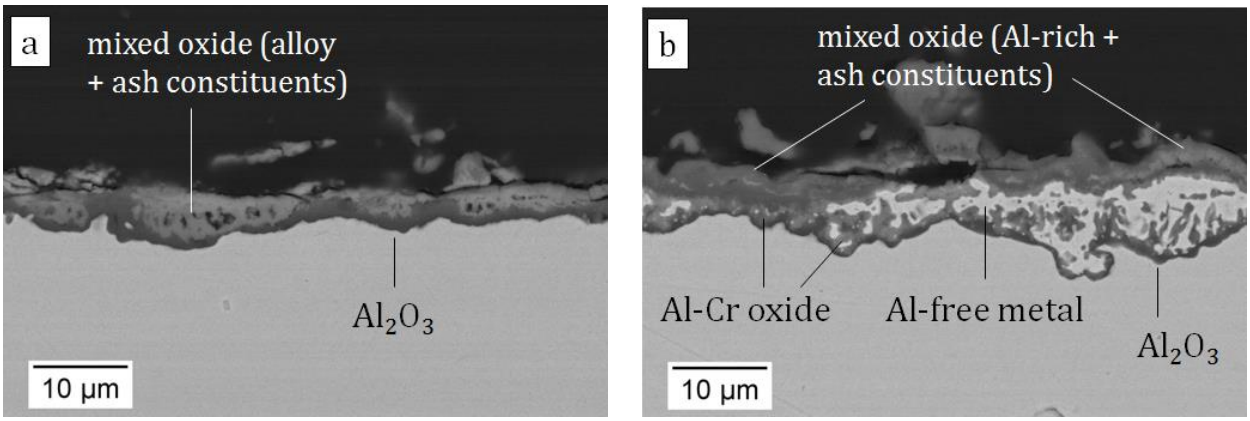

Figure 34: Reaction morphology observed after 50 h exposure of γ-rich Ni-30Co-27Cr-12Al-0.1Y alloys to synthetic class-C fly ash in CO_2-H_2O at 1100 °C. (a) and (b) represent the two typical degradation morphologies observed on the same specimen.

Mechanistic aspects of this corrosion process were studied by means of time-lapse experiments. After 1 h reaction in CO_2-H_2O (Figure 35a), the alloy exhibited small Al_2O_3 protrusions, growing inward into the subscale. These developed from an Al-rich oxide layer located at the original metal surface, and continuous with the protective Al_2O_3 on the adjacent alloy surface. A Cr-rich oxide layer was found above the formerly protective scale. From these observations, it is concluded that an Al_2O_3 scale was initially formed and covered the entire alloy surface; reaction with the ash, however, locally consumed the oxide, and as its thickness decreased, the Al flux necessary to sustain its growth eventually exceeded the flux the alloy could provide. This process is discussed in more detail in Section 3.2.3 for the simplified case of reaction with pure CaO. Local failure to maintain external Al_2O_3 growth led to inward growth of Al_2O_3 protrusions, and as the external scale lost its protective character, it was outgrown by a Cr-rich oxide layer. Essentially the alloy, depleted of its aluminum but rich in chromium, turned into a Cr_2O_3-former. This allowed the oxygen activity at the metal surface to be maintained to a low level, such that the alloy could

repassivate: Al_2O_3 progressively extended across the bottom end of the protrusions until forming a new continuous, protective subsurface layer.

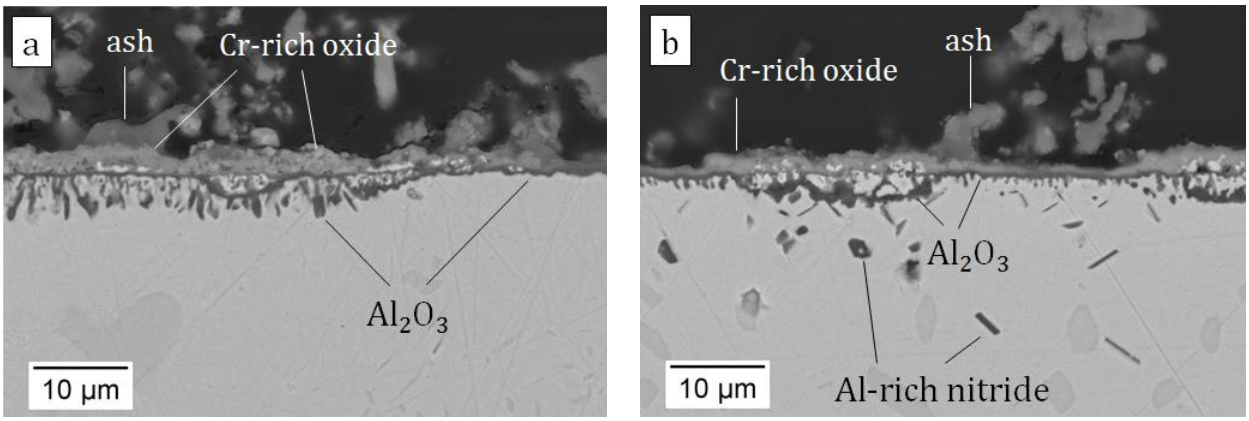

Figure 35: Reaction morphology observed after 1 h exposure of γ-rich Ni-30Co-27Cr-12Al-0.1Y in (a) CO_2-H_2O, and (b) dry air with synthetic class-C fly ash at 1100 °C.

Similar cases of external Cr_2O_3 and internal Al_2O_3 protrusions have been reported by previous investigators for marginal Al_2O_3-forming alloys (i.e. containing ~ 4-6 at. % Al) oxidized in the absence of a deposit [66, 67, 68, 69, 70, 71]. Depending on the specific alloy composition, the steady-state eventually reached ranges from fast internal oxidation to continuous Al_2O_3 growth, as in the present case. The Ni-30Co-27Cr-12Al-0.1Y alloy has relatively high Al and Cr contents, and is a good Al_2O_3-former in the absence of fly ash (Figure 31). This explains why repassivation readily occurs, so long as the ash responsible for the initial protective scale disruption is not in contact with the newly-formed Al_2O_3.

The morphology observed after 50 h reaction in Figure 34b follows directly from the proposed mechanism of disruption-repassivation. In the regions typified by Figure 34a, the absence of an external Cr-rich oxide layer allowed the Al-free metal to be fully oxidized and the ash constituents to be incorporated into this mixed oxide. It is noted that an oxide layer providing some degree of protection was likely present at some point in order for an Al_2O_3 sublayer to form at the base of the nodule. All reaction products observed showed traces of mechanical damage such as cracks or delamination, due to CTE mismatch and associated thermal stresses during cooling, but also possibly related to the sintering of the ash with the thermally-growing oxides at temperature.

One-hour exposures were carried out in different gases using the same alloy (i.e., Ni-30Co-27Cr-12Al-0.1Y) and deposit to ascertain the effect of CO_2, H_2O and the gas p_{O_2} on the early stages of the corrosion process. The results obtained in CO_2-H_2O-O_2 ($p_{O_2} = 2 \times 10^{-2}$ atm, not shown) and dry air ($p_{O_2} = 2 \times 10^{-1}$ atm, Figure 35b) were identical to those obtained in CO_2-H_2O ($p_{O_2} = 4 \times 10^{-5}$ atm, Figure 35a), with the exception that internal aluminum nitrides formed in the N_2-bearing gas. The nitrides were present as a relatively small volume fraction, and distributed in a non-uniform, apparently random manner; it is therefore difficult to assess their role in the reaction process. However, the fact that the degradation morphologies were the same with and without nitrogen suggests that the nitrides were a consequence, rather than a cause of the disruption of the initial Al_2O_3 scale. Furthermore, the average thickness of the corrosion product was not found to significantly

increase between 50 h and 250 h reaction in dry air (Figure 36). This indicates that nitridation was not an obstacle to repassivation, and that the establishment of a continuous Al_2O_3 sublayer effectively protected the alloy in these isothermal conditions. Based on this series of results, it is concluded that the presence of CO_2 or H_2O is not specifically required for the initial Al_2O_3 scale to fail in the presence of class C ash, not more than it prevents its establishment or its continued growth in the absence of a deposit (see Section 3.2.1). This was expected insofar as the mechanism responsible for Al_2O_3 failure involves reaction of the thermally-grown oxide with constituents of the ash, which the presence of CO_2 or H_2O or the p_{O_2} are not thought to affect. It is also noted that although it had no major consequence here, testing in air (or any N_2-bearing mixture) is not recommended, as nitridation is an unnecessary complication.

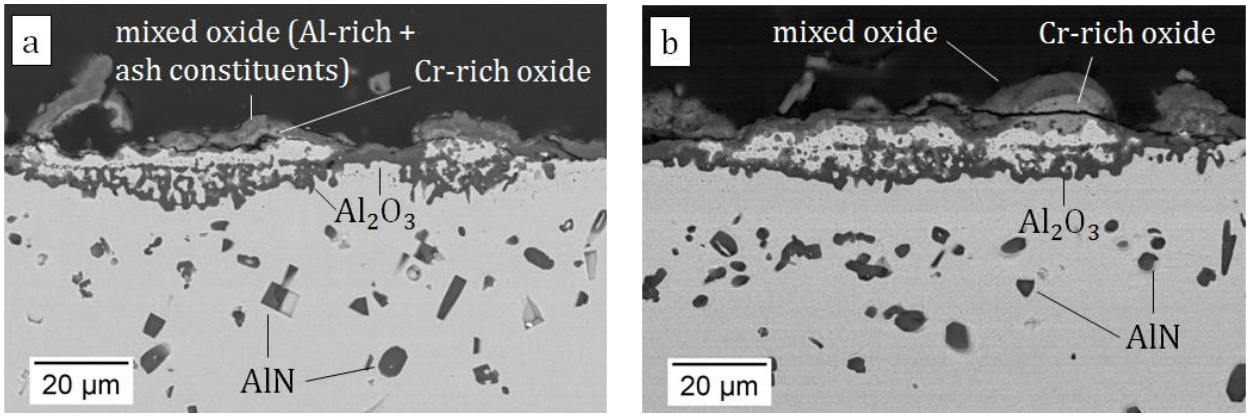

Figure 36: Reaction morphology observed after (a) 50 h and (b) 250 h exposure of γ-rich Ni-30Co-27Cr-12Al-0.1Y in dry air with synthetic class-C fly ash at 1100 °C.

3.2.2.2 Role of alloy composition on reaction with class C ash

Figure 37 shows typical reaction morphologies obtained after 50 h exposure of the six model NiCoCrAlY alloys to commercial class-C ash in CO_2-H_2O at 1100 °C. Increasing the aluminum content proved beneficial, as the average depth of metal loss before repassivation was lower for the 16Al alloys. Qualitatively, the 16Al alloys also exhibited a greater proportion of regions where the initially-formed Al_2O_3 was never disrupted. In contrast, higher chromium contents led to slightly deeper corrosion (except for Ni-30Co-33Cr-16Al-0.1Y, where the absence of any significant degradation may have been due to a lack of contact with the deposit during the exposure).

Because NiCoCrAl is a quaternary system, tie-lines of the β-γ field are not located on a plane of constant Co content such as that shown in Figure 6. Nevertheless, a comparison of various isopleths (not shown here) indicated that β and γ compositions did not vary much with Co content, at least within the range of interest. The isopleth in Figure 6 can therefore, to a first approximation, be used to understand how varying Al and Cr concentrations affect phase compositions and fractions. Values measured experimentally after a 1100 °C heat treatment are shown in Table 1. Qualitatively, increasing either the alloy aluminum or chromium content has the same effect, which is to have less Al and more Cr in γ, and a roughly unchanged level of Al and more Cr in β. Both also lead to a larger fraction of β,

although in this regard going from 12 to 16 at. % Al has a more marked effect than going from 27 to 33 at. % Cr.

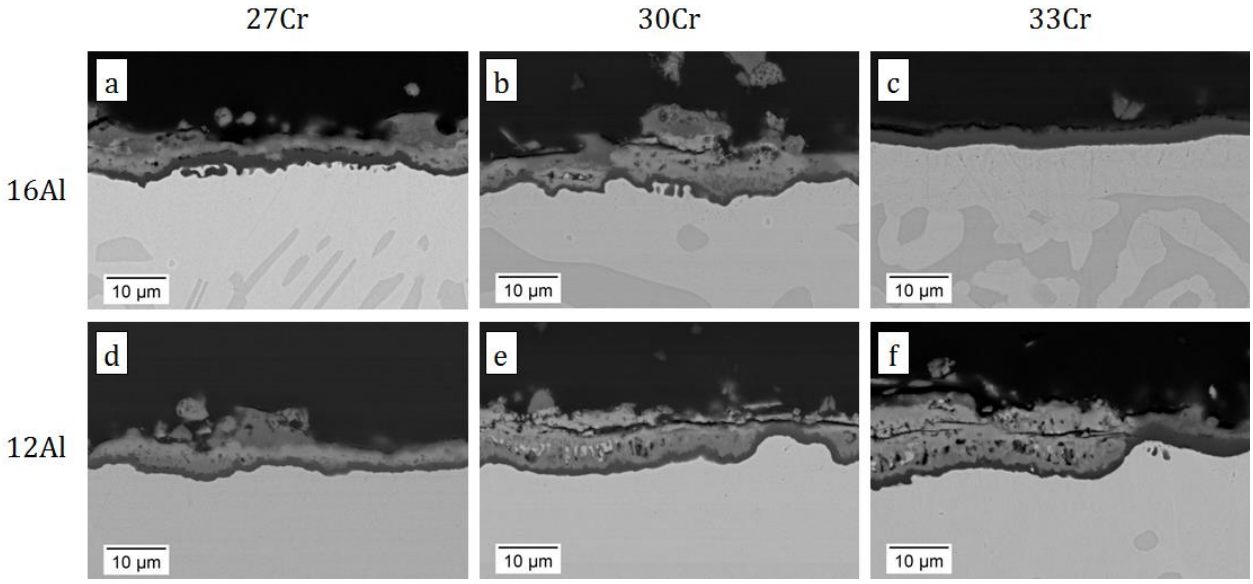

Figure 37: Reaction morphology observed after 50 h exposure of the γ-rich Ni-30Co-xCr-yAl-0.1Y alloys in CO_2-H_2O with commercial class-C fly ash at 1100 °C. (a) 27Cr-16Al; (b) 30Cr-16Al; (c) 33Cr-16Al; (d) 27Cr-12Al; (e) 30Cr-12Al; (d) 33Cr-12Al.

According to the proposed reaction mechanism, what is critical to corrosion resistance in the presence of class C ash is the ability for the alloy (mostly of the γ phase, since β is rapidly depleted from the surface of these γ-rich alloys) to sustain a sufficient outward aluminum flux at the metal/oxide interface. In view of all these observations, the slightly deleterious effect of increasing the alloy chromium content is explained by the fact that it produces a lower Al γ phase, and consequently a lower outward Al flux. When increasing the alloy aluminum content, however, the beneficial effect of a larger β fraction overwhelms the deficiency of the γ phase, as β dissolution helps maintaining the Al flux in γ. It is concluded that to remain strictly an Al_2O_3-former and provide the best degree of protection in the presence of class C ash, an MCrAlY alloy should have rather high Al and limited Cr (i.e., high β fraction); however, sufficient chromium is still desirable both to provide Cr_2O_3 scale protection after Al_2O_3 has been disrupted, and to help establish the Al_2O_3 scale in the first place.

A good compromise was achieved by the low Y version of the high β alloy, Ni-19Co-15Cr-24Al-0.1Y, since it showed no Al_2O_3 failure during the duration of the experiments (Figure 38a). In contrast, the higher Y version of this alloy suffered relatively severe corrosion (Figure 38b). The extent of reaction along the surface was not uniform, and regions of the same specimen were left mostly unattacked. In Figure 39, the peg on the right-hand side is located immediately below the original alloy surface and is seen not to disrupt the Al_2O_3 scale; whereas the left-hand side peg, which intersects the alloy surface, dissolved both alloy and ash elements, thereby creating a discontinuity in the Al_2O_3 scale. In this particular case, a continuous Al_2O_3 layer eventually formed around the peg, effectively stopping the attack, but it is believed that larger pegs where repassivation was not possible

are the cause for the severe degradation observed on this alloy. A similar, detrimental effect of "overdoping" was also identified in type II hot corrosion [72].

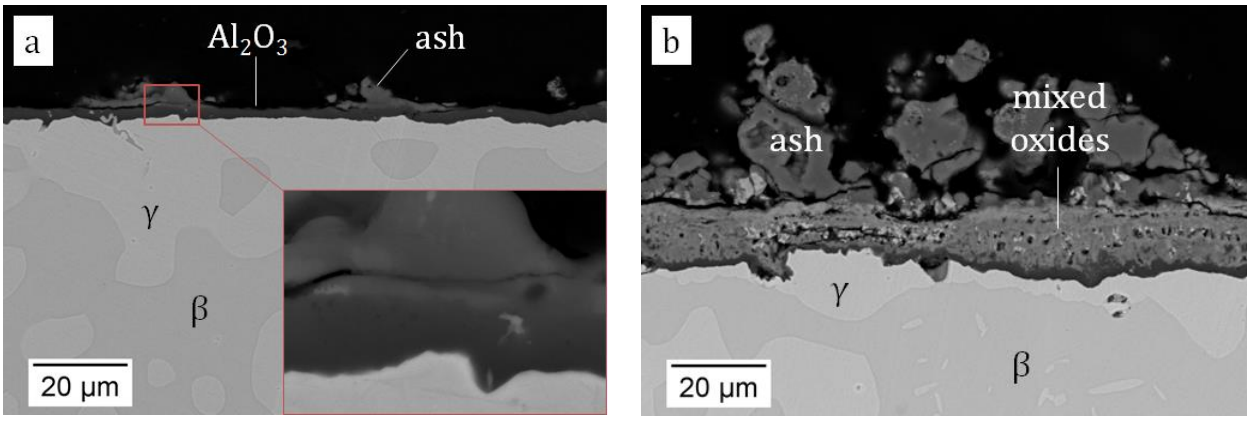

Figure 38: Reaction morphology observed after 50 h exposure of β-rich Ni-19Co-15Cr-24Al-zY with (a) 0.1 Y and (b) 0.3 Y in CO_2-H_2O with commercial class-C ash at 1100 °C.

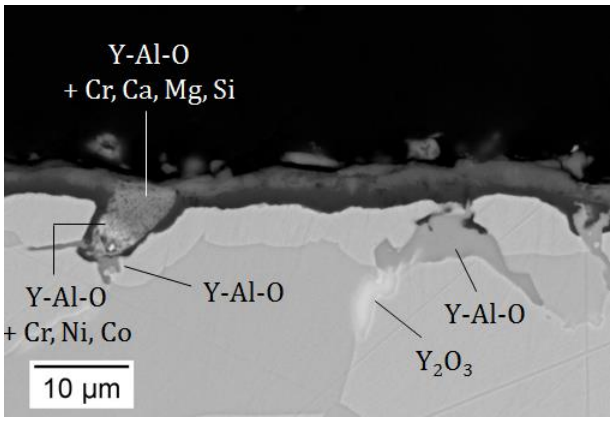

Figure 39: Micrograph showing two Y-Al-O pegs after 50 h exposure of high Y alloy Ni-19Co-15Cr-24Al-0.3Y to commercial class-C ash in CO_2-H_2O at 1100 °C.

3.2.3 Role of individual constituents: reaction with CaO

In order to investigate the role of the oxides and sulfates in the reactivity of fly ash, corrosion experiments were conducted using individual constituents and mixtures of increasing complexity. Among the individual oxides tested (CaO, MgO, Al_2O_3, SiO_2, Fe_2O_3), only the relatively basic CaO and MgO had a significant impact, as their reaction with the thermally-grown Al_2O_3 produced calcium and magnesium aluminates, respectively. The case of CaO is assessed in detail in the present section.

3.2.3.1 Nature of the corrosion process and influence of alloy composition

Exposure to pure CaO was carried out in dry air at 1100 °C using the alloys which showed the most and least resistance to class C ash: the β-rich Ni-19Co-15Cr-24Al-0.1Y (Figure 40a) and the γ-rich Ni-30Co-33Cr-12Al-0.1Y (Figure 40b), respectively. After 50 h, both alloys were found to develop several layers of calcium aluminates ($xCaO\text{-}yAl_2O_3$, noted C_xA_y). The layer sequence was Al-rich CA_2 nearest to the substrate, followed by equimolar CA, and occasionally the Ca-rich $C_{12}A_7$ and C_3A toward the CaO deposit. These were identified by matching compositions measured by SEM-EDS to the intermediate compounds known to exist in the $CaO\text{-}Al_2O_3$ system (Figure 41a). A thin and continuous Al-rich oxide layer, identified as $\alpha\text{-}Al_2O_3$ by PSLS, was always found between the alloy and the first aluminate layer. In addition, the γ-rich alloy produced a thick outer layer of calcium chromate, with (Ni,Co)O embedded throughout (Figure 40b). These were occasionally found in small amounts on the β-rich alloy.

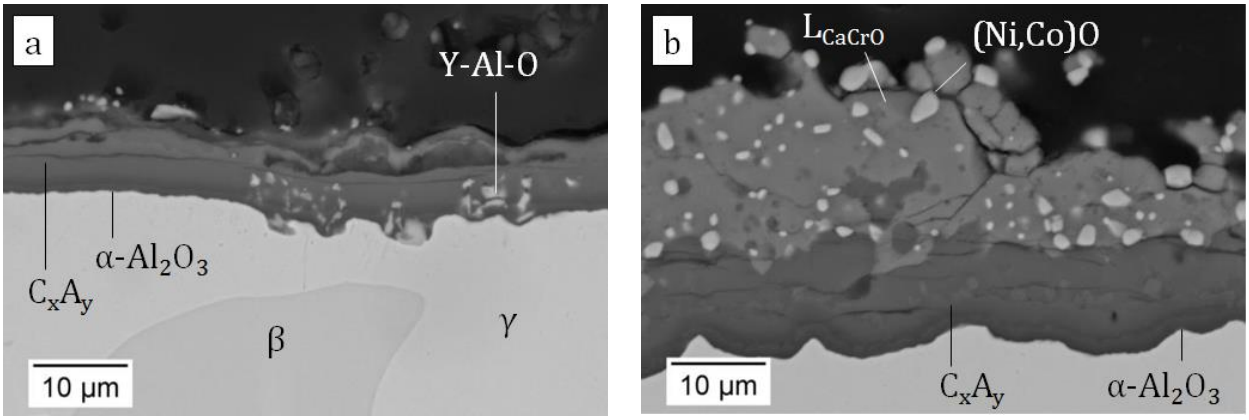

Figure 40: Reaction morphology observed after 50 h exposure of (a) Ni-19Co-15Cr-24Al-0.1Y and (b) Ni-30Co-33Cr-12Al-0.1Y in dry air with CaO at 1100 °C.

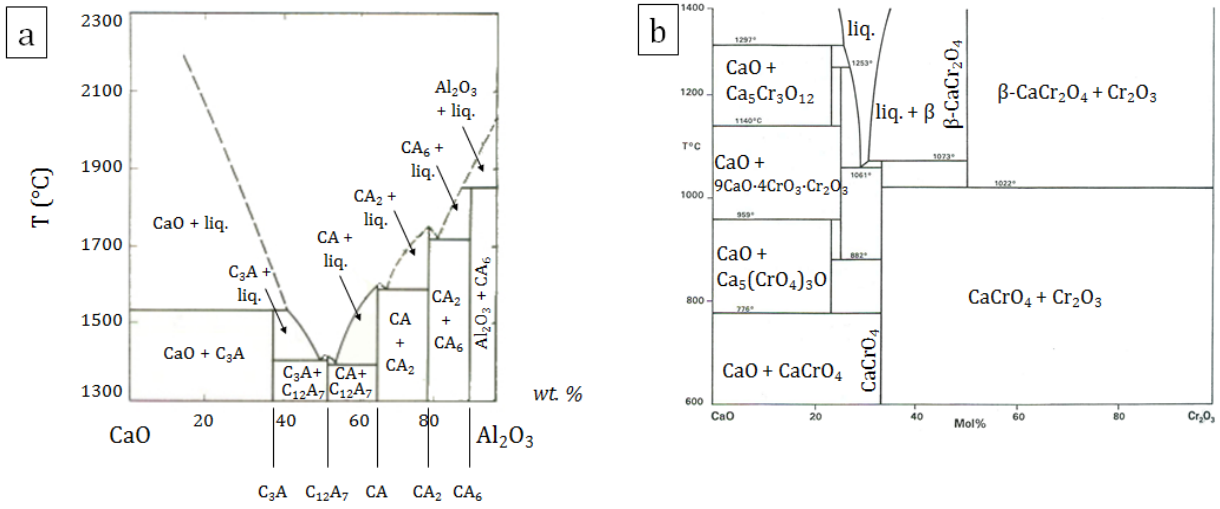

Figure 41: Phase diagrams. (a) $CaO\text{-}Al_2O_3$ system, adapted from Ref. [73]; (b) $CaO\text{-}Cr_2O_3$ system, adapted from Ref. [74]

Calcium oxide is known [75] to react with the chromium contained in MCrAlY alloys to form a low-melting calcium chromate, denoted here as L_{CaCrO}, which is liquid at 1100 °C ($T_{eutectic}$ = 1061 °C, see Figure 41b). The thickness of this layer was not uniform, which made measurements difficult. Qualitatively, the calcium chromate was found to develop rapidly on the γ-rich Ni-30Co-33Cr-12Al-0.1Y within 5 h exposure, and to not significantly thicken thereafter. Furthermore, the thin α-Al_2O_3 layer at the base of the corrosion product suggests that calcium chromate formed only during an initial transient stage. In order to test this hypothesis, Ni-20Co-16Cr-23Al-0.1Y and Ni-30Co-33Cr-12Al-0.1Y were oxidized with no deposit in dry air for 10 h at 1100 °C, growing a continuous Al_2O_3 scale. Upon subsequent exposure to CaO for 40 h in the same conditions, the Al_2O_3 reacted to yield calcium aluminates, but no calcium chromate was formed, confirming the transient nature of the latter.

The weight gains recorded by thermogravimetric analysis at 1100 °C, Figure 42, reflect the successive stages of the reaction process. Plots of $m = f\left(t^{1/2}\right)$ yielded straight lines after a sufficient time was reached (not shown here). This indicates that steady-state kinetics were parabolic for both alloys, with and without CaO deposits. In the absence of CaO, Ni-20Co-16Cr-23Al-0.1Y and Ni-30Co-33Cr-12Al-0.1Y exhibited similar oxidation kinetics: a short (~ 2 h) transient stage, associated with oxides of the base metal constituents and metastable alumina polymorphs, was followed by a steady-state corresponding to α-Al_2O_3 growth. Steady-state parabolic constants calculated from Figure 42 were found to be 3.7×10^{-7} and 4.5×10^{-7} $mg^2\ cm^{-4}s^{-1}$ (based on the convention $m^2 = 2k_p t$) for Ni-20Co-16Cr-23Al-0.1Y and Ni-30Co-33Cr-12Al-0.1Y, respectively, in good agreement with previously reported values for the growth of α-Al_2O_3 at this temperature [76, 77, 78]. In the presence of a CaO deposit, the rates of both transient and steady-state stages increased, and the transition was delayed. The effect of CaO was particularly marked in the case of Ni-30Co-33Cr-12Al-0.1Y, which exhibited a relatively large weight gain in the beginning of the reaction. Since a thick L_{CaCrO} + (Ni,Co)O layer formed on this alloy within 5 h exposure, and only small amounts were found on Ni-20Co-16Cr-23Al-0.1Y, the elevated reaction rate is attributed to L_{CaCrO} and (Ni,Co)O formation. This accelerated process was particularly short-lived (< 1 h). Until about 9 h exposure, both alloys maintained a relatively high reaction rate. The rate-limiting process associated with this period is not readily ascertained, as a continuous α-Al_2O_3 layer was identified by PSLS at the base of the scale for both alloys after 5 h reaction. Nevertheless, both alloys did passivate, and eventually reached slow reaction kinetics.

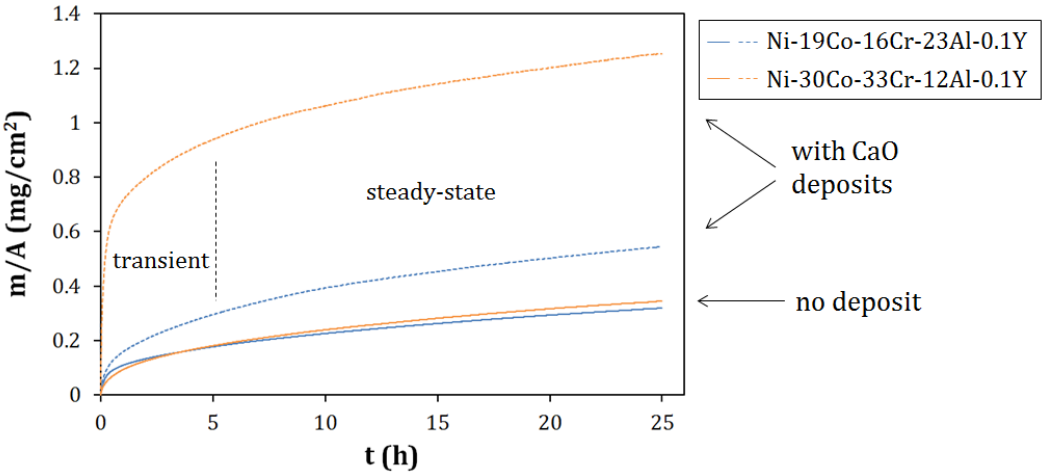

Figure 42: Weight gain recorded by TGA during reaction of Ni-19Co-15Cr-24Al-0.1Y and Ni-30Co-33Cr-12Al-0.1Y in dry air at 1100 °C.

An additional experiment was conducted with a Ni-33Co-35Cr-7Al-0.1Y alloy, which is single-phase γ at 1100 °C, and has a composition similar to that of the γ in Ni-30Co-33Cr-12Al-0.1Y at this temperature. After 50 h exposure to CaO, the 100 % γ alloy developed a reaction morphology similar to that on Ni-30Co-33Cr-12Al-0.1Y. However, the amount of L_{CaCrO} and (Ni,Co)O formed before passivation was much greater, and the ~ 150 µm thick calcium chromate had also embedded C_xA_y particles (Figure 43).

Chiang et al. [75] studied the reaction of nominally Al_2O_3-forming NiCrAl and CoCrAl alloys with CaO, and found that the formation of liquid calcium chromate led to very rapid alloy destruction. In the present study, the extent of metal loss due to L_{CaCrO} and (Ni,Co)O was seen to vary quite significantly with alloy composition and, in turn, alloy microstructure. The β-rich Ni-20Co-16Cr-23Al-0.1Y rapidly established continuous Al_2O_3 and C_xA_y layers, which prevented the oxidation of Cr, Ni or Co; whereas, the 100 % γ Ni-33Co-35Cr-7Al-0.1Y sustained extensive degradation before it could passivate, and the γ-rich Ni-30Co-33Cr-12Al-0.1Y had an intermediate behavior.

Aluminum and chromium strongly partition to the β and γ phases, respectively, as seen in Table 1. Thus γ will favor L_{CaCrO} formation, while β will tend to form Al_2O_3 and C_xA_y. As suggested by Chiang et al. [75], calcium chromate is formed by reaction of CaO with transient chromium oxide. Here the (Ni,Co)O particles embedded in the chromate were found to grow significantly with reaction time, which indicates that they did not precipitate on cooling, but instead developed at temperature. This is due to the fact that L_{CaCrO} dissolves very little (< 1 at. %) nickel or cobalt oxide: as the reaction front advances into the γ-phase, Ni and Co are rejected from the liquid and precipitate as oxide particles. Similarly, the solubility of Al_2O_3 in the chromate was measured by SEM-EDS to be quite low (1-2 at. %), as also reported by others [74]. This led to an Al:Cr elemental ratio of about 1:5, similar to that in the original γ phase in Ni-30Co-33Cr-12Al-0.1Y and Ni-33Co-35Cr-7Al-0.1Y. The conservation of this Al:Cr ratio indicates that the γ phase was consumed in situ by the rapidly advancing reaction front. However, some change in the boundary conditions, such as a decelerating reaction front and associated accumulation of Al in the alloy at the metal/oxide interface, must occur to allow for the eventual establishment of an Al_2O_3 layer.

Exactly how the alloy passivates remains unclear at this stage. Nevertheless, the implications of this reaction process are readily understood, in terms of alloy resistance to the severe degradation associated with liquid calcium chromate: metal loss should be minimized with a lower chromium content or a higher fraction of β. In particular, considerable resistance can be obtained by having a β fraction sufficiently high for the β phase to be continuous, as opposed to forming a dispersion in a γ matrix, as schematically represented in Figure 44. The β-rich Ni-20Co-16Cr-23Al-0.1Y did form a very small amount of L_{CaCrO} and (Ni,Co)O (Figure 40a); the large β fraction (57 %) simply allowed the progression of the liquid phase to be undercut by an Al_2O_3 layer sooner than in the γ-rich alloys.

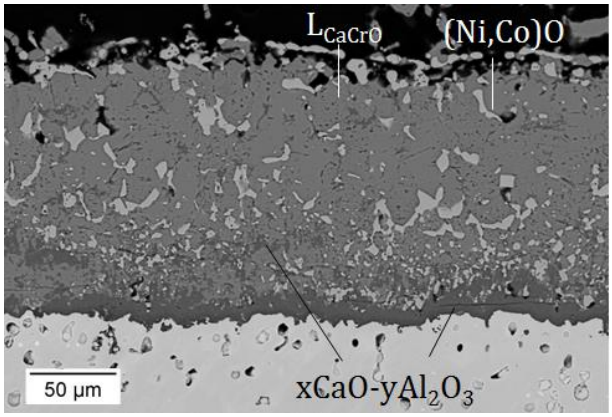

Figure 43: Reaction morphology observed after 50 h exposure of 100 % γ alloy Ni-33Co-35Cr-7Al-0.1Y in dry air with CaO at 1100 °C.

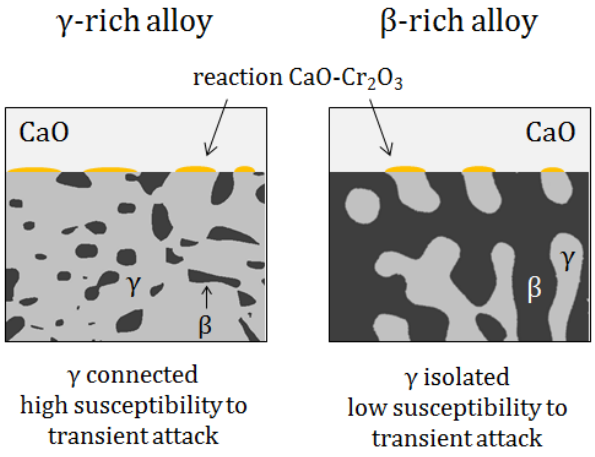

Figure 44: Schematics showing how the susceptibility for transient attack by CaO is determined by the distribution of the Cr-rich γ phase in the alloy.

3.2.3.2 Kinetics of Al_2O_3 production-destruction

Under isothermal conditions the stage of rapid alloy consumption due to liquid chromate formation is, in most cases, short lived, and followed by a steady-state regime of slower corrosion, permitted by the establishment of a continuous Al_2O_3 layer. However, this thermally growing Al_2O_3 reacts with the calcium and oxygen contained in L_{CaCrO}, or directly with the CaO deposit, to form C_xA_y layers. This has consequences on the reaction kinetics, which are considered in the following.

The case of Ni-19Co-15Cr-24Al-0.1Y, where very little L_{CaCrO} formed and the outermost C_xA_y layer was in contact with the CaO deposit, is considered first. Figure 45 shows a schematic of the reaction process. Calcium aluminate growth is known to be controlled by solid state Ca^{2+} diffusion [79, 80, 81]; its formation is therefore described to occur at the Al_2O_3/C_xA_y interface by the reaction

$$xCa^{2+} + xO^{2-} + yAl_2O_3 = C_xA_y \quad (3)$$

The oxygen and calcium necessary for this reaction are provided by the decomposition of CaO at the CaO/C_xA_y interface:

$$CaO = Ca^{2+} + O^{2-} \quad (4)$$

Two processes contribute to net Al_2O_3 growth: (i) its destruction to form C_xA_y according to Eq. (3) at the Al_2O_3/C_xA_y interface, and (ii) its production by oxidation of aluminum contained in the metal substrate,

$$2Al^{3+} + 3O^{2-} = Al_2O_3 \quad (5)$$

For the sake of simplicity, the latter is described to occur at the metal/oxide interface, with O^{2-} assumed to diffuse faster than Al^{3+}, but a mixed or even predominantly outward growth mechanism would not change the resulting kinetics. As illustrated in Figure 45, the oxygen necessary for Al_2O_3 growth is assumed to be supplied by solid-state diffusion across C_xA_y. This oxygen ultimately originates from the gas atmosphere, and it is further assumed that the oxygen provided by decomposition of CaO is entirely consumed to form C_xA_y. This prevents the accumulation of calcium or oxygen in C_xA_y, and is realistic insofar as all known calcium aluminates are intermediate $xCaO\text{-}yAl_2O_3$ compounds (Figure 41a), in which the degree of oxidation of Ca or Al is not different from that in CaO and Al_2O_3, respectively. In the case of the γ-rich Ni-30Co-33Cr-12Al-0.1Y alloy, the C_xA_y layers are surmounted by liquid calcium chromate; it is assumed that the latter can rapidly provide the oxygen and calcium required for C_xA_y and Al_2O_3 growth, and that this step is therefore not rate-limiting.

Several investigators have studied the growth kinetics of oxide scales that consist of multiple layers growing by diffusion of the same cation, taking into account the partitioning of the cation flux between the successive layers [82, 83, 84, 85, 86, 87]. The present situation is slightly different in that it involves two types of cations, but it is equivalent if one considers the diffusion of oxygen instead. Provided that the degree of oxidation of aluminum and calcium does not change upon forming any of the aluminates from CaO and Al_2O_3, the present situation is a particular, simple case of the general formalism introduced by Yurek et al. [83] for two-layer structures. That treatment provided a relationship between the thickening constant measured for each layer in the multi-layer scale and the "intrinsic" constants that would be observed if a single-layer of each individual oxide had formed.

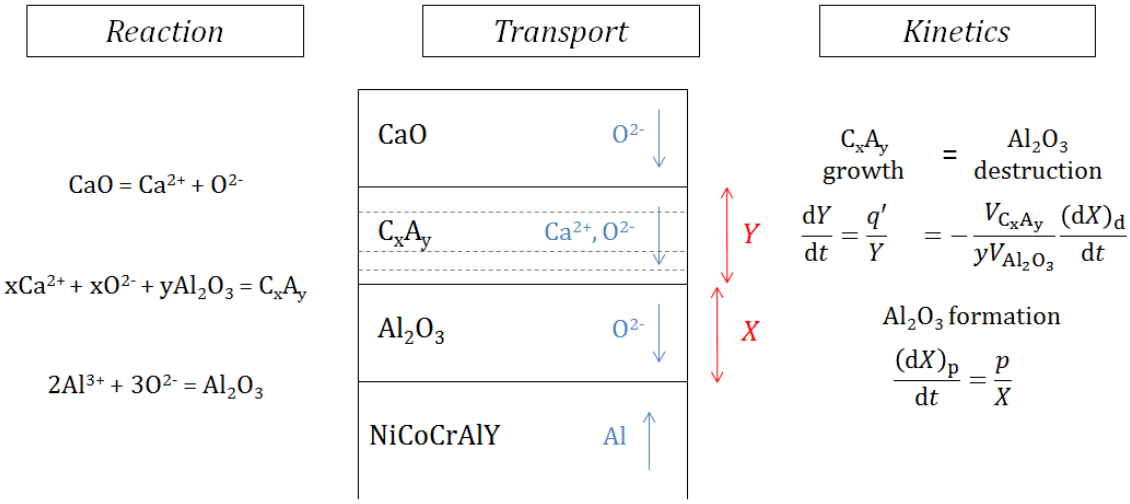

Figure 45: Schematic representation of the reactions and transport processes associated with the formation of calcium aluminate from CaO and thermally grown Al_2O_3.

Published studies of calcium aluminate growth mostly concern powders, and the reported rate constants tend to vary significantly depending on the starting materials and the method used to assess the results. In the absence of consistent data in the literature, the present analysis will rely on experimental data obtained here. The following considers the relationship between the constants measured for Al_2O_3 and C_xA_y in the multi-layer structure and the constant for individual Al_2O_3 growth, measured in the absence of a deposit. Since the stoichiometry and relative thicknesses of the aluminates do not affect the flux of oxygen used for the oxidation reaction, the aluminate layers are gathered into a single layer of average stoichiometry C_xA_y. Its thickening kinetics are described in accordance with the parabolic rate law

$$\frac{dY}{dt} = \frac{q'}{Y} \tag{6}$$

where Y is the thickness of C_xA_y in the Al_2O_3-C_xA_y scale, and q' is the associated parabolic constant. Since $Y(t=0)=0$, Eq. (6) yields

$$Y^2 = 2q't \tag{7}$$

Considering the mass balance underlying Eq. (3), the destruction term is written

$$\frac{(dX)_d}{dt} = -\frac{yV_{Al_2O_3}}{V_{C_xA_y}}\frac{dY}{dt} \tag{8}$$

where V_i is the molar volume of phase i. Using the TGA data of Figure 42, it can be shown that in the steady-state regime established in the absence of a deposit, Al_2O_3 grows according to parabolic kinetics. Previous findings discussed in Ref. [88] show that the rate-limiting step is grain-boundary diffusion of O^{2-} (or Al^{3+}). This still holds when there is concurrent C_xA_y formation, so long as the alloy can provide sufficient Al to sustain Al_2O_3 growth. Inasmuch as the constitution and predominant structure of Al_2O_3 grain boundaries remain unchanged, the instantaneous growth rate in a situation of production-destruction is inversely proportional to the oxide thickness, with the same constant as in the absence of a deposit. Thus the production term is written

$$\frac{(\mathrm{d}X)_\mathrm{p}}{\mathrm{d}t} = \frac{p}{X} \tag{9}$$

where X is the thickness of Al_2O_3 in the Al_2O_3-C_xA_y scale and p is the parabolic constant measured in a situation for exclusive oxidation.

The net Al_2O_3 growth is obtained by adding the two contributions:

$$\frac{\mathrm{d}X}{\mathrm{d}t} = \frac{(\mathrm{d}X)_\mathrm{p}}{\mathrm{d}t} + \frac{(\mathrm{d}X)_\mathrm{d}}{\mathrm{d}t} = \frac{p}{X} - \frac{yV_{\mathrm{Al_2O_3}}}{V_{\mathrm{C_xA_y}}}\frac{q'}{Y} \tag{10}$$

or, using Eq. (7),

$$\frac{\mathrm{d}X}{\mathrm{d}t} = \frac{p}{X} - \alpha\frac{q'}{\sqrt{2q't}} \tag{11}$$

where $\alpha = \frac{yV_{\mathrm{Al_2O_3}}}{V_{\mathrm{C_xA_y}}}$. This equation is solved to yield

$$\begin{cases} X^2 = 2p't \\ p' = \frac{1}{2}\left[2p + \alpha^2 q' - \alpha\sqrt{q'(4p + \alpha^2 q')}\right] \end{cases} \tag{12}$$

The form of Eq. (11) allows for another solution $p'' = \frac{1}{2}\left[2p + \alpha^2 q' + \alpha\sqrt{q'(4p + \alpha^2 q')}\right]$, with $p' < p < p''$. Since Al_2O_3 is being consumed by the reaction with the aluminate, p' is the appropriate solution. Noting that Al_2O_3 and C_xA_y have the same Al/O ratio, the same expression for p' can be obtained from the general equations given by Yurek et al. [83]. Based on that treatment, the relationships between the constants measured in the Al_2O_3-C_xA_y scale and the constants for individual Al_2O_3 and C_xA_y growth are

$$p' = \frac{p}{1 + \alpha\frac{Y}{X}} \tag{13}$$

$$q' = \frac{q}{1 + \frac{1}{\alpha}\frac{X}{Y}} \tag{14}$$

with the ratio of layer thicknesses in the multi-layer structure given by

$$\frac{Y}{X} = \alpha\frac{q}{p} \tag{15}$$

The analysis is now applied to the reactions of Ni-20Co-16Cr-23Al-0.1Y and Ni-30Co-33Cr-12Al-0.1Y. For each alloy, the intrinsic oxidation rate p is arrived at by fitting the TGA data measured with no CaO (Figure 42), while q' is determined from C_xA_y thickness measurements after 5, 25, 50 and 250 h exposures (Figure 46). The ratio $\alpha = yV_{\mathrm{Al_2O_3}}/V_{\mathrm{C_xA_y}}$ is calculated as the average of values obtained for CA and CA_2, which were found by SEM-EDS to constitute most of the C_xA_y. Values of p' calculated with Eq. (12) are shown in Table 7, together with constants obtained from direct measurement of Al_2O_3 thickness in Al_2O_3-C_xA_y scales (Figure 46). The latter are seen to be within an order of magnitude but significantly smaller than those obtained indirectly via Eq. (12), especially for the β-rich alloy. This will be discussed subsequently.

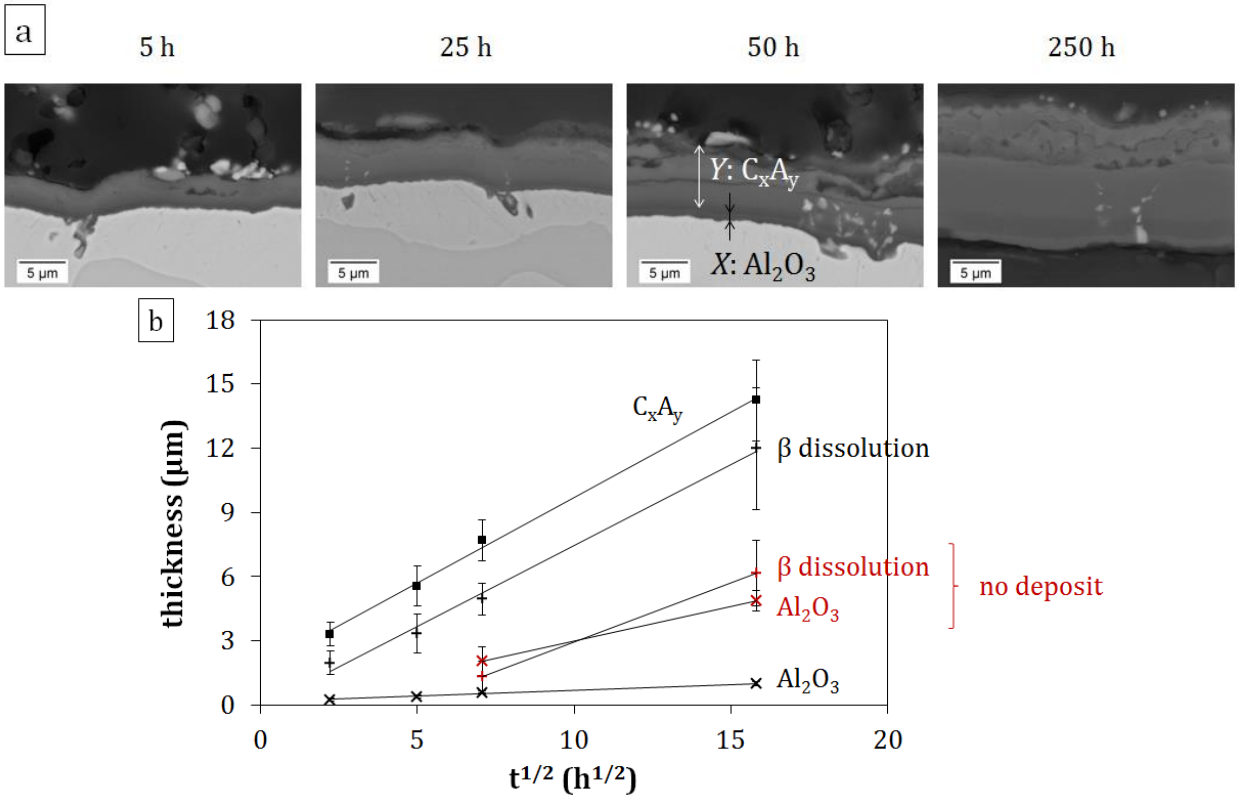

Figure 46: Thickness of C_xA_y and Al_2O_3 layers, and of β dissolution zone, measured after exposure of β-rich Ni-19Co-15Cr-24Al-0.1Y to CaO in dry air at 1100 °C. (a) micrographs; (b) parabolic plot. Alumina thickness and β dissolution depth measured in the same conditions without deposit are shown for comparison.

Table 7: Parabolic constants (10^{-14} cm^2 s^{-1}) for C_xA_y growth, and Al_2O_3 growth with and without CaO deposit, obtained from thickness or TGA measurements (see text for details).

		Ni-19Co-15Cr-24Al-0.1Y	Ni-30Co-33Cr-12Al-0.1Y
Al_2O_3 thickness	p'	0.41	1.9
TGA (no deposit)	p	11	13
C_xA_y thickness	q'	83	80
Eq. (12)	p'	2.7	3.7
TGA (with deposit)	r'	25	24
Eq. (22)	p'	4.5	6.9

After evaluating reaction kinetics based on direct thickness measurements, p' is now calculated using TGA data (Figure 42), which also reflect the rate at which the Al_2O_3 layer thickens. According to the description adopted here and represented in Figure 45, the

weight gain per unit of surface area recorded during an exposure to CaO corresponds to the oxygen uptake necessary for Al_2O_3 production:

$$\frac{\mathrm{d}m}{\mathrm{d}t} = \frac{\mathrm{d}m_{\mathrm{O}}}{\mathrm{d}t} = \frac{(\mathrm{d}m_{\mathrm{O}})_{\mathrm{p}}}{\mathrm{d}t} \tag{16}$$

No net weight gain arises from C_xA_y growth, as the Ca and O forming the x CaO units come from the CaO deposit, and the Al and O forming the y Al_2O_3 units come from the existing Al_2O_3 layer. The net oxygen uptake is related to the quantity of Al_2O_3 produced through the mass balance underlying Eq. (5):

$$\frac{1}{M_{\mathrm{O}}}(\mathrm{d}m_{\mathrm{O}})_{\mathrm{p}} = (\mathrm{d}n_{\mathrm{O}})_{\mathrm{p}} = 3\left(\mathrm{d}n_{\mathrm{Al_2O_3}}\right)_{\mathrm{p}} \tag{17}$$

where M_0 is the atomic weight of oxygen. Combining Eqs. (16) and (17), and converting the quantity of Al_2O_3 produced into an equivalent thickness, one obtains

$$\frac{\mathrm{d}m}{\mathrm{d}t} = \frac{3M_{\mathrm{O}}}{V_{\mathrm{Al_2O_3}}}\frac{(\mathrm{d}X)_{\mathrm{p}}}{\mathrm{d}t} \tag{18}$$

Using the TGA data of Figure 42, one can show that at steady-state, weight uptakes of both Ni-20Co-16Cr-23Al-0.1Y and Ni-30Co-33Cr-12Al-0.1Y in the presence of CaO obey a parabolic law

$$m^2 = 2s't \tag{19}$$

where s' is the gravimetric rate constant. It follows from Eq. (18) that Al_2O_3 production also obeys parabolic kinetics, which is written

$$\frac{(\mathrm{d}X)_{\mathrm{p}}}{\mathrm{d}t} = \frac{r'}{\sqrt{2r't}} \tag{20}$$

where $r' = s'\left(\frac{V_{\mathrm{Al_2O_3}}}{3M_{\mathrm{O}}}\right)^2$ is the parabolic constant related to the rate at which Al_2O_3 thickens by oxidation of the alloy in the Al_2O_3-C_xA_y structure. This production rate is inversely proportional to the layer thickness, Eq. (9), which yields

$$\frac{p}{X} = \frac{r'}{\sqrt{2r't}} \tag{21}$$

Considering that $X(t=0)=0$, Eq. (21) is solved to provide

$$\begin{cases} X^2 = 2p't \\ p' = \dfrac{p^2}{r'} \end{cases} \tag{22}$$

Thus p' can be calculated from r' and p, which are obtained by fitting TGA data recorded with and without CaO deposit, respectively. The results are seen in Table 7 to be in reasonable agreement with those obtained with Eq. (12), although slightly higher.

Two observations should be made from the p' values presented in Table 7. First, for a given alloy, a significant discrepancy exists between the values obtained with the three methods used. This is particularly the case for the β-rich alloy, where the value corresponding to direct thickness measurements is much lower than the calculated values. The difference is beyond possible experimental errors, and must instead reflect the incomplete satisfaction of the limiting assumptions made here. First, analysis by SEM-EDS showed small amounts (1-2 at. %) of chromium in the C_xA_y, and of aluminum in the L_{CaCrO}. This slightly affects the mass balance underlying Eq. (12) and the interpretation of the TGA data, via Eq. (17). Furthermore, some aspects of the complexities associated with Al_2O_3

growth were not accounted for in the present analysis. For instance, one aspect is related to the choice of boundary conditions: the oxygen activity at the Al_2O_3 surface was assumed to be the same whether calcium aluminates form or not, although some p_{O_2} gradient probably exists across the layers in the Al_2O_3-C_xA_y scale. This arguably does not affect p' significantly, inasmuch as Al_2O_3 predominantly exhibits n-type behavior, and its growth rate is little affected by the external p_{O_2} [88]. Further, oxidation both with and without CaO involves a transient stage, as shown by the TGA data in Figure 42, which possibly comprises the formation of metastable Al_2O_3 polymorphs, base-metal oxides or L_{CaCrO} prior to the establishment of α-Al_2O_3 and C_xA_y layers. One can show that the extent of these processes does not directly affect the thickening rate achieved during steady-state. (Specifically, using equations of the form $(x - x_i)^2 = 2k(t - t_i)$ or $x^2 - x_i^2 = 2k(t - t_i)$ to describe Al_2O_3 or C_xA_y growth does not change the expression giving p' in Eq. (12) for sufficiently long reaction times.) However, in accordance with the analysis of Brumm and Grabke [78], aspects of transient oxidation such as the time needed for the θ→α transformation do have an influence on the microstructure of Al_2O_3, in particular its grain size, and therefore affect growth rates observed on the longer term. In this respect, because of the p-type nature of θ-Al_2O_3 [89, 90, 91], a reduced p_{O_2} at the oxide surface in the presence of C_xA_y could have an indirect effect on the α-Al_2O_3 eventually established, by slowing the growth of the metastable polymorph. Due to its high reactivity, the presence of CaO certainly had an impact on the transient stage of the reaction, as evident in Figure 42, although potential effects on Al_2O_3 microstructure were beyond the scope of this investigation.

A second observation arising from the data gathered in Table 7 is that a significant difference exists between the p' values obtained for the two alloys, which is not accounted for in the present analysis. This is most evident when considering p' from direct Al_2O_3 thickness measurements. Similarly, the C_xA_y-to-Al_2O_3 thickness ratio, while approximately constant with time for each alloy as expected for diffusion-controlled growth processes, was found to be quite different for the two alloys: 12.8 ± 0.8 for Ni-20Co-16Cr-23Al-0.1Y, versus 6.2 ± 0.2 for Ni-30Co-33Cr-12Al-0.1Y. This could possibly be due to a difference in the constitution of the C_xA_y scale, as varying relative thicknesses would affect the average scale stoichiometry. This could not be assessed with sufficient accuracy because of the non-uniform, locally rumpled morphology of the reaction product. Another potential effect is related to the presence of liquid calcium chromate. In the case of the γ-rich alloy, the calcium and oxygen required for C_xA_y and Al_2O_3 growth must be provided by the L_{CaCrO} which forms a thick and continuous layer. If ionic transport in the liquid is not sufficiently rapid, it could limit the rate of C_xA_y growth, and allow a relatively thicker Al_2O_3 to persist. Furthermore, a slow transport would also involve a local chromium enrichment in the liquid, and, since the latter occupies a small composition range at 1100 °C (Figure 41b), this could result in the precipitation of $CaCr_2O_4$. The phase transformation would involve a partial reduction of chromium (the liquid contains a mixture of Cr III and Cr VI, while $CaCr_2O_4$ contains only Cr III), which would affect oxygen both in the mass balance underlying Eq. (12) and in the interpretation of the TGA data, via Eq. (16). Again the constitution of the L_{CaCrO} could not be characterized with the degree of accuracy required because of experimental limitations.

Overall, the present results indicate that beyond a reduction in thickness, the growth mechanism of Al_2O_3 is affected by the reaction with CaO. The details of the associated

processes, as well as the role played by alloy composition, are outside the scope of the present work and deserve further investigation. Yet, the present analysis is useful in that it provides a semi-quantitative evaluation of the effect of CaO on the rate of Al consumption. In essence, as Al_2O_3 reacts to form C_xA_y, its thickness is reduced, and so is its ability to act as a diffusion barrier: the instantaneous oxidation rate p/X increases. This rate is expressed as $(\mathrm{d}X)_\mathrm{p}/\mathrm{d}t = p/\sqrt{2p't}$, and since $p' < p$, it is indeed larger than its CaO-free counterpart, $p/\sqrt{2pt}$. Another metric that can be used to characterize Al consumption is the rate of β dissolution. Due to the larger oxidation rate, β is dissolved at a greater rate in the presence of CaO, as seen in Figure 46. Extrapolation of the observed kinetics provides an estimation of the time needed for β depletion over half the thickness of a typical 7.5 mil (190 μm) bondcoat: 16,000 h in the presence of CaO, versus 31,000 h in a situation of pure oxidation. Of course this estimate is an extreme, as it corresponds to the case where the bondcoat would continuously be in contact with a CaO-rich fly ash at 1100 °C. At this temperature, interdiffusion with the superalloy substrate would probably more relevant as a limiting factor. Furthermore, the present experiments showed that calcium aluminate scales were particularly prone to spallation upon cooling. In an actual gas turbine where maintenance periods impose some amount of thermal cycling, the presence of CaO-rich fly ash in contact with the bondcoat would potentially cause even more damage, as spallation of the corrosion product would expose an Al-depleted coating, which would then be particularly subject to liquid calcium chromate formation.

3.2.3.3 Effect of gas composition and temperature on reaction with CaO

Advancing toward more complex exposure conditions, the γ-rich alloy Ni-30Co-27Cr-12Al-0.1Y was used in a series of experiments involving Al_2O_3-40 wt. % CaO deposits. In CO_2-H_2O-O_2 at 1100 °C, the alloy formed C_xA_y and Al_2O_3 layers, but no calcium chromate (Figure 47a). This is attributed to the lower alloy Cr content (27 at. %, versus 33 at. % for the alloy studied in Section 3.2.3), and to the presence of Al_2O_3 in the deposit itself, which partially neutralized CaO by forming calcium aluminates. Based on the results presented in Section 3.2.2, the presence of CO_2 and H_2O in the gas is deemed to not have played a significant role. Changing the gas to O_2-SO_2, however, suppressed the formation of calcium aluminates. As shown in Figure 47b, small amounts of Cr and Co oxides were found mixed with the deposit, but the Al_2O_3 scale was not found to have reacted and overall no significant alloy consumption occurred. This can be understood by considering the relative stability of calcium sulfate and calcium aluminate in the presence of SO_3. As seen in the predominance diagram of Figure 48, CaO is not stable in the O_2-SO_2 mixture of interest. Furthermore, $CaSO_4$ is more stable than most calcium aluminates. Only one of the displacement reactions,

$$CaSO_4 + 6Al_2O_3 = CA_6 + SO_3 \quad (23)$$

is thermodynamically possible, but it involves an Al_2O_3-rich compound which was not previously seen to grow significantly fast – this would result in minimal Al_2O_3 destruction. Essentially, CaO has been neutralized because of the pronounced stability of $CaSO_4$ in the SO_3-containing atmosphere.

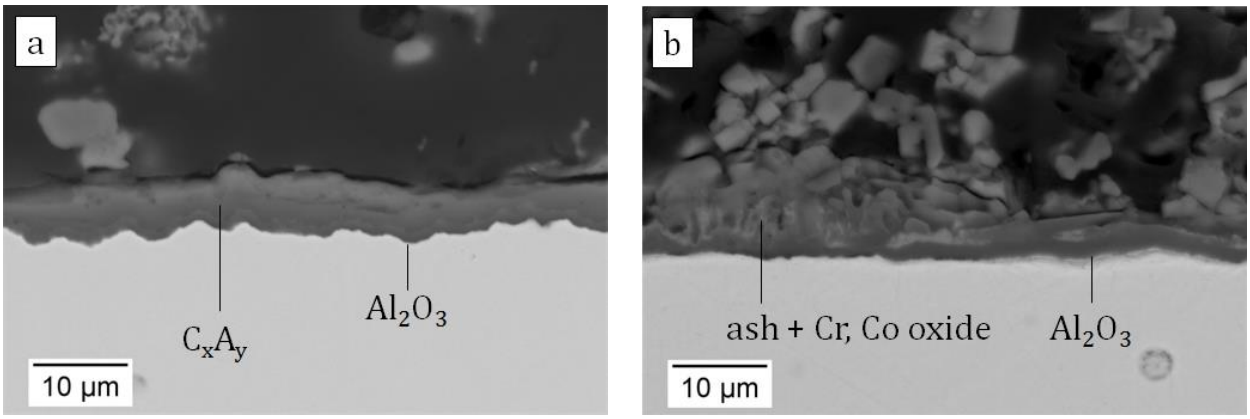

Figure 47: Reaction morphology observed after 50 h exposure of γ-rich Ni-30Co-27Cr-12Al-0.1Y to Al_2O_3-CaO in (a) CO_2-H_2O-O_2 and (b) O_2-SO_2 at 1100 °C.

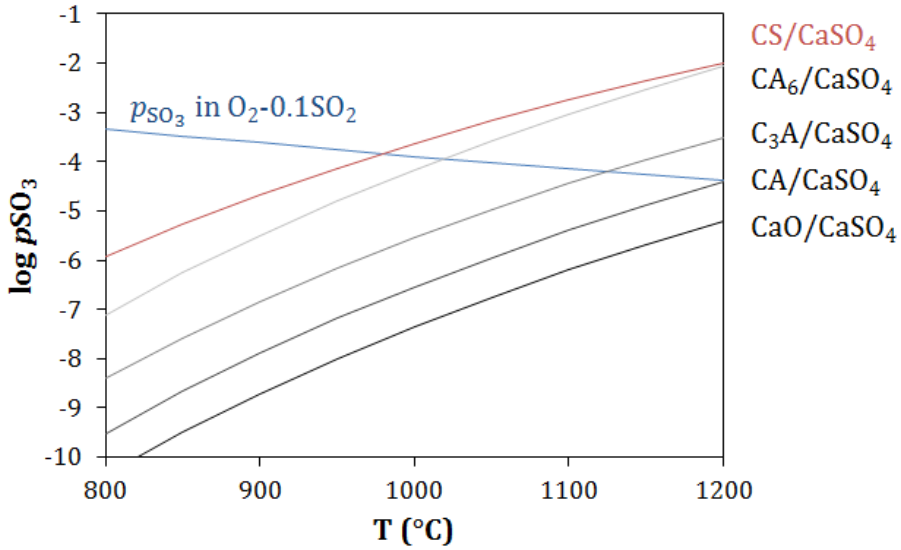

Figure 48: Predominance diagram (log pSO_3 vs temperature) for calcium oxide, aluminates and silicate versus calcium sulfate, based on the general displacement reaction: $xCaSO_4 + yA = C_xA_y + xSO_3$. Cement notation employed: C = CaO, S = SiO_2, A = Al_2O_3. Also includes equilibrium pSO_3 in O_2-0.1SO_2. All results were obtained from data in HSC software [92].

Reaction of the same alloy with Al_2O_3-CaO in the SO_3-free mixture CO_2-H_2O-O_2 at 900 °C resulted in a situation of non-selective oxidation, where significant amounts of (Ni,Co)O oxide were formed, and no passivation was observed after 50 h. As shown in Figure 49, an Al-rich oxide layer is present at the base of the corrosion product, but protrusions grow inward into the alloy: the alloy/Al_2O_3 interface is not kinetically stable. In the absence of a CaO deposit, oxidation of this alloy at 900 °C led to the formation of an Al_2O_3 scale surmounted by a layer of mixed Cr-Co-Ni oxide, and, locally, of shallow (~1 μm deep) Al_2O_3 protrusions. Furthermore, the θ→α transformation was not complete after 50 h. Surface PSLS characterization (not shown here) showed that while most of the surface consisted of α-Al_2O_3, a significant fraction was still predominantly θ.

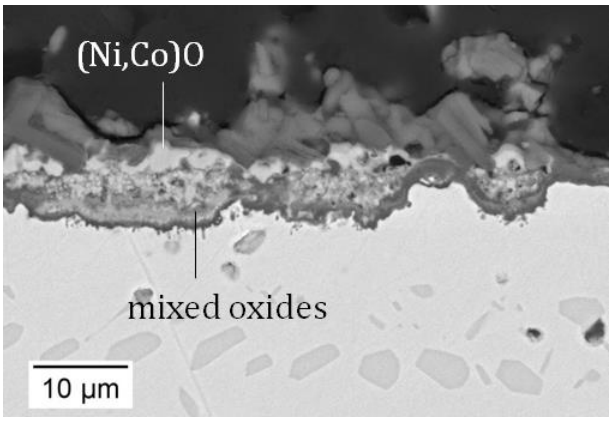

Figure 49: Reaction morphology observed after 50 h exposure of γ-rich Ni-30Co-27Cr-12Al-0.1Y to Al_2O_3-CaO in CO_2-H_2O-O_2 at 900 °C.

In order to rationalize the alloy failure to form and maintain an external Al_2O_3 scale when exposed to Al_2O_3-CaO at 900 °C, it is useful to consider Wagner's [93] criterion for sustained Al_2O_3 growth. Briefly, this is based on the principle that external Al_2O_3 growth can be sustained so long as the outward Al flux in the metal at the interface with the oxide equals the flux required for the oxide to grow. A maximum flux is obtained in the alloy when the interfacial Al content is set to zero. This defines the minimum bulk concentration for external Al_2O_3 growth, N^*_{Al}. Under the assumptions of parabolic oxidation kinetics and of a constant Al diffusion coefficient in the alloy (D_{Al}) in the composition range of interest, N^*_{Al} is given by [93]

$$N^*_{Al} = F\left(\sqrt{\frac{1}{2}\frac{k_{\mathrm{c}}}{D_{\mathrm{Al}}}}\right) \tag{24}$$

where F is the auxiliary function defined by $F(u) = \sqrt{\pi}u(1-\operatorname{erf} u)\exp(u^2)$ and k_{c} the parabolic constant for metal recession, defined by $d^2 = k_{\mathrm{c}}t$ with d the depth of the metal/oxide interface relative to the original alloy surface. In a situation of individual Al_2O_3 growth, the mass balance on the Al contained in the oxide scale is written

$$\frac{2X}{V_{\mathrm{Al_2O_3}}} = \frac{d}{V_{\mathrm{a}}} \tag{25}$$

with V_{a} the molar volume of the alloy, which yields a simple relationship between k_{c} and p

$$k_c = \left(\frac{2V_{\mathrm{a}}}{V_{\mathrm{Al_2O_3}}}\right)^2 p \tag{26}$$

and

$$N^*_{Al} = F\left(\frac{2V_{\mathrm{a}}}{V_{\mathrm{Al_2O_3}}}\sqrt{\frac{p}{2D_{\mathrm{Al}}}}\right) \tag{27}$$

Ihen Al_2O_3 reacts with CaO to form calcium aluminates, Eq. (25) becomes

$$\frac{2X}{V_{\mathrm{Al_2O_3}}} + \frac{2yY}{V_{\mathrm{C_xA_y}}} = \frac{d}{V_{\mathrm{a}}} \tag{28}$$

Using Eqs. (7) and (12), Y can be written

$$Y = \frac{V_{C_xA_y}}{yV_{Al_2O_3}}\left(\sqrt{2\frac{p^2}{p'}t} - X\right) \tag{29}$$

and the relationship giving k_c from measurable constants becomes

$$k_c = \left(\frac{2V_a}{V_{Al_2O_3}}\right)^2 \frac{p^2}{p'} \tag{30}$$

which finally yields

$$N^*_{Al} = F\left(\frac{2V_a}{V_{Al_2O_3}}\sqrt{\frac{p^2/p'}{2D_{Al}}}\right) \tag{31}$$

A comparison between Eqs. (26) and (30), or Eqs. (27) and (31), shows that changing from an individual Al_2O_3 scale to a multi-layer Al_2O_3-C_xA_y scale amounts to replacing p by p^2/p' when considering the flux of Al incorporated in the reaction product.

This analysis is now used to study the effect of a varying temperature on the reaction of Ni-30Co-27Cr-12Al-0.1Y with Al_2O_3-CaO deposits. No measured value of p or p' is available for this alloy; instead, N^*_{Al} is evaluated as follows. The constant p is taken from data by Brumm and Grabke [78] for α and θ-Al_2O_3 growth on NiAl-Cr alloys, using activation energies of 350 and 231 kJ/mol, respectively. In the absence of direct data, q is first calculated at 1100 °C from Eqs. (14) and (15) using q' measured here for Ni-30Co-33Cr-12Al-0.1Y (Table 7) and p for α-Al_2O_3 in Ref. [78]. Activation energies reported in the literature for the growth of calcium aluminates vary widely [79], with most values in the 150-250 kJ/mol range [81]; the median 200 kJ/mol is used here, in good agreement with results reported in Refs. [80, 94]. Values of q at varying temperatures are then calculated from q at 1100 °C, based on the Arrhenius equation. Constants p' and q' are then obtained for each of α and θ-Al_2O_3 using Eqs. (13) to (15) and the constants for individual Al_2O_3 (p) and C_xA_y (q) growth. Interdiffusion in a 5-component, 2-phase alloy system is complex. Since β is quite rapidly depleted from the subsurface of the γ-rich alloys, only diffusion in γ is considered. Nesbitt and Heckel [95] published experimental interdiffusion data for the ternary Ni-Cr-Al system, including a regression equation allowing interdiffusion coefficients to be calculated as a function of alloy composition. Chromium concentration gradients were seen to have little effect on Al diffusion, such that the main term $\widetilde{D}^{Ni}_{Al,Al}$ was prevalent. At 1100 °C, replacing Co by Ni and ignoring Y, one calculates $\widetilde{D}^{Ni}_{Al,Al} = 3.4 \times 10^{-10}$ cm^2 s^{-1} for the nominal composition (27Cr, 12Al), and $\widetilde{D}^{Ni}_{Al,Al} = 1.1 \times 10^{-10}$ cm^2 s^{-1} for an alloy fully depleted of its Al. Equation (31) is based on a constant diffusion coefficient; the average value $\widetilde{D}^{Ni}_{Al,Al} = 2 \times 10^{-10}$ cm^2 s^{-1} is chosen as an approximation. This value is consistent with other experimental and calculated values for dilute NiCrAl alloys at 1100 °C gathered in Ref. [96]. The activation energy for $\widetilde{D}^{Ni}_{Al,Al}$, 288 kJ/mol, is taken from Ref. [95].

Minimum Al concentrations calculated using Eq. (31) are plotted as a function of temperature in Figure 50 for both α and θ-Al_2O_3 growth, with and without CaO reaction. All predicted N^*_{Al} values are below the alloy nominal Al content (12 at. %). Considering α-Al_2O_3 at 1100 °C, the reaction with CaO leads to a relatively small increase of N^*_{Al}, from 1.2 at. % with no deposit to 2.8 at. % with CaO. This is consistent with the observed ability of Ni-30Co-27Cr-12Al-0.1Y to maintain an external Al_2O_3 layer at this temperature. For α-Al_2O_3

reaction with CaO, the 900 °C value of N_{Al}^{*}, 4.9 at. %, is higher than the 1100 °C value, but still relatively low. This indicates that the decrease in the alloy diffusion rate is partly compensated by the slowing of diffusion in Al_2O_3 and C_xA_y. However, PSLS measurements showed that θ-Al_2O_3 was still present in significant amounts after 50 h at 900 °C, which suggests that the metastable polymorph controlled the oxidation rate for an extended period at this temperature. Indeed, several investigators [77, 78] have shown that a temperature decrease from 1100 to 900 °C considerably delayed the θ→α transition. The value of N_{Al}^{*} calculated for θ-Al_2O_3 reaction with CaO at 900 °C, 8.1 at. %, is significantly higher than that obtained for α-Al_2O_3.

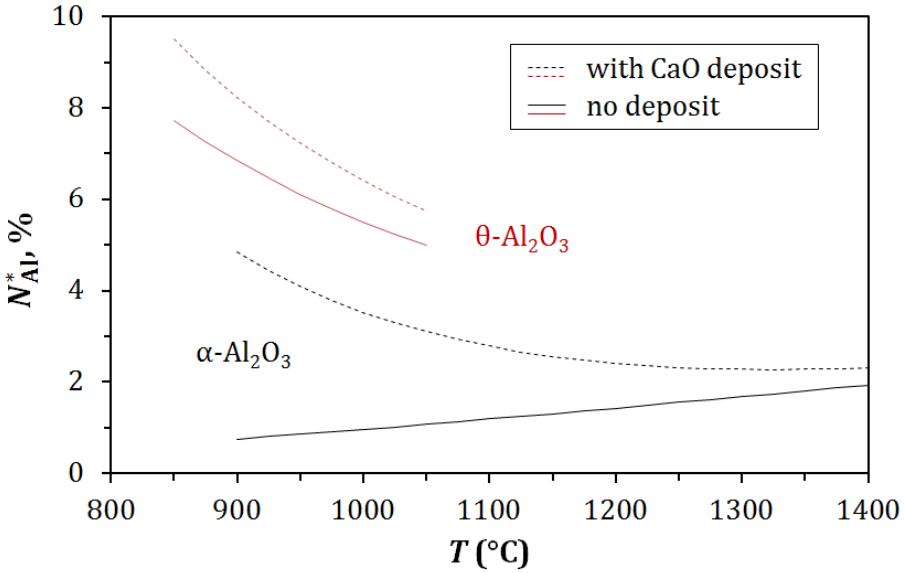

Figure 50: Minimum bulk Al content to maintain external Al_2O_3 growth with and without CaO reaction as a function of temperature. Calculated from Eqs. (27), (31), and parameters described in text.

Uncertainties in the activation energies and the limiting assumptions used here are such that predicted N_{Al}^{*} values should be regarded as rough estimates. Nevertheless, the trends are valid and indicate that reaction with CaO will be significantly more severe in terms of Al consumption, relative to its availability at the metal/oxide interface, at 900 °C than at 1100 °C. This is mainly due to the persistence of θ-Al_2O_3 at the lower temperature. These observations are consistent with the observed failure of Ni-30Co-27Cr-12Al-0.1Y to passivate in the presence of CaO at 900 °C.

The above analysis neglects the multi-phase nature of the alloys studied here. Compositional changes in oxidizing multi-phase alloys have been studied in the past [97, 98, 99]. Applying a diffusional analysis to β-γ alloys shows that for a given bulk composition, the interfacial aluminum flux in steady-state conditions is greater when γ contains more Al and the volume fraction of β is correspondingly smaller. This is particularly evident using the analytical method of Ref. [97], as the minimum bulk concentration to maintain Al_2O_3 scaling according to Wagner's criterion, i.e., N_{Al}^{*} in Eq. (24),

is to be replaced by the expression $\sqrt{N_{\mathrm{Al}}^{\gamma}\left[N_{\mathrm{Al}}^{\gamma}+2f_{\beta}\left(N_{\mathrm{Al}}^{\beta}-N_{\mathrm{Al}}^{\gamma}\right)\right]}$, where N_{Al}^{i} is the Al mole fraction in phase *i* and f_{β} is the volume fraction of β. In the case of the Ni-30Co-27Cr-12Al-0.1Y alloy, as the temperature decreases, f_{β} increases, which is compensated by a decrease in N_{Al}^{γ}, from 9.7 at. % at 1100 °C to 7.3 at % at 900 °C (measured by SEM-EDS). This results in a reduced interfacial Al flux, and further weighs against the alloy ability to sustain Al_2O_3 growth at the lower temperature.

To conclude this series of experiments using Al_2O_3-CaO deposits, the Ni-30Co-27Cr-12Al-0.1Y alloy was reacted in O_2-SO_2 at 900 °C. As shown in Figure 51a, the alloy developed locally different reaction morphologies, which reflect an evolution consistent with that identified in the case of class C ash at 1100 °C (see Section 3.2.2): inward growth of Al_2O_3 protrusions from an initially protective scale, formation of an outer Cr-rich oxide layer and of a new Al_2O_3 layer across the base of the protrusions, oxidation of the metal located above the passive layer. In some regions however, no continuous Cr-rich oxide layer is present, and the mixed oxide contains significant amounts (3-5 at. %) of Ca and S. In these regions the passive layer locally shows early signs of disruption (small protrusions and internal oxide particles), indicating that an active, non-protective type of corrosion could possibly persist. In the gas of interest at 900 °C, $CaSO_4$ is much more stable than any calcium aluminate (see Figure 48). The process of Al_2O_3 disruption does not then involve a displacement reaction like Eq. (23), but rather the formation of another type of compound, possibly a mixed sulfate. Indeed, in an experiment carried out in the same conditions but directly using $CaSO_4$ as the deposit, a distinct yet undefined phase was formed of approximate composition (at. %) 10Al-10Cr-4Ca-5S-71O, and the alloy showed signs of non-selective oxidation (Figure 51b). The mixed oxide regions growing below the original alloy surface were seen to be Al- and Cr-rich, with significant sulfur enrichment. These features are characteristic of a hot corrosion type of attack, even though no liquid phase is known to exist in this system at this temperature. Further investigations are needed to better comprehend this $CaSO_4$-induced attack.

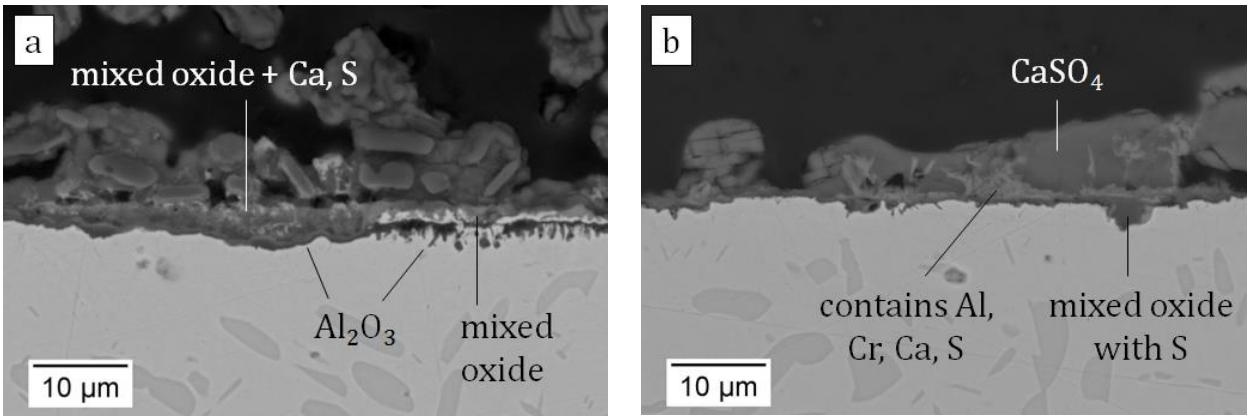

Figure 51: Reaction morphology observed after 50 h exposure of γ-rich Ni-30Co-27Cr-12Al-0.1Y to (a) Al_2O_3-CaO and (b) $CaSO_4$ in O_2-SO_2 at 900 °C.

3.2.4 Reaction with oxide, sulfate, and oxide-sulfate mixtures

The preceding sections were focused on degradation modes induced by CaO and $CaSO_4$. The scope is now extended to various oxide-sulfate mixtures, with the aim of identifying the key aspects of corrosion by industrial fly ash. It is first noted that while reaction with class-C ash in dry air at 1100 °C produced significant degradation (Figure 36), exposure to either a deposit of the same composition with no sulfate, or to Na_2SO_4 alone, in the same conditions, resulted in exclusive Al_2O_3 scaling. Similarly, no attack was observed when using a series of mixtures based on a SiO_2-rich composition similar to class F fly ash ($50SiO_2$-$25Al_2O_3$-$10CaO$-$10Fe_2O_3$-$5MgO$, in wt. %), prepared with the addition of K_2SO_4 (Figure 52a), or with increasing CaO contents (up to 46 wt. %, Figure 52b), the other constituents being held in a constant ratio. We thus observed that in isothermal conditions at 1100 °C, external Al_2O_3 was readily established and maintained in the presence of most realistic ash mixtures. Cases of Al_2O_3 failure were specific to γ-rich alloys contacted with deposits combining some sulfate and a high CaO concentration.

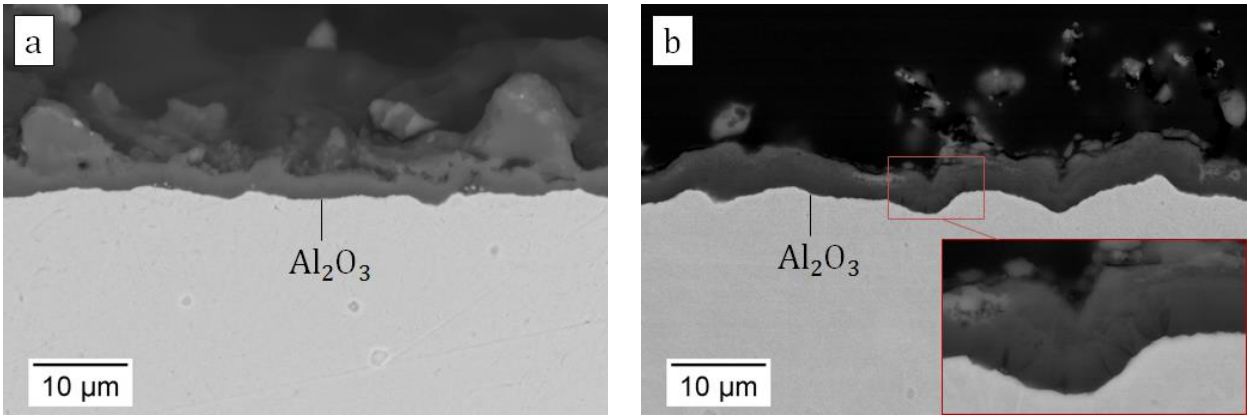

Figure 52: Reaction morphology observed after 50 h exposure of γ-rich Ni-30Co-30Cr-12Al-0.1Y to (a) SiO_2-$24Al_2O_3$-$10CaO$-$10Fe_2O_3$-$5MgO$-$5K_2SO_4$ and (b) SiO_2-$15Al_2O_3$-$46CaO$-$6Fe_2O_3$-$3MgO$ in dry air at 1100 °C. Deposit compositions in wt. %.

In order to refine this preliminary observation, a variety of ash mixtures were prepared by combining the following "building blocks": an acidic oxide (Al_2O_3 or SiO_2), a basic oxide (CaO or MgO) and a sulfate (Na_2SO_4). Since the gas p_{SO_3} was found to play a significant role during reaction with $CaO/CaSO_4$, experiments were conducted in an SO_3-free gas (CO_2-H_2O-O_2) and in O_2-SO_2, at 900 and 1100 °C. The γ-rich Ni-30Co-27Cr-12Al-0.1Y alloy was used for all exposures. This represents a large amount of experimental results; the most significant are presented here.

Reaction in CO_2-H_2O-O_2 at 1100 °C is considered first. Taking the results obtained with Al_2O_3-CaO (Figure 47) as a baseline, it is found that adding 30 wt. % SiO_2 at the expense of Al_2O_3 suppresses calcium aluminate formation. Transient oxidation of Cr, Co and Ni was more important with Al_2O_3-SiO_2-CaO than in the absence of a deposit, but no sign of reaction with the thermally grown Al_2O_3 scale was found (Figure 53a). Analysis of the deposit after exposure showed that CaO had preferentially reacted with SiO_2 to form

$CaSiO_3$. This is due to the greater stability of the silicate, compared to the aluminates (Table 8). The addition of 10 wt. % Na_2SO_4 to this oxide mixture, however, resulted in significant degradation (Figure 53b), as the alloy developed a reaction morphology much alike that observed with class C ash.

Table 8: Standard free energy of formation of calcium silicates and aluminates per unit CaO, $\Delta_r G^0$ (kJ/mol-CaO). Cement notation employed: C = CaO, S = SiO_2, A = Al_2O_3. Data from HSC Chemistry [92].

T (°C)	900	1100
Calcium silicates		
CS	-90.8	-90.7
1/2 C_2S	-69.0	-70.7
1/3 C_3S	-43.6	-45.0
1/3 C_3S_2	-82.8	-83.6
Calcium aluminates		
CA	-42.0	-45.8
CA_2	-54.5	-60.6
CA_6	-72.1	-83.1
1/2 C_2A	-6.5	-6.8
1/3 C_3A	-18.4	-21.2
1/12 $C_{12}A_7$	-29.0	-32.9

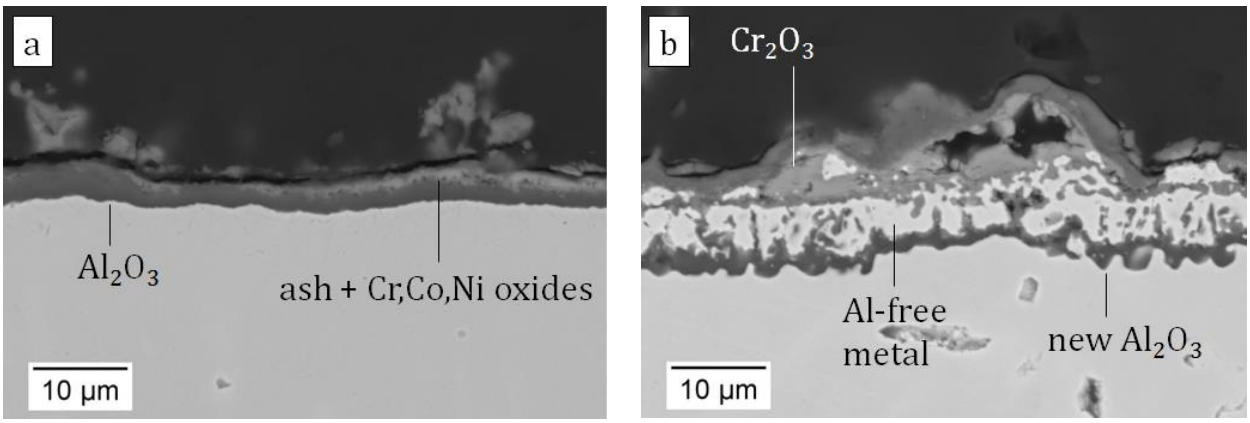

Figure 53: Reaction morphology observed after 50 h exposure of γ-rich Ni-30Co-27Cr-12Al-0.1Y to (a) Al_2O_3-30SiO_2-40CaO and (b) Al_2O_3-25SiO_2-40CaO-10Na_2SO_4 in CO_2-H_2O-O_2 at 1100 °C. Deposit compositions in wt. %.

Similar observations were made after reaction in the O_2-SO_2 atmosphere: no calcium aluminates were formed, and exposure to the Al_2O_3-SiO_2-CaO-Na_2SO_4 deposit also produced significant corrosion (Figure 54). It is noted however that in the latter case, the reaction product was different from that formed in CO_2-H_2O-O_2. In the SO_3-containing gas, the Al_2O_3 layer at the base of the corrosion product was interrupted by Cr-rich sulfides, also present

as internal particles in the alloy. The rest of the scale was a multiphase mixture composed of Cr-rich oxide and ash constituents. Overall, the extent of corrosion was more important than in the SO_3-free gas. In particular, (i) no Cr-rich oxide layer was developed in the outer part of the corrosion product, which allowed the ash to contact the alloy, and (ii) sulfidation at the metal/oxide interface seemed to hamper repassivation. Remarkably, reaction with Al_2O_3-Na_2SO_4 and Al_2O_3-CaO-Na_2SO_4 mixtures in O_2-SO_2 did not cause non-selective oxidation. This indicates that while the presence of Na_2SO_4 in the deposit is necessary to trigger Al_2O_3 failure at 1100 °C, the composition of the oxide mixture associated with the sulfate is also very important. In particular, some SiO_2 must be present for the attack to proceed.

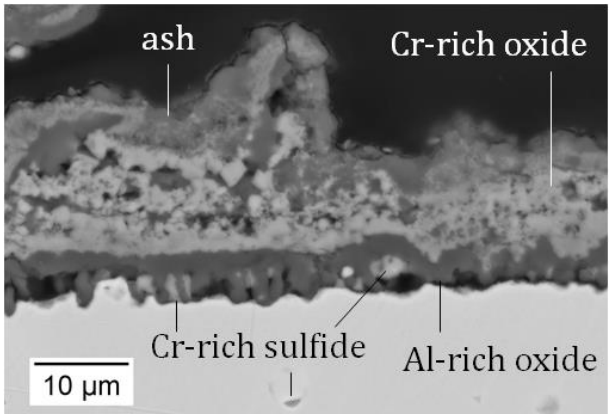

Figure 54: Reaction morphology observed after 50 h exposure of γ-rich Ni-30Co-27Cr-12Al-0.1Y to Al_2O_3-25SiO_2-40CaO-10Na_2SO_4 in O_2-SO_2 at 1100 °C. Deposit composition in wt. %.

Regarding the role of gaseous sulfur, it is noted that the corrosion products peeled off from most of the alloy surfaces during cooling after exposures in O_2-SO_2. This also occurred in CO_2-H_2O-O_2, but to a lesser extent. In addition, in O_2-SO_2, internal yttrium sulfides and oxy-sulfides were found in the reacted alloys. The detrimental effects of sulfur, in terms of neutralizing reactive elements and weakening the metal-oxide interface, are well known [100]. Spalled regions were left unoxidized, which indicates that delamination occurred during cooling, and did not affect the nature of the corrosion products in the isothermal experiments reported here.

Now turning to experiments conducted in O_2-SO_2 at 900 °C, reaction with Al_2O_3-CaO is again used as a baseline, where CaO conversion to $CaSO_4$ caused non-selective oxidation (Figure 51a). As shown in Figure 55a, substituting SiO_2 for Al_2O_3 in the deposit did not prevent Al_2O_3 failure. Despite the relatively high stability of calcium silicate, calcium sulfate is more stable in the O_2-SO_2 mixture used here at 900 °C (Figure 48), and was therefore not neutralized by SiO_2. The addition of Na_2SO_4 did not significantly affect the ash reactivity, as exposures to SiO_2-CaO, Al_2O_3-SiO_2-CaO-Na_2SO_4 (Figure 51b), and class C fly ash (not shown here) all produced the same non-selective oxidation morphology. Thus what is found to cause Al_2O_3 failure and govern the corrosion process is $CaSO_4$, produced by conversion of CaO in the deposit. As mentioned in Section 3.2.3.3, direct exposure to a $CaSO_4$ deposit did not quite yield the same reaction morphology, as a hot corrosion type of attack was

observed (Figure 51b). The presence of more acidic oxides (Al_2O_3, SiO_2) alongside $CaSO_4$ seems to have enhanced the sulfate reactivity toward the thermally grown Al_2O_3.

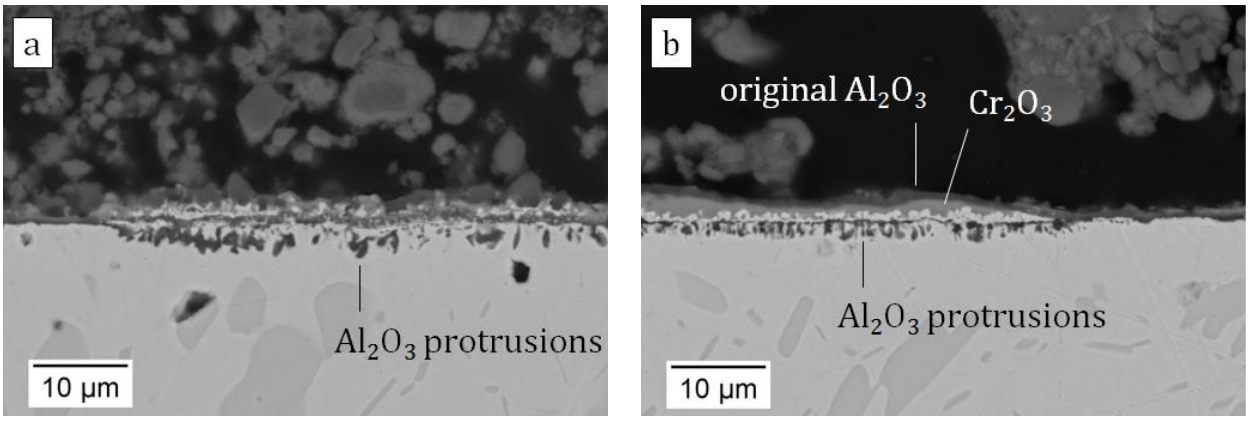

Figure 55: Reaction morphology observed after 50 h exposure of γ-rich Ni-30Co-27Cr-12Al-0.1Y to (a) SiO_2-40CaO and (b) Al_2O_3-25SiO_2-40CaO-10Na_2SO_4 in O_2-SO_2 at 900 °C. Deposit compositions in wt. %.

Type I hot corrosion experiments are typically done using Na_2SO_4 as the deposit, which is liquid at 900 °C. The γ-rich alloy used here was found not to be sensitive to this type of attack; as shown in Figure 56a, exposure to Na_2SO_4 produced small scattered protrusions of S-containing Al-Cr oxide, but overall the degradation was not significant. This was also found to be the case after exposure to a SiO_2-Na_2SO_4 mixture (not shown here). However, quite remarkably, exposure to Al_2O_3-Na_2SO_4 did trigger a hot corrosion type of attack, as internal Cr-rich sulfides developed in the alloy, and the main corrosion product was a mixed oxide-sulfate scale (Figure 56a). Solubility measurements by Rapp and coworkers [54] showed that at 927 °C, Al_2O_3 dissolved in liquid Na_2SO_4 according to a basic process, which may be written as

$$Al_2O_3 + O^{2-} = 2AlO_2^- \quad (32)$$

The solubility limit depends on the local p_{SO_3} but is rather small – of the order of 500 ppm mol Al/mol Na_2SO_4 in the gas mixture of interest. Thus mixing Na_2SO_4 in a large excess of Al_2O_3, as was done here, has the effect of increasing the melt acidity, and saturating it with aluminate ions AlO_2^-. In these conditions, the melt is not expected to dissolve a thermally grown Al_2O_3, and failure to establish an Al_2O_3 scale must involve some reaction of the melt with transient oxides. Chromium was found to be present in the corrosion product. However, since Cr_2O_3 and Al_2O_3 are both subject to basic dissolution in the conditions of interest [101], the acidification of the melt by dissolution of one would reduce the driving force for dissolution of the other – no phenomenon of synergistic dissolution, as documented by Hwang and Rapp for the Fe_2O_3-Cr_2O_3 couple [102], is expected. Understanding the reasons why the Ni-30Co-27Cr-12Al-0.1Y alloy failed to establish a protective Al_2O_3 scale in an Al_2O_3-Na_2SO_4 mixture, but succeeded when contacted to Na_2SO_4 or SiO_2-Na_2SO_4, will require further investigation of the complex interactions governing molten sulfate chemistry. This would be helpful with regards to Na_2SO_4-induced hot corrosion, but, as shown in the present work, is also relevant to $CaSO_4$-induced attack.

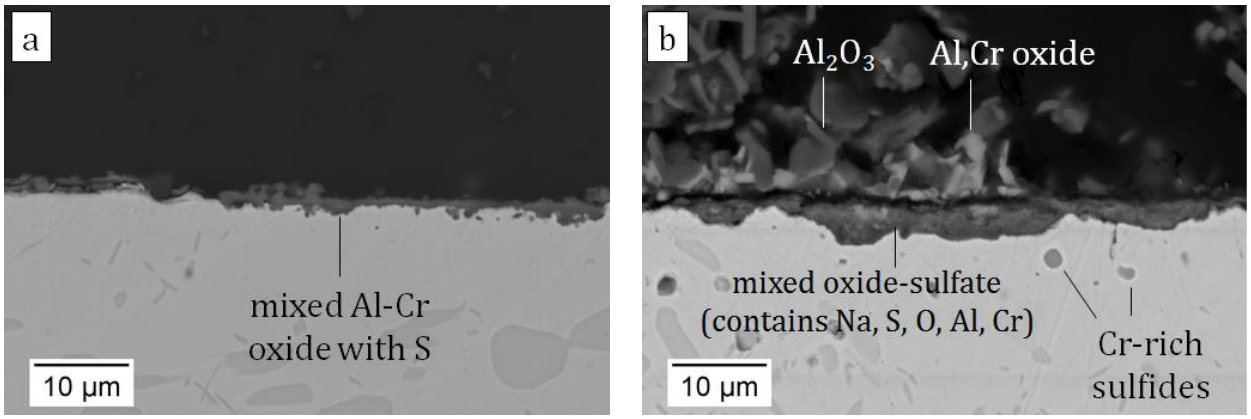

Figure 56: Reaction morphology observed after 50 h exposure of γ-rich Ni-30Co-27Cr-12Al-0.1Y to (a) Na_2SO_4 and (b) Al_2O_3-10Na_2SO_4 in O_2-SO_2 at 900 °C. Deposit composition in wt. %.

4 Conclusions and Future Work

Cyclic testing of APS TBCs with deposits in controlled gas atmospheres was shown to severely reduce TBC lifetime. Two different types of 7YSZ top coats commonly used in land-based turbines were tested. The failure of the YSZ top coat was caused by infiltration of ash constituents that resulted from liquid formation at 1100°C. Liquid K_2SO_4 was responsible for the transport of ash constituents into the porous top coat during exposure at high temperature. When a TBC cooled on thermal cycling, the infiltrated species solidified and changed the compliance of the YSZ. The exact mechanisms of the infiltration depended on deposit chemistry, but the overall effect was to reduce strain tolerance and increase elastic modulus which promoted early spallation of the top coat.

Top coat microstructure influenced deposit-induced attack on TBCs. The DVC top coats were more resistant to the infiltration compared to HPLD coatings. The relatively dense microstructure of the DVC coating was less susceptible to liquid infiltration. Also, the absence of horizontal splat boundaries did not provide easy pathways for crack propagation. The splat morphology of the HPLD top coat allowed for large regions of infiltrated YSZ to break away before complete TBC delamination, in a similar manner to erosion failure where the YSZ would spall away from the top down. Significant cracking could be observed in the HPLD top coat (far away from the TGO). The DVC top coats, in contrast, remained intact until delamination near the TGO. This type of failure in a DVC TBC was sudden and catastrophic, and it would very difficult to predict by visual inspection of a TBC.

Detrimental effects of fly-ash were observed in several atmospheres. Cyclic exposures in steam-containing atmospheres did not significantly accelerate TBC failure. This indicated that these TBCs were not susceptible to additional degradation from moisture effects on the YSZ. Atmospheres containing SO_2, however, interfered with alumina growth on the bond coat and resulted in more accelerated TBC failure. This additional effect on TBC lifetime is relevant to land-based gas turbines where TBCs are typically exposed to harsh gas atmospheres that contain SO_2. This type of degradation could enhance TBC failure even in

the absence of deposits.

This study provides important insight into deposit-induced failure that has not been well-understood in the past. Molten CMAS deposits are often studied at very high temperatures (>1200°C), and the effects of salt deposits in hot corrosion are generally well-understood at lower temperatures (700-900°C). The results presented here show a type of TBC failure that exists at intermediate temperatures (1000-1100°C) where the oxide constituents are expected to be solid. The effects of K_2SO_4 are typically not considered in similar oxide-containing (CMAS) deposits, and hot corrosion studies have reported that sulfates (without oxides) were not detrimental to TBC lifetime. When considered along with oxides, however, K_2SO_4 has been shown to play a very important role in TBC degradation. Delamination of the TBC top coat could potentially expose the underlying bond coat to the buildup of fly-ash deposits.

Based on experiments involving model as well as industrial ash mixtures, the results presented here help to identify the deposit compositions which potentially pose a threat to MCrAlY materials, and to elaborate an understanding of the associated reaction mechanisms. Of the individual oxides commonly found in fly ash, only MgO and CaO were found to have a detrimental effect on oxidation. Reaction with CaO at 1100 °C initially produced a liquid calcium chromate, which rapidly consumed the Cr-rich γ phase until an Al_2O_3 layer could be formed. The extent of degradation was greatly reduced by increasing the Al content and decreasing the Cr content of the alloy. In the steady-state regime eventually established, Al_2O_3 was simultaneously produced by oxidation of the alloy and consumed by reaction with CaO to form calcium aluminate. The kinetics of this process were analyzed in details, with particular attention to the Al flux required to sustain Al_2O_3 growth, and its evolution with temperature. This set the basis for an understanding of the conditions leading to Al_2O_3 failure from its solid-state reaction with deposits. The presence of SO_3 in the gas was found to be of importance, as it readily converted CaO into $CaSO_4$, which suppressed calcium aluminate formation but introduced yet another type of deleterious solid-state interaction with Al_2O_3 at 900 °C.

While oxide mixtures and individual sulfates were generally found not to alter Al_2O_3 scaling, the combination of oxides and sulfates induced, in certain cases, failure of the protective scale. This was interpreted in terms of modification of the sulfate chemistry by the added oxides, and of the reactivity of the resulting melt with the thermally grown oxides. High chromium contents promoted the formation of an external Cr_2O_3 layer after the initial Al_2O_3 failed, which protected the underlying alloy from the ash, and allowed the establishment of a new protective Al_2O_3 layer at the base of the corrosion product. This reaction sequence was observed in a variety of gas mixtures, with no significant effect of CO_2, H_2O or of the gas p_{O_2}. Nitrogen caused internal nitridation in air, but this did not prevent repassivation. However, in O_2-SO_2, sulfidation of chromium and aluminum hampered the establishment of a continuous Al_2O_3 layer, and the adherence of the corrosion product was greatly reduced, compared to the sulfur-free atmospheres. This would potentially be quite detrimental in thermal cycling, as was indeed observed in cyclic experiments involving complete TBCs.

Bondcoat compositions typically used in modern TBCs exhibit a fairly good resistance to the fly ash deposits tested here. Significant degradation was only observed for γ-rich alloys, when the ash combined a large amount of CaO, some SiO_2 and some Na_2SO_4. As part

of an ongoing effort to examine the chemical and microstructural aspects of alloy susceptibility to a variety of degradation modes, joint work with colleagues at the Pennsylvania State University has led to the use of computational thermodynamics to design MCrAlY alloys with independently varying phase fractions or phase compositions. Testing is in progress, but has already showed that γ-rich alloys which tended to fail in contact with class C ash also exhibited the best resistance to type I hot corrosion, while β-rich alloys exhibited an opposite trend. Combined with the experience of deposit reactivities gained from the present study, this approach of systematic alloy testing will be of considerable help to both elucidate the complex interactions between alloy and deposit chemistries, and to optimize bondcoat compositions based on the degradation modes defined by the operating conditions of interest.

5 References Cited

[1] B. Pint, "High-Temperature Corrosion in Fossil Fuel Power Generation: Present and Future," *JOM,* vol. 65, no. 8, pp. 1024-1032, 2013.

[2] N. J. Simms, P. J. Kilgallon and J. E. Oakey, "Fireside issues in advanced power generation systems".

[3] G. Hammond and S. O. W. S. Akwe, "Techno-economic appraisal of fossil-fuelled power generation systems with carbon dioxide capture and storage," *Energy,* pp. 975-984, 2011.

[4] B. M. Jenkins, L. L. Baxter, T. R. Miles and T. R. Miles, "Combustion properties of biomass," *Fuel Processing Technology,* vol. 54, pp. 17-46, 1998.

[5] C. G. Levi, J. W. Hutchinson, M.-H. Vidal-Setif and C. A. Johnson, "Environmental degradation of thermal-barrier coatings by molten deposits," *MRS Bulletin,* vol. 37, pp. 932-941, 2012.

[6] J. P. Bons, J. Crosby, J. E. Wammack, B. I. Bentley and T. H. Fletcher, "High-Pressure Turbine Deposition in Land-Based Gas Turbines From Various Synfuels," *Journal of Engineering for Gas Turbines and Power ,* vol. 129, pp. 135-143, 2007.

[7] S. Jenkins and G. Brown, *A Comparison of PC, CFB and IGCC Technologies for Basin Electric Power Cooperative's Dry Fork Station,* 2007.

[8] O. Maurstad, "An Overview of Coal based Integrated Gasification Combined Cycle (IGCC) Technology," MIT Laboratory for Energy and the Environment, Cambridge, MA, 2005.

[9] P. Wang and M. Massoudi, "Effect of Coal Properties and Operation Conditions on Flow Behavior of Coal Slag in Entrained Flow Gasifiers: A Brief Review," U.S. Department of Energy, National Energy Technology Laboratory, Pittsburgh, PA, 2011.

[10] D. Brooker, "Chemistry of Deposit Formation in a Coal Gasification Syngas Cooler," *Fuel,* vol. 72, pp. 665-670, 1992.

[11] B. M. White, R. W. Ames and P. Burke, "Conditions in Advanced Turbines for IGCC

Power Plantswith Carbon Capture," in *Proceedings of the ASME Turbo Expo 2013*, San Antonio, TX, 2013.

[12] Duke Energy, [Online]. Available: www.duke-energy.com. [Accessed 5 11 2014].

[13] W. P. Parks, E. E. Hoffman, W. Y. Lee and I. G. Wright, "Thermal Barrier Coatings Issues in Advanced Land-Based Gas Turbines," *Journal of Thermal Spray Technology,* vol. 6, no. 2, pp. 187-192, 1997.

[14] N. P. Padture, M. Gell and E. H. Jordan, "Thermal BArrier Coatings for Gas-Turbine Engine Applications," *Science,* pp. 280-284, 12 April 2002.

[15] C. Sims, N. Stoloff and W. (. Hagel, Superalloys II, New York: John Wiley and Sons, 1987.

[16] R. Darolia, "Thermal Barrier Coatings Technology: Critical Review, Progress Update, Remaining Challenges and Prospects," *International Materials Reviews,* vol. 000, no. 000, pp. 1-35, 2013.

[17] D. R. Clarke, M. Oechsner and N. Padture, "Thermal Barrier Coatings for More Efficient Gas-Turbine Engines," *MRS Bulletin,* vol. 37, no. 10, pp. 891-941, 2012.

[18] M. Peters, C. Leyens, U. Schulz and W. A. Kaysser, "EB-PVD Thermal Barrier Coatings for Aeroengines and Gas Turbines," *Advanced Engineering Materials,* vol. 3, no. 4, pp. 193-204, 2001.

[19] A. G. Evans, D. R. Mumm, J. W. Hutchinson, G. H. Meier and F. S. Pettit, "Mechanisms controlling the durability of thermal barrier coatings," *Progress in Materials Science,* vol. 46, pp. 505-553, 2001.

[20] B. Gleeson, "Thermal Barrier Coatings for Aeroengine Applications," *Journal of Propulsion and Power,* vol. 22, no. 2, pp. 375-383, 2006.

[21] W. Beele, G. Marijnissen and A. van Lieshout, "The Evolution of Thermal Barrier Coatings - Status and Upcoming Solutions for Today's Key Issues," *Surface and Coatings Technology,* Vols. 120-121, pp. 61-67, 1999.

[22] J. Chevalier, L. Gremillard, A. V. Virkar and D. R. Clarke, "The Tetragonal-Monoclinic Transformation in Zirconia: Lessons Learned and Future Trends," *J. Am. Ceram. Soc.,* vol. 92, no. 9, pp. 1901-1920, 2009.

[23] R. Reed, Superalloys: Fundamentals and Applications, Cambridge, 2006.

[24] A. Rabiei and A. G. Evans, "Failure Mechanisms Associated with the Thermally Grown Oxide in Plasma-Sprayed Thermal Barrier Coatings," *Acta mater.,* vol. 48, pp. 3963-3976, 2000.

[25] A. G. Evans, D. R. Clarke and C. G. Levi, "The influence of oxides on the performance of advanced gas turbines," *Journal of the European Ceramic Society ,* vol. 28, pp. 1405-1419, 2008.

[26] N. A. Fleck and T. Zisis, "The erosion of EB-PVD thermal barrier coatings: The competition between mechanisms," *Wear,* vol. 268, no. 11-12, pp. 1214-1224, 2010.

[27] R. Wellman, G. Whitman and J. R. Nicholls, "CMAS corrosion of EB PVD TBCs: Identifying the minimum level to initiate damage," *Int. Journal of Refractory Metals & Hard Materials,* vol. 28, pp. 124-132, 2010.

[28] R. Wellman and J. Nicholls, "Erosion, corrosion and erosion-corrosion of EB-PVD thermal coatings," *Tribology International,* vol. 41, no. 7, pp. 657-662, 2008.

[29] L. Li, N. Hitchman and J. Knapp, "Failure of Thermal Barrier Coatings Subject to CMAS Attack," *Journal of Thermal Spray Technolog,* vol. 19, no. 1-2, pp. 148-155, 2010.

[30] S. Kramer, J. Yang and C. G. Levi, "Infiltration-Inhibiting Reaction of Gadolinium Zirconate Thermal Barrier Coatings with CMAS Melts," *J. Am. Ceram. Soc.,* vol. 91, no. 2, pp. 576-583, 2008.

[31] C. Mercer, S. Faulhaber, A. G. Evans and R. Darolia, "A delamination mechanism for thermal barrier coatings subject to calcium-magnesium-alumino-silicate (CMAS) infiltration," *Acta Materialia,* vol. 53, pp. 1029-1039, 2005.

[32] P. Mohan, T. Patterson, B. Yao and Y. Sohn, "Degradation of Thermal Barrier Coatings by Fuel Impurities and CMAS: Thermochemical Interactions and Mitigation Approaches," *Journal of Thermal Spray Technology,* vol. 19, no. 1-2, pp. 156-167, 2010.

[33] J. Wu, H.-b. Guo, Y.-z. Gao and S.-k. Gong, "Microstructure and thermo-physical properties of yttria stabilized zirconia coatings with CMAS deposits," *Journal of the European Ceramic Society,* vol. 31, pp. 1881-1888, 2011.

[34] S. Kramer, J. Yang, C. Levi and C. A. Johnson, "Thermochemical Interaction of Thermal Barrier Coatings with Molten CaO-MgO-Al2O3-SiO2 (CMAS) Deposits," *J. Am. Ceram. Soc.,* vol. 89, pp. 3167-3175, 2006.

[35] M. Yoshiba, K. Abe, T. Aranami and Y. Harada, "High-Temperature Oxidation and Hot Corrosion Behavior of Two Kinds of Thermal Barrier Coating Systems for Advanced Gas Turbines," *Journal of Thermal Spray Technology,* vol. 5, no. 3, pp. 259-268, 1996.

[36] R. L. Jones, "Some Aspects of the Hot Corrosion of Thermal Barrier Coatings," *Journal of Thermal Spray Technology,* vol. 6, no. 1, pp. 77-84, 1997.

[37] C. Batista, A. Portinha, R. M. Ribeiro, V. Teixeira and C. R. Oliveira, "Evaluation of laser-glazed plasma-sprayed thermal barrier coatings under high temperature exposure to molten salts," *Surface & Coatings Technology,* vol. 200, pp. 6783-6791, 2006.

[38] V. Deneux, Y. Cadoret, S. Hervier and D. Monceau, "Effect of Water Vapor on the Spallation of Thermal Barrier Coating Systems During Laboratory Cyclic Oxidation Testing," *Oxid. Met.,* vol. 73, pp. 83-93, 2010.

[39] J. L. Smialek, D. Zhu and M. D. Cuy, "Moisture-induced delamination video of an oxidized thermal barrier coating," *Scripta Materialia,* vol. 59, pp. 67-70, 2008.

[40] J. Smialek, "Moisture-Induced Delayed Spallation and Interfacial Hydrogen Embrittlement of Alumina Scales," *JOM,* pp. 29-35, 2006.

[41] X. Guo, "On the degradation of zirconia ceramics during low-temperature annealing in water vapor," *Journal of Physics and Chemistry of Solids,* vol. 60, pp. 539-546, 1999.

[42] X. Guo, "Low temperature degradation mechanism of tetragonal zirconia ceramics in water: role of oxygen vacancies," *Solid State Ionics,* vol. 112, pp. 113-116, 1998.

[43] T. Gheno, D. Monceau, D. Zhang and D. Young, *Corrosion Science,* vol. 53, pp. 2767-2777, 2011.

[44] D. Young, High Temperature Oxidation and Corrosion of Metals, Amsterdam: Elsevier,

2008.

[45] M. Michalik, M. Hansel, J. Zurek, L. Singheiser and W. Quadakkers, *Materials at High Temperatures,* vol. 22, pp. 213-221, 2005.

[46] J. Ehlers, D. Young, E. Smaardijk, A. Tyagi, H. Penkalla and L. Q. W. Singheiser, *Corrosion Science,* vol. 48, pp. 3428-3454, 2006.

[47] G. Meier, K. Jung, N. Mu, N. Yanar, F. Pettit, J. Piron Abellan, T. Olszewski, L. Nieto Hierro, W. Quadakkers and G. Holcomb, *Oxidation of Metals,* vol. 74, pp. 319-340, 2010.

[48] E. Opila and D. Myers, *Journal of the American Ceramic Society,* vol. 87, pp. 1701-1705, 2004.

[49] M. Maris-Sida, G. Meier and F. Pettit, *Metallurgical and Materials Transactions A,* vol. 34A, pp. 2609-2619, 2003.

[50] R. Kartono and D. Young, *Materials and Corrosion,* vol. 59, pp. 455-462, 2008.

[51] M. DeCrescente and Bornstein, *Corrosion,* vol. 24, pp. 127-133, 1968.

[52] J. Goebel and F. Pettit, *Met Trans ,* vol. 1, pp. 1943-1954, 1970.

[53] J. Stringer, *Annu Rev Mater Sci,* vol. 7, pp. 477-509, 1977.

[54] R. Rapp, *Corrosion,* vol. 42, pp. 568-577, 1986.

[55] G. Goward, *Journal of Engineering for Gas Turbines and Power,* vol. 2, pp. 421-425, 1986.

[56] N. Birks, G. Meier and F. Pettit, "Chapter 8," in *Hot Corrosion, an Introduction to the High Temperature Oxidation of Metals, 2nd Edition*, Cambridge, Cambridge University Press, 2006, pp. 205-252.

[57] F. Pettit, *Oxid Met,* vol. 76, pp. 1-21, 2011.

[58] M. Helminiak, N. Yanar, F. Pettit, T. Taylor and G. Meier, "The Behavior of High-Purity, Low-Density Air Plasma Sprayed Thermal Barrier Coatings," *Surface and Coatings Technology,* pp. 793-796, 2009.

[59] R. Vaben, N. Czech, W. Mallener, W. Stamm and D. Stover, "Influence of Impurity Content and Porosity of Plasma-Sprayed Yttria-Stabilized Zirconia Layers on the Sintering Behaviour," *Surface and Coatings Technology,* vol. 141, no. 2-3, pp. 135-140, 2001.

[60] *Materials Preparation Canter, Ames Laboratory USDOE, Ames IA, USA.*

[61] B. Sundman, B. Jansson and J. Andersson, *Calphad,* vol. 9, pp. 153-190, 1985.

[62] P. e. a. Turchi, "Kattner, U.R.," in *CALPHAD and Alloy Thermodynamics, P.E.A.*, Warrendale, PA, 2002.

[63] J. Hamilton and A. Nagelberg, "In Situ Raman Spectroscopic Study of Yttria-Stabilized Zirconia Attack by Molten Sodium Vanadate," *Journal of the American Ceramic Society,* vol. 67, no. 10, pp. 686-690, 1984.

[64] V. Tolpygo and D. Clarke, *Mater High Temp,* vol. 17, pp. 59-70, 2000.

[65] Y. Pliego-Cuervo and F. Glasser, "The Role of Sulphates in Cement Clinkering Reactions: Phase Formation in the System CaO-Al2O3-Fe2O3-SiO2-CaSO4-K2SO4,"

Cement and Conctrete Research, vol. 9, pp. 573-581, 1979.

[66] C. Giggins and F. Pettit, *Journal of the Electrochemical Society,* vol. 118, pp. 1782-1790, 1971.

[67] N. Belen, P. Tomaszewicz and D. Young, *Oxidation of Metals,* vol. 22, pp. 227-245, 1984.

[68] J. Chen, P. Rogers and J. Little, *Oxidation of Metals,* vol. 47, pp. 381-410, 1997.

[69] U. Brill and D. Agarwal, in *NACE Corrosion 97 Conference*, New Orleans, LA (USA), 1997.

[70] G. Ackermann, G. Teneva-Kosseva, H. Kohne, K. Lucka, S. Richter and J. Mayer, *Materials and Corrosion,* vol. 59, pp. 380-388, 2008.

[71] A. Sato, Y. Chiu and R. Reed, *Acta Materialia,* vol. 59, pp. 225-240, 2011.

[72] M. Task, B. Gleeson, F. Pettit and G. Meier, *Oxidation of Metals,* vol. 80, pp. 125-146, 2013.

[73] E. Levin, C. Robbins and H. McMurdie, Phase Diagrams for Ceramists. Vol. 1, Columbus, OH: The American Ceramic Society, 1964.

[74] A. Kaiser, B. Sommer and E. Woermann, *Journal of the American Ceramic Society,* vol. 75, pp. 1463-1471, 1992.

[75] K. Chiang, G. Meier and R. Perkins, *Journal of Materials for Energy Systems,* pp. 71-86, 1984.

[76] H. Hindam and D. Whittle, *Oxidation of Metals,* vol. 18, pp. 245-284, 1982.

[77] G. Rybicki and J. Smialek, *Oxidation of Metals,* vol. 31, pp. 275-304, 1989.

[78] M. Brumm and H. Grabke, *Corrosion Science,* vol. 33, p. 1677, 1992.

[79] M. Gulgun, O. Popoola and W. Kriven, *Journal of the American Ceramic Society,* vol. 77, 1994.

[80] B. Mohamed and J. Sharp, *Journal of Materials Chemistry,* vol. 7, pp. 1595-1599, 1997.

[81] C. Ghoroi and A. Suresh, *AIChe,* vol. 53, pp. 502-513, 2007.

[82] C. Wagner, *Acta Metallurgica,* vol. 17, pp. 99-107, 1969.

[83] G. Yurek, J. Hirth and R. Rapp, *Oxidation of Metals,* vol. 8, pp. 265-281, 1974.

[84] F. Gesmundo and F. Viani, *Corrosion Science,* vol. 18, pp. 217-230, 1978.

[85] F. Viani and F. Gesmundo, *Corrosion Science,* vol. 20, pp. 541-554, 1980.

[86] H. Hsu, *Oxidation of Metals,* vol. 26, pp. 315-332, 1986.

[87] G. Wang, B. Gleeson and D. Douglass, *Oxidation of Metals,* vol. 31, pp. 415-429, 1989.

[88] A. Heuer, D. Hovis, J. Smialek and B. Gleeson, *Journal of the American Ceramic Society,* vol. 94, pp. S146-S153, 2011.

[89] J. Jedlinski and G. Borchardt, *Oxidation of Metals,* vol. 36, pp. 317-337, 1991.

[90] J. Doychak, J. Smialek and T. Mitchell, *Metallurgical Transactions A,* vol. 20A, pp. 499-518, 1989.

[91] B. Pint, J. Martin and L. Hobbs, *Solid State Ionics,* vol. 78, pp. 99-107, 1995.

[92] *HSC version 6.0,* Pori, Finland: Outokumpu Research Oy.

[93] C. Wagner, *Journal of the Electrochemical Society,* vol. 99, pp. 369-380, 1952.

[94] W. Weisweiler and S. Ahmed, *Zement-Kalk-Gips,* vol. 33, pp. 84-89, 1980.
[95] J. Nesbitt and R. Heckel, *Metallurgical Transactions A,* vol. 18, pp. 2075-2086, 1987.
[96] C. Campbell, W. Boettinger and U. Kattner, *Acta Materialia,* vol. 50, pp. 775-792, 2002.
[97] F. Gesmundo and B. Gleeson, *Oxidation of Metals,* vol. 44, pp. 211-237, 1995.
[98] P. Carter, B. Gleeson and D. Young, *Acta Materialia,* vol. 44, pp. 4033-4038, 1996.
[99] T. Nijdam and W. Sloof, *Acta Materialia,* vol. 56, pp. 1972-4983, 2008.
[100] T. Gheno, D. Monceau, D. Oquab and Y. Cadoret, *Oxidation of Metals,* vol. 73, pp. 95-113, 2010.
[101] R. Rapp, *Corrosion,* vol. 42, pp. 568-577, 1986.
[102] Y. Hwang and R. Rapp, *J Electrochem Soc,* vol. 137, pp. 1276-1280, 1990.
[103] R. A. Miller, "Ceramic Thermal Barrier Coatings for Electric Utility Gas Turbine Engines," in *3rd Berkely Conference on Corrosion, Erosion, and Wear of Materials*, Berkely, CA, 1986.
[104] P. Mohan, T. Patterson, Y. Sohn and V. H. Desai, "Degradation of Thermal Barrier Coatings by Molten CMAS (CaO-MgO-Al2O3-SiO2) Deposits," in *47th AIAA Aerospace Sciences Meeting Including The New Horizons Forums and Aerospace Exposition*, Orlando, Florida, 2009.
[105] Wofram Research, Inc., *Mathematica, Version 9.0,* Champaign, IL, 2012.
[106] F. Maak, *Zeitschrift fur Metallkunde,* vol. 52, p. 538, 1961.
[107] X. Liu, T. Gheno, B. Gleeson and Z. Liu, To be published, 2015.